Summer 8-22-2018

Thermochemical Conversion of Guaiacol Over Unsupported Tungsten Oxide and Nickel Supported Catalysts

Pamela Ruiz Martinez
University of Maine, pameruizm@gmail.com

Recommended Citation

Martinez, Pamela Ruiz, "Thermochemical Conversion of Guaiacol Over Unsupported Tungsten Oxide and Nickel Supported Catalysts" (2018). *Electronic Theses and Dissertations*. 3021.
https://digitalcommons.library.umaine.edu/etd/3021

THERMOCHEMICAL CONVERSION OF GUAIACOL OVER UNSUPPORTED TUNGSTEN OXIDE AND NICKEL SUPPORTED CATALYSTS

By

Pamela Ruiz Martinez

B.A. University of Concepcion, 2009

A THESIS
Submitted in Partial Fulfillment of the
Requirements for the Degree of
Doctor of Philosophy
(in Chemistry)

The Graduate School
The University of Maine
August 2018

Advisory Committee:

- Brian Frederick, Associate Professor of Chemistry, Advisor
- William J DeSisto, Professor of Chemical Engineering, Co-Advisor
- Rachel Austin, Professor of Chemistry, Barnard College
- Barbara Cole, Professor of Chemistry
- Carl Tripp, Professor of Chemistry

THERMOCHEMICAL CONVERSION OF GUAIACOL OVER UNSUPPORTED TUNGSTEN OXIDE AND NICKEL SUPPORTED CATALYSTS

By Pamela Ruiz Martinez

Thesis Co-Advisors: Dr. Brian Frederick and Dr William J. DeSisto

An Abstract of the Thesis Presented
in Partial Fulfillment of the Requirements for the
Degree of Doctor of Philosophy
(in Chemistry)

August 2018

Interest in conversion of biomass into renewable fuels has motivated development of thermochemical methods for production of bio-oil and development of hydrodeoxygenation catalysts for upgrading the oil. Two types of catalysts were investigated. The catalytic activity of unsupported tungsten oxide bronze catalysts for the conversion of guaiacol was explored as a representative compound from bio-oil. The reactions were carried out in a trickle bed reactor at various concentrations of the reactant and hydrogen pressure, as well as varying catalyst activation and reaction temperatures. The reaction pathway from guaiacol to phenol by demethoxylation, followed by hydrogenation to cyclohexanol, and finally dehydration to cyclohexene was determined experimentally. Kinetic data revealed approximately first order dependence on hydrogen pressure and zeroth order dependence on guaiacol concentration. Langmuir-Hinshelwood-Hougan-Watson models were tested within a plug flow reactor model. The best fit

was for a reaction mechanism in which the guaiacol methoxy C-O bond scission was the rate controlling step with guaiacol and some phenol blocking active sites. Catalytic activity and selectivity of supported Ni-based catalysts were also studied for the same model compound (guaiacol) in order to evaluate the role of metal hydrogenation sites and acid dehydration sites. The supports used were SiO_2, Al_2O_3 and SiO_2-Al_2O_3. All catalysts were prepared by the incipient wetness impregnation method and were characterized by different physico-chemical techniques. Conversion reactions were carried out in a batch reactor at 5 MPa of H_2 pressure and 300 °C. The maximum catalytic activity among the Ni/Al_2O_3 catalysts was attributed to the formation of a greater number of active metal sites arising from an optimal nickel dispersion at a loading of 8 wt%. At higher Ni content, the formation of Ni aggregates was observed resulting in loss of active sites. The selectivity (at constant conversion and metal loading) toward deoxygenated products, cyclohexene and cyclohexane, was clearly related to the acid sites of the support, which were much greater on SiO_2-Al_2O_3.

ACKNOWLEDGEMENTS

Many people played a role to produce this thesis and I would like to express my sincere gratitude to all of them. First, I would like to thank my co-advisors Dr. Brian Frederick and Dr. William DeSisto, for their guidance with my work. To Dr. Frederick for working with me nights and weekends to help me complete the work described in the following pages. I am truly grateful for all their help and patience.

I'd like to thank Dr Tom Schwartz for his help with our Mathcad models setup and development, all his help was necessary to complement our experimental work.

I'd like to thank Dr. M. Clayton Wheeler for opening the doors of his lab and allow me to work and complete my experimental work.

I'd like to thank Dr. Nestor Escalona from Univerdad Catolica, Chile. For his input and the realization of experimental characterizations necessary to complete this thesis. I'd also like to thank Nick Hill who also was around to solve any reactor leaks issues. The experimental work would have not been possible without his help.

I'd like to thank the Department of Energy for funding my research and the support from the Forest Bioproducts Research Institute (FBRI), the Department of Chemistry, and the Graduate School for funding me during the summer to complete my thesis.

I'd also like to thank my husband, Jose Carrasco, for all his patience, unconditional support and for always being there for me through all kinds of situations. To my parents for all their love and support, who always made me work hard and reach my goals.

Last but not least, I would like to thank Barbara Frederick and family for opening the doors of her home and allow me to recover from surgery after my cancer diagnosis, for all her kindness and encouragement, please know that you will always remain in our hearts.

TABLE OF CONTENTS

Chapters

LIST OF TABLES

LIST OF FIGURES

CHAPTER 1.

INTRODUCTION AND BACKGROUND

1.1. Lignocellulosic Biomass

From the late seventeenth century, fossil fuels have been the basis of industrialization for both developed and emerging countries. In 2013, coal, petroleum and natural gas have been the source of more than 80% of the United States energy used with annual consumption projected to remain near those levels through 2040 [1] According to the petroleum statistics [2], the transportation sector relies heavily on fossil fuels. This overdependence on oil as an energy source has raised serious economic and environmental concerns.

The demand for oil far outweighs the limited reserves available. The oil market, since the last report from World Oil Outlook dated November 2014 [3], has encountered major changes. For example, the first half of 2014 registered oil prices of over $100/barrel; this figure dropped to less than $60/barrel by December 2014. The oil prices during the first nine months of the following year averaged $53/barrel. The Organization of Petroleum Exporting Countries (OPEC) reported that in 2014 the global consumption totaled 91.3 million barrels per day (mb/d) [4], predicting now that this demand will reach 97 mb/d by 2020. This increment represents a 0.94% yearly increase.

The environmental impact of CO_2 emissions from crude oil-derived fuels will follow the predicted oil demand trend and contribute to global warming, which is a subsequent effect of greenhouse gas emissions. These economic and environmental concerns have generated increased interest for developing non-fossil energy sources and chemicals [5] in order to reduce the dependence on fossil fuels [6-8].

Among the energy sources available, biomass is the only carbon-rich source that is considered a promising renewable energy resource that could reduce the actual dependence on fuel and petrochemical feedstock [6, 9]. Biomass offers a wide variety of solid, liquid and gaseous products that can be obtained through three thermochemical conversion processes: gasification, direct combustion, and pyrolysis [10, 11] as shown in Figure 1.1. Life cycle analysis suggests that its impact on the environment is minimal because it is near CO_2 neutral [12, 13]. Biomass is also a potential source of value-added chemicals.

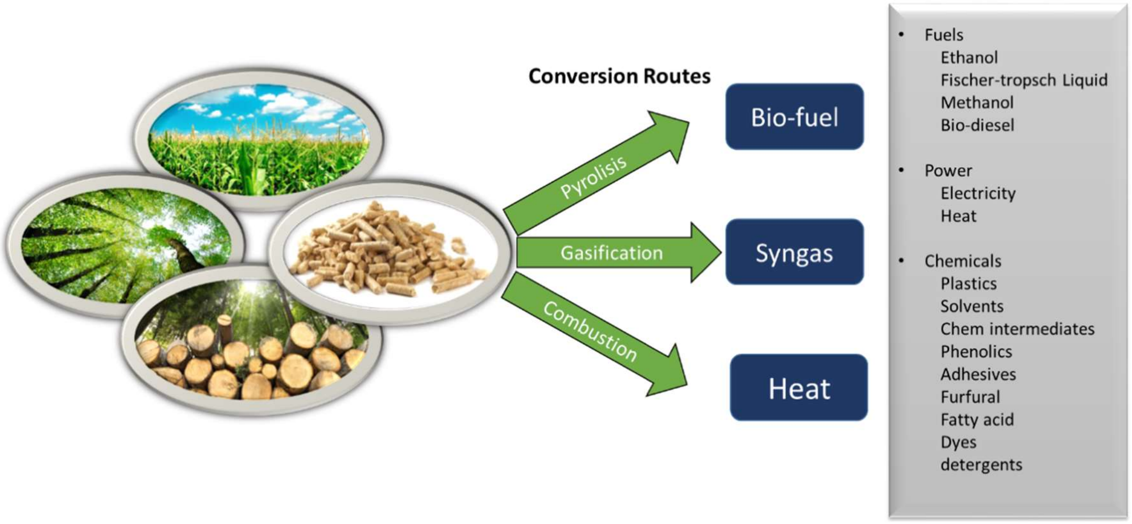

Figure1.1 Thermochemical conversion technologies of biomass. Adapted from source: http://www.cleantechloops.com/biomass-conversion-technologies/

A wide variety of feedstocks can be used to generate biofuels. Sugars and vegetable oils are the raw material for the so-called "first generation" biofuels. Lignocellulosic biomass, such as residues from agriculture and forestry operations, is converted into "second-generation" biofuels. Bioethanol and biodiesel are first-generation biofuels with a global increase in demand due to governmental mandates to blend them with crude oil-derived fuels. However, since the production of ethanol comes mainly from corn, there is controversy on using edible plants for fuel generation because it contributes to global food shortage and increase in price. This has led to accelerated interest in non-edible plant materials and waste residues, known as lignocellulosic biomass, as feedstock.

A wide variety of biomass waste, including sugar cane bagasse, rice husk, switch grass, wheat straw and wood, is readily available for transformation into bio-oil. The transformation of solid lignocellulosic biomass into a liquid product is achieved through fast pyrolysis. Pyrolysis occurs in the absence of oxygen, in a temperature range between 400 °C to 650 °C, high heating rates, and short residence time (1-2 seconds). A dark brown liquid is obtained, called "bio-oil". In the fast pyrolysis process, biomass is transformed to bio oils that have the potential to be converted into transportation fuels and commodity chemicals, although their high oxygen content 15-40% weight, high viscosity and instability doesn't make it possible to use them directly and it needs to be upgraded[14-17]. Pyrolysis yields approximately 40% liquid product by mass [9, 11]. The main advantage of the pyrolysis process is that nearly any type of biomass can be transformed into bio-oil. The product properties depend on the conditions of the process and the type of feedstock [4, 18, 19]. Bio-oil properties have been extensively studied and reported in the literature [8, 11, 20-27]. For example, DeSisto et al. [27] studied the fast pyrolysis of pine sawdust to optimize the liquid yield by varying reaction temperature and residence time. The authors reported a strong dependence on temperature: the highest liquid yield was obtained at 500 °C and it reached 65%. The authors also analyzed the bio-oil composition by GC/MS. Guaiacol, phenol, catechol and their derivatives, as well as sugars, stilbenes and resin acids were among the compounds found. Similar results were reported by Ingram et al.[28] for the pyrolysis of pine wood at 450 °C. Another major source of biomass is rice husk, [29] a by-product of rice, that is non-edible and widely available. Alvarez et al.[29] studied the effect of temperature on product yield and product composition in a conical spouted bed reactor; the result was a maximum liquid yield of 70% at 450 °C. They also reported a wide variety of chemical compounds in the bio-oil such as acids, aldehydes, ketones, phenols, guaiacols, catechols, ethers, furans and saccharides. The pyrolysis process increases the energy density (energy per volume) of green biomass by a factor of 6-7 depending on moisture content [30], making the product more promising as a prospective biofuel [4].

Bio-oil contains a complex mixture of over 400 different oxygenated molecules, comprising water (10-30% wt) and oxygenated compounds such as: aldehydes, ketones, sugars, carboxylic acids, esters, furans, guaiacols and phenolics [11, 20, 22]. The high-water content and the oxygenated compounds present make bio-oil polar in nature, and therefore bio-oil is immiscible with crude oil.

The major difference between crude oil and bio-oil is the elemental composition. Bio-oil contains 10 to 40% oxygen while crude oil contains almost 0% oxygen. This high oxygen content in bio-oil derives from the biomass composition comprised of the three main biopolymers named cellulose, hemicellulose, and lignin, as shown in Figure 1.2.

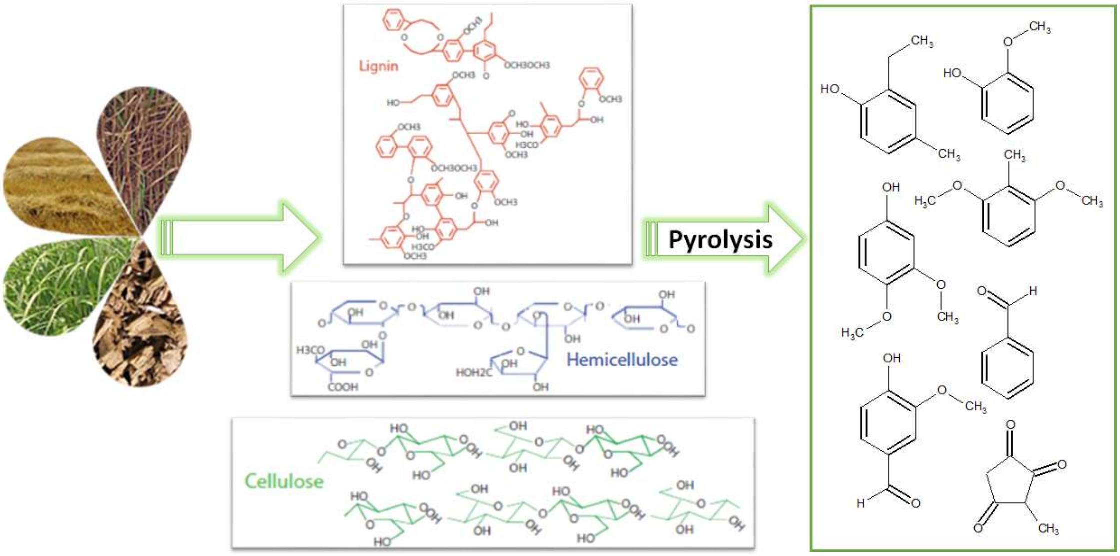

Figure 1.2 Lignocellulosic Biomass Source. Adapted from Biocore Project and Alonso et al.[31]

High water and oxygen content causes practical issues: poor volatility, low heating values (19 MJ/kg) compared to conventional fuel (40 MJ/kg), low stability during storage, high acidity, and corrosiveness [23, 32]. Therefore, bio-oil cannot be used directly as a high-quality fuel in a conventional engine. Thus, bio-oil needs to be upgraded by totally or partially removing oxygen in order to make it suitable as a transportation fuel. Upgrading methods that have had some success as reported in the literature include cracking and zeolite upgrading. The most feasible route to upgrade bio oils is by hydrodeoxygenation (HDO), hydrotreatment that can remove partially or totally the oxygen content and improve the chemical and fuel properties of the oils [33-39].

1.2. Catalytic hydrodeoxygenation

Hydrodeoxygenation is analogous to the hydrotreating processes (hydrodesulfurization and hydrodenitrogenation) used in the petroleum refinery to remove sulfur and nitrogen heteroatoms. Typical hydrodeoxygenation catalysts are sulfided NiMo and CoMo supported on alumina studied previously by Delmon et al. [40, 41]. HDO studies are performed over heterogeneous catalysts with hydrogen as the gas and reactant at pressures between 7-30 MPa and temperatures between 300-600 °C [5, 40-45] in order to reduce the high content of oxygen-containing molecules. Hydrogen is consumed throughout the process and oxygen is removed by the formation of water [23]. The main drawback of using sulfided catalysts as active phases for HDO is that bio oils do not contain sulfur. In order to maintain catalyst activity, it is necessary to add sulfur to the feed, which can cause contamination of the catalyst and products, as reported by Bui et al [46, 47].

Mild hydrotreating conditions on pyrolysis oil still have a tendency for coke formation. Species such as alkoxyphenols and guaiacol are highly reactive and can polymerize during the upgrading process [48]. Therefore, a low temperature stabilization step followed by a higher temperature treatment is recommended for pyrolysis oil upgrading [49]. High pressures aid the solubility of H_2 in the oil and thereby a high availability of hydrogen surrounds the catalyst surface, keeping it active, alleviating coke formation, and increasing the reaction rate [50]. Extensive work has been done to improve qualities of bio-oil. Wildschut et al.[51] studied Ru/Al_2O_3, Pt/C, Ru/C, Ru/TiO_2, and Pd/C catalysts for the two-step upgrading process of bio-oil: the first step at mild conditions (250 °C and 100 bar) prevented the polymerization process that bio-oil undergoes, and a second step, at more severe reaction conditions (350 °C and 200 bar) led to significant upgrading of bio-oil. Many reactions take place during HDO of bio-oil, including: cracking, decarbonylation, decarboxylation, deoxygenation, hydrogenation and polymerization [52]. Routray et al. [53] reported the catalytic upgrading of bio-oil using Ru/C at a low temperature of 130 °C, where hydrogenation typically occurs, and 2000 psi H_2 pressure. The authors reported that after 64 h on stream, the reactor built up a pressure above 2200 psi, indicating plugging of the reactor due to coke accumulation on the surface of the catalyst. The functional groups that were hydrogenated were carboxylic acids, ketones, phenols (guaiacols, syringols, catechols), furfurals (furfural, 5-hydroxy methyl furfural), and lignin-based components; however, sugars were not reactive under these conditions. These studies demonstrate the effectiveness of different catalysts for HDO of bio-oil. Hydrotreatment of bio-oil presents complex challenges due to the large number of different functional groups present with different reactivities; as a consequence, the studies are often empirical and do not offer insights into reaction pathways and other parameters needed to improve the process. Thus, most of the HDO studies reported in the literature have used model compounds representative of the different compounds present in cellulose, hemicellulose and lignin. Initial studies in the early 1980s were devoted to catalytic, kinetic, and mechanistic studies [33, 54]. However, the studies were part of hydrotreating studies for crude oil and were limited in scope because of the low oxygen content of crude oil. Over the last decade, there has been substantial increase in HDO research driven by the aforementioned desire to explore alternatives to petroleum crude. Although significant achievements have been made, the development of effective HDO catalysts is still challenging and requires sustained efforts[8].

1.3. Guaiacol as model compound of bio-oil

More than 400 oxygenated organic compounds have been identified in bio-oils, in which the composition and oxygen content determine the reactivity of the compound during HDO. Studying different model compounds present in bio-oils is crucial to understand the mechanism of the upgrading process. Moreover, for each model compound the reaction mechanism will differ for a given catalyst or active phase present. Fundamental studies utilize model compounds rather than bio-oils because this approach allows a better understanding of the reaction process and the mechanism involved [55-57].

Fast pyrolysis bio-oil is a biphasic mixture (aqueous and organic phase). It contains depolymerized cellulose, hemicellulose and lignin components, as shown in Figure 1.4. 2-methoxy phenol (guaiacol), found in the organic phase, is an attractive model compound because it contains both phenolic and methoxy functional groups, which makes guaiacol challenging for complete deoxygenation. Several catalytic systems have been applied to guaiacol HDO, including conventional hydrotreating catalysts, NiMo and CoMo supported on Al_2O_3, metal phosphides, and noble metals, among others [8, 44, 56, 58-69]. The conversion of guaiacol involves several consecutive transformations, including aromatic ring hydrogenation, C-O and C-C bond cleavage, and alkylation[46, 70-73]. The preference for particular routes depend on the nature of catalyst and the reaction conditions. A generalized reaction pathway adapted from Bykova et al. is shown in Fig 1.4[72]

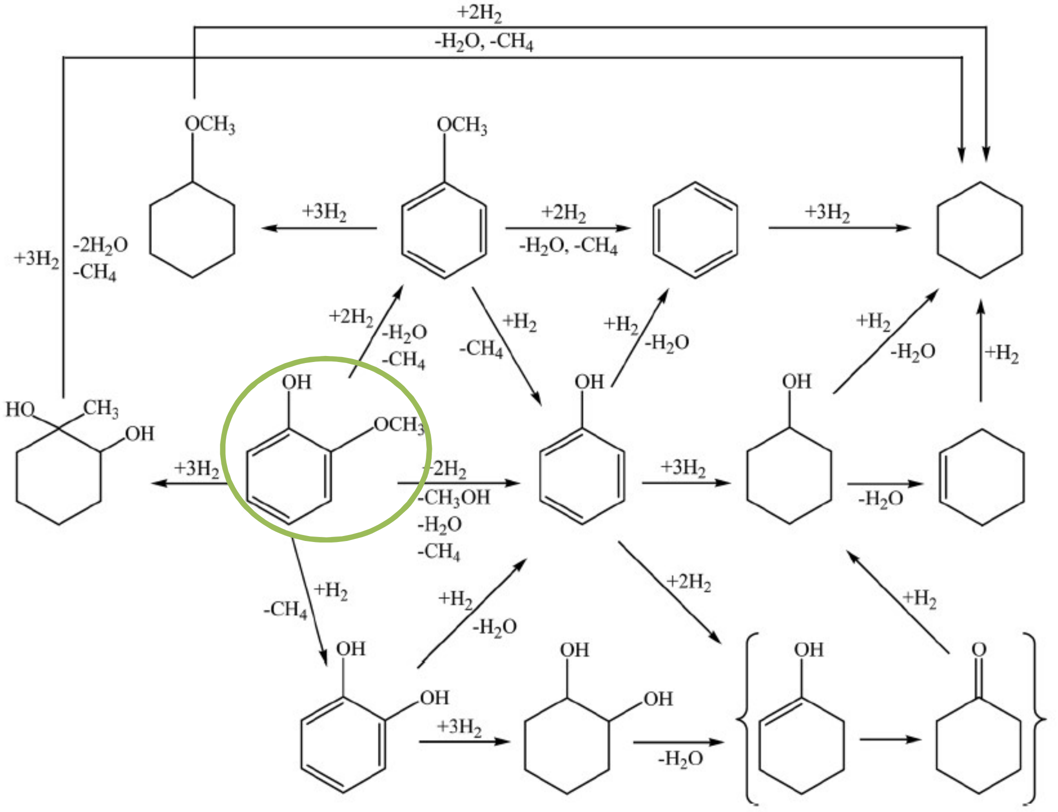

Figure 1.3 Proposed reaction pathways during the conversion of guaiacol. Reproduced from Bykova et al. [72].

Guaiacol can be transformed by demethylation (DME) to catechol, which then undergoes hydrogenolysis to form phenol. Guaiacol can also be directly converted to phenol by a demethoxylation reaction (DMO, hydrogenolysis of the Ar-OCH_3 bond). The phenol ring can then undergo hydrogenation to cyclohexanol, and subsequent dehydration to cyclohexene followed by hydrogenation to cyclohexane. This network has been proposed by several other studies in the literature [8, 46, 67].

1.4. Sulfided catalysts

Typical catalysts used for HDO are those used for hydrodesulfurization (HDS) and hydrodenitrogenation (HDN) processes, such as sulfided CoMo and NiMo supported on alumina. Delmon et al. [40, 41]. used guaiacol as a representative molecule of the bio oil to be able to understand the chemical transformation mechanism involved during the reaction. Guaiacol contains two oxygen type functionalities (-OCH_3 and –OH). The transformation of this compound produced as a main product catechol by demethylation (DME), which is later transformed by a combination of C-O bond breaking and hydrogenation (HYD), benzene and cyclohexane were observed as final products. Other sulfided catalyst studies have shown similar results [46, 47, 74-76] For these catalysts, cobalt and nickel are used as promoters to donate electrons to molybdenum atoms and weaken the bond between sulfur and molybdenum, generating sulfur vacancies that are the active sites for HDO and HDS reactions [77]. Metal sulfides have shown high reactivity for HDO processes. These catalysts require an activation temperature above 500 °C in the presence of a mixture of H_2S and H_2; in addition, a sulfiding agent is needed in the feed to keep the catalyst active throughout the process. Various supports have been studied including silica, alumina, silica-alumina or zeolites [33, 78, 79].

Non-traditional sulfide catalysts have also been reported in the literature for HDO. In particular, rhenium sulfide has shown great potential for the HDO of guaiacol.

Ruiz et al. [75] studied the effect of sulfiding mixture (H_2S/H_2, H_2S/N_2) on rhenium catalysts supported on ZrO_2 and ZrO_2-sulfated for the HDO of guaiacol using a batch reactor at 5 MPa and 300 °C (CS_2 was added to the liquid mixture as a sulfiding agent). The results showed that H_2S/N_2 was a more effective sulfiding mixture and led to ReS_2/ZrO_2 being 2.8 times more active than a commercial $NiMoS/Al_2O_3$ catalyst.

Similarly, Sepulveda et al [70, 76, 80] used sulfided rhenium catalysts supported on SiO_2 and Al_2O_3 for HDO of guaiacol and found that the type of support used dictates the reaction pathway: ReS_2/SiO_2 favored direct demethoxylation of guaiacol to phenol while ReS_2/Al_2O_3 preferred demethylation of guaiacol to catechol, which is subsequently deoxygenated to phenol, as shown in Figure 1.3.

Overall, sulfided catalysts have demonstrable deoxygenation activity but their application is limited by the need to add sulfiding agent to the feed to replace the one stripped from the catalyst during the reaction, which contaminates the product and catalyst [40, 81-83]. Therefore, there has been a shift in the literature towards non-sulfide catalysts including noble metals, transition metal phosphides, carbides, nitrides, non-noble metal catalysts, and bifunctional metal/acid catalysts.

1.5. Noble metal catalysts

Noble metal catalysts such as Ru, Pt, Pd, and others have been shown to be highly active for the HDO of guaiacol [67, 84-86]. Typical compounds found are 2-methoxycyclohexanol, 2-methoxycyclohexanone, 1-methoxycyclohexane, cyclohexanol, and cyclohexanone, which leads to a high hydrogen consumption and the costs of these metals makes them less attractive in industry applications [84, 87]. In one of the first studies, Gutierrez et al [84] found that ZrO_2-supported monometallic and bimetallic noble metal catalysts containing Pt, Pd, and Rh, exhibited higher activity than conventional sulfided $CoMo/Al_2O_3$ catalysts, favoring hydrogenation-deoxygenation over a direct deoxygenation pathway. On the other hand, Nimmanwudipong et al. [67, 88] studied HDO reactions on $Pt/\gamma\text{-}Al_2O_3$ using different model compounds such as guaiacol, anisole, cyclohexanone and 4-methylanisole. The authors found that, in general, Pt metallic sites were responsible for hydrogenation while the acidic Al_2O_3 support promoted transalkylation reactions.

In Rh based catalysts[71, 87], the first step of conversion of guaiacol is the hydrogenation of the ring, followed by demethoxylation or dehydroxylation. Noble metals (Pt, Rh, Pd, and Ru) hydrogenate the guaiacol ring producing 2-methoxy cyclohexanol [71], with further deoxygenation to cyclohexane.

Metallic Pt, Sn and Pt-Sn bimetallic clusters supported on CNF (carbon nanofiber) catalysts were studied by Gonzalez et al.[89] for the gas-phase HDO of guaiacol and anisole at 400° C and 1 atm.

The study showed that the bimetallic catalysts were highly selective toward benzene. In particular, the Sn/CNF catalyst was effective in deoxygenating anisole, in which the acid functionality was capable of both oxygen removal and transalkylation, minimizing the loss of carbon. Gonzalez et al. suggested two possible routes for anisole deoxygenation: first, decomposition of the methoxy group forming phenol; second, a transalkylation reaction that is catalyzed by acid sites, where the methyl group from methoxy is transferred to another aromatic molecule, implying that two anisole molecules can form phenol and methylanisole, both of which can be deoxygenated to produce benzene and toluene, respectively. However, the excessive cost of noble metals makes it harder to scale up for industrial applications.

1.6. Transition metal phosphide, carbides and nitrides

Other studies have been carried out using metal phosphides for the HDO of guaiacol as a model compound. Zhao et al. [90] compared the activity of Ni_2P, Co_2P, WP, Fe_2P, and MoP supported on SiO_2 to two commercial catalysts (sulfided $CoMo/Al_2O_3$ and 5%Pd/Al_2O_3). The metal phosphide catalysts were more selective towards phenol, benzene and methoxybenzene, indicating minimal hydrogen consumption compared to the other catalysts. However, the main disadvantage of these types of catalysts is that they oxidize in water[91], in the same manner as typical hydrotreatment catalysts, producing phosphate which could clog the active sites of the catalyst and lead to deactivation.

Another group of catalysts reported to be active in HDO are supported and unsupported nitrides [73, 92]. Ghampson et al. [92] showed during HDO of guaiacol at 300 °C and 50 bar H_2 that pure phase Mo_2N favored the direct demethoxylation route, and that the addition of cobalt enhanced the deoxygenation activity of the catalyst. In another study, Ghampson et al. [73], reported that the activity and selectivity of Mo-based nitride catalysts can be tuned by the nitridation method (NH_3 or N_2/H_2 mixture) and surface treatment of the carbon support used. The authors reported that the best activity of their series was the one with the highest dispersion of Mo nitride.

Transition-metal carbide (W_2C and Mo_2C supported on carbon nanofiber (CNF)) catalysts were reported by Jongerius et al. [93] for the HDO of guaiacol at 350 °C and 55 bar of H_2 pressure. The conversion over the W_2C/CNF catalyst reached 66% and the main products were phenol and dimethylphenol isomers, while the conversion over Mo_2C/CNF reached 99% conversion with phenol and cresols as the main products.

Despite these promising results, metal nitrides and carbides require severe conditions for preparation: temperatures over 700 °C are required to prepare nitrides and over 1000 °C for carbides. This has implications on the economic feasibility of bio-oil upgrading.

1.7. Non-noble metal catalysts

Transition metals such as Fe, Ni and Co, which are typical hydrogenation catalysts, have reported worthy catalytic performance for HDO reactions. Olcese et al. [86] studied gas-phase HDO of guaiacol over an Fe/SiO_2 catalyst at 400 °C and found this catalyst to be highly selective towards the production of benzene and toluene. More importantly, this catalyst removed oxygen from guaiacol without hydrogenation of the aromatic ring.

The activity and selectivity of Ni/SiO_2 and Co/SiO_2 catalysts compared favorably to noble metal catalysts (Pt/SiO_2 and Pd/SiO_2) and sulfided $CoMo/Al_2O_3$ catalysts, according to Mochizuki et al., for the HDO of guaiacol in a batch reactor at 300 °C and 50 bar H_2 [94]. The Ni/SiO_2 catalyst produced cyclohexane and cyclohexanol as major products, while the Co/SiO_2 catalyst completely converted guaiacol into cyclohexanol. This shows that Ni/SiO_2 has greater potential as an HDO catalyst.

Nickel catalysts have received some level of attention in the literature for HDO reactions due to their strong hydrogenation activity. Bykova et al. tested Ni and NiCu catalysts supported on CeO_2-ZrO_2 and γ-Al_2O_3 for the HDO of guaiacol at 320 °C and 17 MPa H_2 in a batch reactor and observed ring hydrogenated compounds such as methylcyclohexane-1,2-diol and cyclohexanone as the main products [72]. Mortensen et al.[95] screened a series of catalysts(Ni/ZrO_2; Ni-V_2O_5/ZrO_2; Ni-V_2O_5/SiO_2; Ru/C; Ni/Al_2O_3; Ni/SiO_2; Pd/C; Pt/C), for the HDO of phenol at 275

°C and 10MPa of H_2 in a batch reactor. The Ni catalyst supported on ZrO_2 was the best performing catalyst, leading to the production of highly deoxygenated compounds. The authors also found that the nature of the support played a role in the activity and selectivity of the catalyst through adsorption and activation of phenol. A similar behavior was reported by Yakovlev et al.[96] who found, during the HDO of anisole over a Ni/SiO_2 catalyst, that the cooperative effect of metallic sites of Ni-Cu and acidic sites of the oxide support led to high deoxygenation degree.

Metallic Ni is frequently used as a promoter for W or Mo-based catalysts due to its ability to activate H_2 and promote reducibility [78]. Deoxygenation of phenol between a temperature range of 423 to 573 K was reported on Ni-W supported on activated carbon by Echeandia et al.[97] using different tungsten precursors. The authors found a synergistic effect with the addition of Ni regardless of the tungsten precursor used, and that the Ni-W catalysts were highly active in the complete deoxygenation of phenol. Furthermore, the catalysts were more stable than conventional sulfided $CoMo/Al_2O_3$ catalysts.

Anisole conversion was studied on Ni catalysts [98] supported on carbon, SBA-15, SiO_2 and Al_2O_3 in a batch reactor at 180 – 220 °C and 0.5-3 MPa of H_2. The main products observed were cyclohexyl methyl ether, cyclohexanol, cyclohexane, cyclohexyl ether, and small amounts of benzene. The catalysts transformed anisole first by hydrogenation, followed by hydrogenolysis of the $O\text{-}CH_3$ bond, producing cyclohexanol, which was then deoxygenated to form cyclohexane. Moreover, the support had a dramatic influence on the activity and product distribution. For instance, Ni supported on activated carbon exhibited poor deoxygenation activity while Ni/Al_2O_3 was capable of cleaving the C-O bond due to the stronger acid sites of the support. The Ni/SiO_2 catalyst, on the other hand, had the highest deoxygenation activity, producing principally cyclohexane.

1.8. Silica, Alumina and Silica-Alumina supports

The main function of a catalyst support is to disperse and stabilize the active phase. Catalyst supports play a fundamental role on the activity and selectivity of active metal phases in a number of reactions. Conventional supports used in HDO reactions are metal oxides with acidic or basic character, as well as activated carbons. All supports present different physico-chemical properties: surface areas ranging from 10 to 1200 m^2/g, different pore size and volume, and acidity.

The most common supports are alumina, silica, silica-alumina, zeolites, and activated carbon. They are the most convenient type of materials to use as supports due to their low cost and their chemical, thermal and mechanical stability.

Silica, SiO_2, is a chemically inert, highly adsorbent and thermally stable material. It is widely used as adsorbent, desiccant, chemical support and insulator in electronics. Another characteristic is that the SiO_2 surface contains silanol groups [-Si-OH] that are weakly acidic. In fact, it is less acidic than gamma-alumina[82] and zeolites [99] and it has been found to have low affinity for carbon formation [90].

Aluminum Oxide (Al_2O_3), also known as alumina, has several transitional phases such as gamma alumina (γ-Al_2O_3), delta alumina (δ-Al_2O_3), kappa alumina (κ-Al_2O_3), theta alumina (θ-Al_2O_3) and alpha alumina (α-Al_2O_3). Specifically, γ-Al_2O_3[100] is widely used as a catalyst support, due to its properties; strong Lewis acidity [101], high chemical inertness, strength and hardness, relatively large specific surface area, and good porosity. Gamma-alumina is also characterized as having high thermal stability which is dependent on the preparation method [102]. Finally, gamma-alumina has a spinel structure with defects [101, 103], containing a certain fraction of cation vacancies, which improves the interaction between the active component and the support.

Silica-Alumina (SiO_2-Al_2O_3) is used as an acidic support for many catalytic applications including hydrocracking, alkylation, oligomerization and isomerization, which are important in petrochemical industry processes [104-106]. It contains both Brønsted and Lewis acid sites. The properties of silica-alumina depend on the preparation method, Si/Al ratio and pretreatments.

1.9. Scope of thesis

Biomass is considered a promising source of renewable energy and helps decrease our dependence in fossil fuels. Lignocellulosic compounds derived from fast pyrolysis of biomass have the potential to be an alternate source of fuels and commodity chemicals. However, bio-oil must be refined prior to any application, due to its high oxygen content. A possible route of transformation to improve bio-oil properties involves partial or total removal of oxygenated groups present, through a general class of reactions known as catalytic hydrodeoxygenation (HDO). A number of reaction pathways have been identified over different types of catalysts for representative model compounds. The intrinsic activity depends on a variety of experimental factors. Hence, it is necessary to explore optimal conditions to find suitable catalysts for this task. This work involved a study of unsupported tungsten oxide and supported nickel catalysts for the conversion of 2-methoxyphenol(guaiacol) as a model compound.

Previous work with WO_3 catalysts showed that the composition of the active phase, formed during pre-activation in hydrogen, was a reduced hydrogen bronze, H_xWO_{3-z}. The composition varied with pre-activation temperature and the hydrogenation of acrolein was optimal over a narrow composition range. Therefore, initial work focused on measuring the rate of guaiacol conversion as a function of the pretreatment temperature. A distribution of products were identified and so reactions at low conversion were carried out to establish the main reaction pathway from guaiacol to cyclohexane. The conversion was then measured as a function of guaiacol concentration and hydrogen pressure to establish the kinetic rate law. Understanding the mechanism involved in the conversion of guaiacol over reducible oxides is important in order to comprehend, to a deeper extent, the factors controlling the activity and selectivity of the HDO reactions.

Nickel-based catalysts have been more widely studied but still, much more information is required to understand the role of metal hydrogenation sites and acid dehydration sites in controlling activity and selectivity. Initial work varied the catalyst support at constant metal loading to determine how interaction of the support with the metal-controlled dispersion and gave the highest activity. Next, the metal loading was varied to design an optimum catalyst, which can be more efficient, active and selective for the HDO reactions.

The general objective of this thesis is to study supported and unsupported catalysts suitable for HDO of guaiacol as a model compound.

Objectives:

1. Study the effect of pre-activation temperature and reaction temperature of unsupported WO_3 on the HDO activity of guaiacol.
2. Study the effect of H_2 pressure and guaiacol concentration on the HDO activity of guaiacol with unsupported WO_3 for a specific activation temperature of 350 °C.
3. Verify the reaction pathway by feeding intermediates found in the product distribution of guaiacol with unsupported WO_3.
4. Propose a possible reaction mechanism and rate law for tungsten catalyst during HDO of guaiacol based on the results.

5. Evaluate the effects on the activity and selectivity of Ni catalysts for the conversion of guaiacol and the nature of the acid sites on the SiO_2, Al_2O_3, and Al_2O_3-SiO_2 supports.
6. Study varying nickel loadings using Al_2O_3 as support and evaluate activity and selectivity for HDO of guaiacol.

The organization of the thesis is as follows: Experimental methods are presented in Chapter 2. The results and analysis of the reactions of guaiacol and related compounds over H_xWO_3 bronze catalysts are presented in Chapter 3. The study of Ni supported catalysts for HDO of guaiacol is given in Chapter 4. A summary and suggestions for future work is provided in Chapter 5.

CHAPTER 2

EXPERIMENTAL METHODS

This chapter presents a description of the materials and methods used for the work reported. In addition, procedures of the evaluation of bulk tungsten oxide and supported nickel as catalysts for the HDO of guaiacol in both the trickle bed reactor (TBR) and batch reactor, respectively, are described. The methodology used in the product analysis and a brief overview of the characterization techniques used are also included.

2.1 Nitrogen Adsorption Isotherms

This technique is widely used to determine textural properties of a solid material, which is fundamental for determining the surface area and porosity of heterogeneous catalysts. Whenever a gas is brought into contact with the surface of a solid, the gas will adsorb on the surface of the solid forming a thin layer. When the pressure of gas molecules is raised, it enhances the formation of multilayers. Nitrogen and argon adsorption (at -196 °C) are considered to be the most suitable methods to determine the surface area of non-porous and porous materials in the microporous and mesoporous range.

The initial step of the procedure involves evacuating the adsorbent by heating the solid at elevated temperature under high vacuum. Heating the sample under vacuum ensures the removal of weakly adsorbed molecules, cleaning the internal surface of the solid. The sample is then cooled down to

-196 °C (77 K) followed by dosing known amounts of nitrogen. An adsorption isotherm is obtained by measuring the amount of gas adsorbed across a wide range of relative pressures at a constant temperature. On the other hand, desorption isotherms are achieved by measuring gas removed as pressure is reduced.

The interaction strength between the gas molecules and the pore wall of the solid will define the shape of the isotherm formed.

The International Union of Pure and Applied Chemistry (IUPAC) have classified porous materials as follows [107];

Micropores: < 2 nm

Mesopores: between 2 and 50 nm

Macropores: > 50 nm

The shape of adsorption isotherms identified by IUPAC are grouped into six types, as shown in Fig. 2.1 [108]. Different shapes are obtained depending on the behavior of gases adsorbed by different pore sizes.

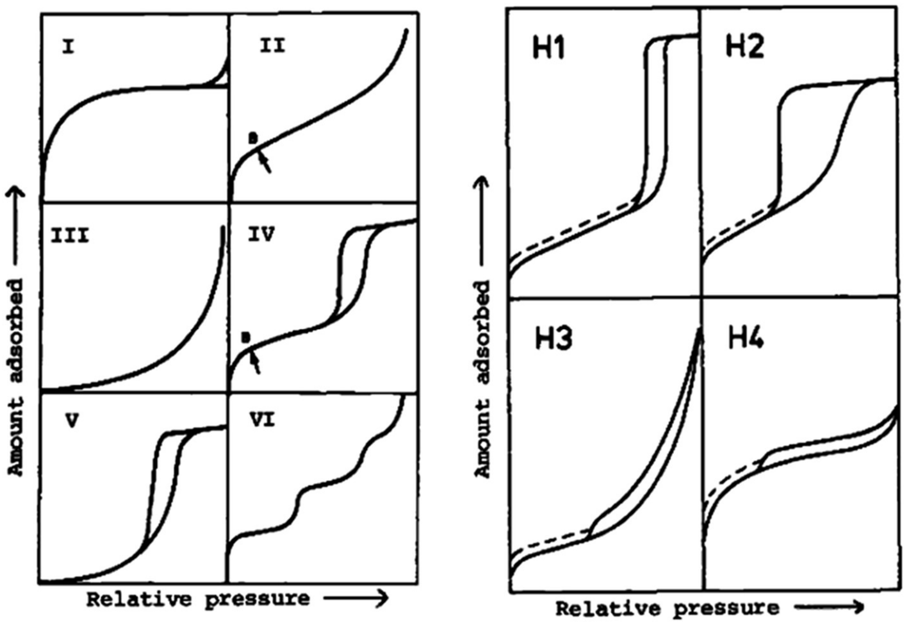

(A)

(B)

Figure 2.1 (A): Types of sorption isotherm; (B): Types of hysteresis loop. See text for details. Reproduced from Sing et al. [109].

The materials studied in this thesis present two out of the six types of isotherms. The Type I isotherm is typical for microporous materials: adsorption is limited to the completion of a single monolayer of adsorbate at the adsorbent surface. Complete filling of these narrow pores occurs at low relative pressure forming a monolayer.

The Type IV isotherm, characteristic of mesoporous materials, has a hysteresis loop which is associated with capillary condensation. The pores are completely filled at high relative pressure and the plateau region indicates when the pores are completely filled.

Following an earlier classification by de Boer, IUPAC published a revised classification of hysteresis loops of various shapes present in mesopores. Hysteresis loop H1 shows nearly vertical and parallel branches which indicates a very narrow distribution of cylindrical-like pores. [109, 110]. Materials with type H2 loops are characteristic of complex pore structure and do not have a well-defined distribution of pore size. The type H3 is observed in porous materials formed from aggregates, where the capillary condensation happens in a non-rigid framework and an undefined porosity. Type H4 is characteristic of complex materials containing both micro and mesopores and is similarly associated with narrow slit-like pores.

The method most widely used for the determination of surface area of porous materials is the BET (Brunauer, Emmet, and Teller) [111]. The low-pressure portion of most isotherms can be transformed into a line using the BET equation,

$$\frac{1}{V({}^{P}/_{P_0} - 1)} = \frac{1}{V_m C} + \frac{C-1}{V_m C}\left(\frac{P}{P_0}\right), \tag{2. 1}$$

where P_0 and P are the saturation pressure and equilibrium pressure of the adsorptive, respectively; V is the volume of gas adsorbed; V_m is the monolayer volume of adsorbate; and C is the BET constant, related to the heat of adsorption of the adsorbate.

V_m and C in equation 2.1 can be estimated from the slope and intercept of the linear BET plot, i.e. $\frac{1}{V({}^{P}/_{P_0}-1)}$ versus $\left(\frac{P}{P_0}\right)$. Consequently, the specific BET surface area S_{BET}, m^2/g can be calculated as follows:

$$S_{BET} = \frac{V_m\ N_A\,\sigma}{22414\,\frac{cm^3}{mole}\ x\ W} \tag{2. 2}$$

where V_m is the monolayer capacity at STP conditions, N_A is Avogadro's number (6.02×10^{23} mol^{-1}), σ is the cross-sectional area of an adsorbate molecule ($\sigma = 0.162$ nm^2 for nitrogen) and W is the mass of the sample (g).

Nitrogen adsorption/desorption isotherms were measured at 77K using a Micromeritics ASAP-2020 instrument to determine the BET specific surface area (SBET). Prior to the analysis, the samples were degassed at 150 °C for 6 h.

2.2 X-Ray Diffraction (XRD)

X-ray diffraction is a method able to provide qualitative and quantitative information on crystalline compounds present in a solid, based on the fact that each crystalline substance, presents a unique diffraction diagram. Thus, a diagram of an unknown sample can be compared to a standard (known) sample and determine its identity and chemical composition. In this thesis XRD was used to determine the phase composition of heterogeneous catalysts. An incident x-ray beam interacts with the solid material to be studied. The interaction between the X-rays and the electrons present give rise to a dispersion phenomenon. When dispersion occurs constructive and destructive interference is produced between the dispersed x-rays. The distances between the dispersion centers are of the same order of magnitude as the radiation wavelength. The resulting diffraction gives intensity patterns that can be interpreted according to the location of the atoms in the crystal, satisfied by Bragg's law, $n\lambda = 2dsin\theta$, where the incident radiation is of wavelength λ, the distance between two lattice planes is d, the diffraction angle is θ, and the integer order of reflection is n.

X–Ray Diffraction is also used to estimate the average crystallite size (D) of a material from the width of a diffraction line, using the Scherrer equation[112],

$$D_p = \frac{K\lambda}{\beta_{1/2}cos(\theta)}, \tag{2. 3}$$

where $\beta_{1/2}$ is the full width at half maximum of the diffraction peak at 2θ(in radians) and K is a geometric shape factor, typically taken to be 0.94.

2.3 Transmission Electron Microscopy (TEM)

TEM is a valuable characterization technique to analyze particle size and morphology of the surface of catalytic materials. In TEM, the sample is illuminated by an electron beam, electrons are transmitted through a very thin layer of sample, and an image is formed through the interaction of the electrons and the specimen. The instrument was used in bright field mode, where contrast is formed by occlusion and adsorption of electrons in the sample. Dark areas or regions of the sample are produced where there are atoms of a higher atomic number.[113]. Digital image processing was performed to determine the particle size information of a particular region. Dark-field mode allowed us to obtain data for diffraction patterns. [114].

The analysis was carried out using a Jeol Model JEM-1200 EXII System. Samples were ground and dispersed in methanol, then transferred to a copper grid (methanol dispersion method). To obtain the Ni particle size, a histogram study of the micrographs for over 300 particles of catalysts was performed using Image Tool 3.0 image processing software.

2.4 Surface Acidity

In catalysis, surface acidity plays an important role on the behavior of different catalytic materials on many applications applied to chemical industries. [115]. Thus, understanding the acidic nature of solid surfaces is an important parameter for ion exchange and catalysis. Total acidity methods for solid catalysts have been developed by numerous authors: Benesi method using Hammett indicators [116], chemisorption of ammonia [115], pyridine-thermobalance method [117], FT-IR spectra of adsorbed pyridine, and the potentiometric titration method [118]. The potentiometric method developed by Cid and Pecchi [118] measures the acid strength distribution during titration of a suspension, made up of a small quantity of 0.1 N n-butylamine in acetonitrile containing a known mass of solid catalyst, with the same base.

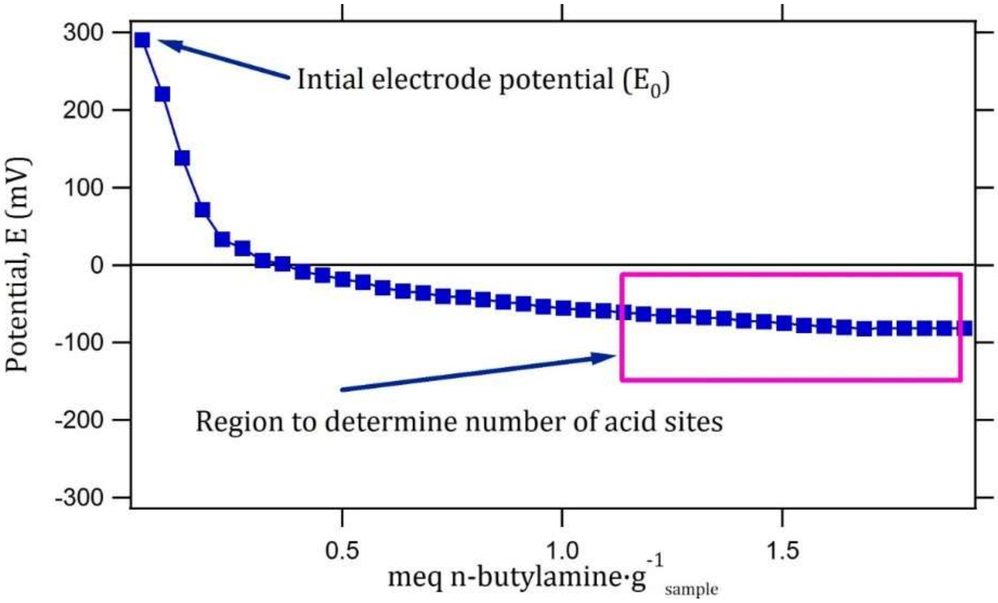

Figure 2.2 Potentiometric Titration Curve; Figure Courtesy of T. Ghampson.

The maximum acid strength of the surface acid sites on the catalyst is estimated from the initial electrode potential on the titration curve obtained as shown in Figure 2.2. In addition, the total number of acid sites (meq/g_{solid}) can be estimated from the point on the titration curve where the plateau is reached.

The method of potentiometric titration was used to determine the acid strength and the total number of acid sites (Lewis & Brønsted) for both supports and catalysts in the oxide and reduced states.

All the catalysts and supports were reduced ex situ at 500 °C under flowing H_2 at 100 mL/min for 4 h. Catalyst samples (150 mg) were dispersed in a beaker containing 90 mL of acetonitrile (Merck, 99%), adding 0.05 mL of 0.1 mol L^{-1} n-butylamine solution in acetonitrile. The titrant solution was added from a micro burette with side reservoir (Kimble, tolerance of ± 0.02 mL). The suspension was left under agitation for 3 h, before the initial potential was recorded; then 0.05 mL was added every 2 min until the potentiometric curve reached a constant potential. The variation in electric potential was registered on a Sartorious Instrument (PB-11) pH/mV meter using an Ag/AgCl electrode as shown in Figure 2.3. The pH meter was standardized using a buffer at pH 7 and pH 10

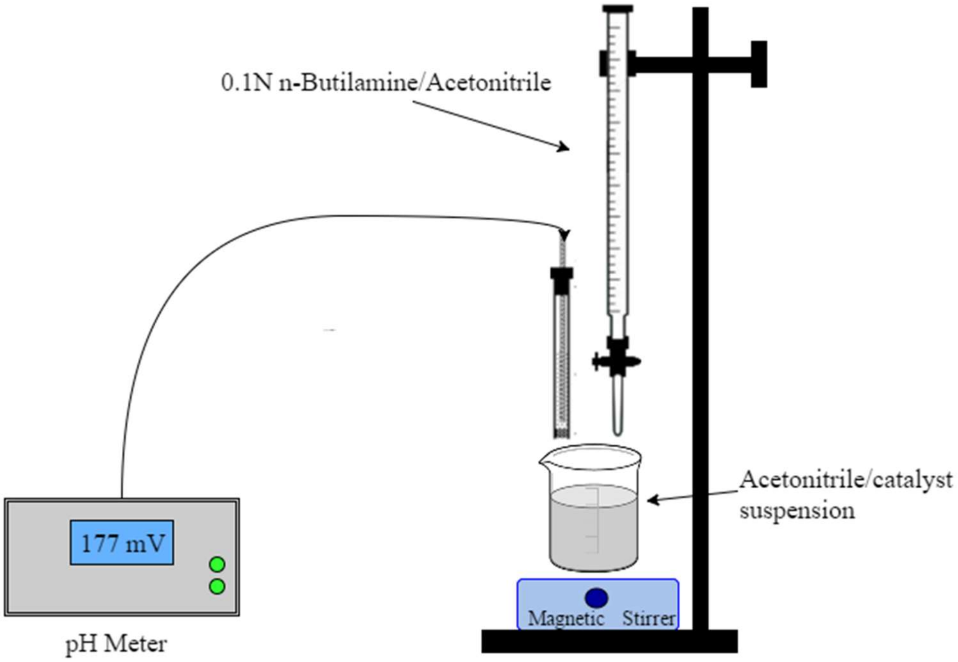

Figure 2.3 Instrument to determine total acidity

To quantify the strength and number of acid sites, the following criteria were used:

The initial potential from the electrode, E_0, is a measurement of the acid strength of surface sites according to the following [118] classification:

	E0 > 100 mV	very strong acid sites
0 <	E0 < 100 mV	strong acid sites
-100 <	E0 < 0 mV	weak acid sites
	E0 < -100 mV	very weak acid sites

Number of acid sites (or acid sites density)

$$\text{Total acidity} = \frac{(0.1 * \text{used volume})}{(\text{mass sample})} * \left(\frac{\text{mmol}}{\text{g}}\right)$$

2.5 X-ray photoelectron spectroscopy (XPS)

X-ray photoelectron spectroscopy provides qualitative and quantitative information about all the elements present. XPS provides information of the molecular surroundings (oxidation states, neighboring atoms).

XPS is performed in an ultrahigh vacuum environment where incident energetic photons cause emission of photoelectrons from a material. It operates on the principle of Einstein's photoelectric effect, where the photon interacts with an electron of an atomic orbital transferring the total energy from the photon to the electron, giving rise to a photoelectron emission, where the kinetic energy of the ejected electron, E_k, is;

$$E_k = h\nu - \varphi - BE, \quad (2.4)$$

where hν is the energy of the incident photon, the work function of the spectrometer is φ, and the binding energy of the emitted photoelectron is BE. A sufficiently energetic incident radiation may cause the ionization of electrons from a number of different core energy levels in a sample, thereby producing a spectrum of all accessible energy levels [119]. An XPS spectrum gives qualitative information of components of a sample from chemical shifts of binding energies of ejected electrons peculiar to the elements on the surface of the sample. The intensities of the signal are used to quantify elements present on the surface of the sample.

X-ray photoelectron spectra of the reduced catalysts were recorded on a VG Microtech Multilb 3000 electron spectrometer using a Mg Kα (1253.6 eV) photon source, with hemispherical analyzer. The binding energies (BE) were referenced to the C 1s level of the carbon support at 284.8 eV. An estimated error of ± 0.1 eV can be assumed for all measurements. The intensities of the peaks were calculated from the respective peak areas after background subtraction and spectrum fitting by the standard computer based statistical analysis which included fitting the experimental spectra to a sum of Gaussian and Lorentzian lines (90G-10L) using a least squares minimization procedure for $\chi 2$ with the help of the XPS peak program. Relative surface atomic ratios were determined from the corresponding peak areas, corrected with tabulated sensitivity factors [120] with a precision of 7%. All measurements were taken at the laboratory of Dr. José Luis García Fierro, from Instituto de Catálisis y Petroleoquímica (ICP) del CSIC, Madrid-Spain and the department of Reffinagge of the Institute Ircelyon, Lyon-France.

CHAPTER 3

TUNGSTEN OXIDE BRONZES AS ACTIVE PHASE IN HYDRODEOXYGENATION OF GUAIACOL

3.1 Introduction

Tungsten oxide (WO_3) is an acidic metal oxide which has been applied as heterogeneous catalyst either as an active phase, a precursor to other active phases, or a support for a wide variety of reactions, such as hydrotreatment, isomerization, metathesis and alcohol dehydration. Sulfided W/C catalysts [121] prepared from different tungsten precursors were studied for simultaneous HDS of thiophene and hydrogenation (HYD) of 1-pentene. It was found that the W/C catalysts were much more active in HYD than HDS at 498 K and the activity depends on the precursor used. Ni was added to the catalysts and a synergistic effect was observed on the overall activity for HDS and HYD, in which specific sites exist for both thiophene and 1-pentene species.

W/Al_2O_3 and WP/Al_2O_3 [122] catalysts, prepared at different pH, were studied for simultaneous HDS of gas oil and HDN of pyridine. Addition of phosphorus to the surface of the catalyst improved the HDS activity, attributed to an increase in homogeneity of tungsten on alumina, which helps to promote the reaction. In contrast, there was no noticeable effect on the HDN of pyridine with phosphorus addition. The authors found that the overall activity of these catalysts depends on several preparation factors such as impregnation pH, phosphorous addition, and type of precursor used.

WO_3 has also been used as a support in Pt/WO_3 catalysts [123], where the hydrogenation of acrolein was reported. The desirable conversion pathway for acrolein would be to propene, because it involves the cleavage of the C=O bond leaving the C=C intact, thus reducing the H_2 consumption in the reaction. Zegaoui [123] reported the use of reducible metal oxides MoO_3 and WO_3, both containing Pt, following pretreatment under hydrogen at temperatures between 130 – 350 °C. Thibodeau, et al. determined that the pretreatment produces a non-stoichiometric phase known as hydrogen bronze H_xWO_3 (x is in the range of 0.9-1.3) [124]. The authors found that the conversion of acrolein depends on the pretreatment conditions. Thibodeau et al. found that a narrow pre-activation temperature was necessary for the catalyst to be selective to hydrogenation of acrolein.

In general, non-noble metal catalysts such as Ni and W are considered to have great potential for HDO because they are non-sulfide catalysts which do not require severe conditions for activation.

3.2 Materials and Methods

3.2.1 Reactants and catalyst precursors

All materials used in the preparation of tungsten oxide catalysts and the reactants used in the hydrodeoxygenation (HDO) reactions are shown in Table 3.1.

Table 3.1 Reactants and catalysts precursors

Name	Formula	Manufacturer
Ammonium	$(NH_4)_6H_2W_{12}O_{40}$*xH_2O	Sigma Aldrich, puriss p.a.
2- Methoxyphenol	$C_6H_4(OH)(OCH_3)$	Acros, 99.9%
Phenol	C_6H_5OH	Acros, 99.5%
Cyclohexanol	$C_6H_{11}OH$	Sigma Aldrich, 99%
Dodecane	$CH_3(CH_2)_{10}CH_3$	Fisher, 99%
Hexadecane	$C_{16}H_{34}$	Sigma Aldrich, 99%
Hydrogen	H_2	Ultra-high purity, Matheson

3.2.2 Bulk Tungsten Oxide Synthesis

Bulk tungsten trioxide was prepared by thermal decomposition of ammonium metatungstate hydrate, $(NH_4)_6H_2W_{12}O_{40}$*xH_2O. The furnace used was two feet long with a 2-inch diameter quartz tube fitted with end caps that allowed atmospheric control. Approximately 5 g of precursor was loaded into a 4 x 0.5 x 0.5-inch ceramic boat and heated to 500 °C at 1 °C per minute and then held for 4 hours under flowing air (5 mL min-1). The air flow rate was measured with a bubble meter.

3.2.3 Trickle bed reactor (TBR) schematic

All HDO experiments using model compounds were carried out in a vertical stainless steel continuous-flow trickle bed reactor depicted in Figure 3.1. The reactor tube was a ¾" diameter stainless steel tube.

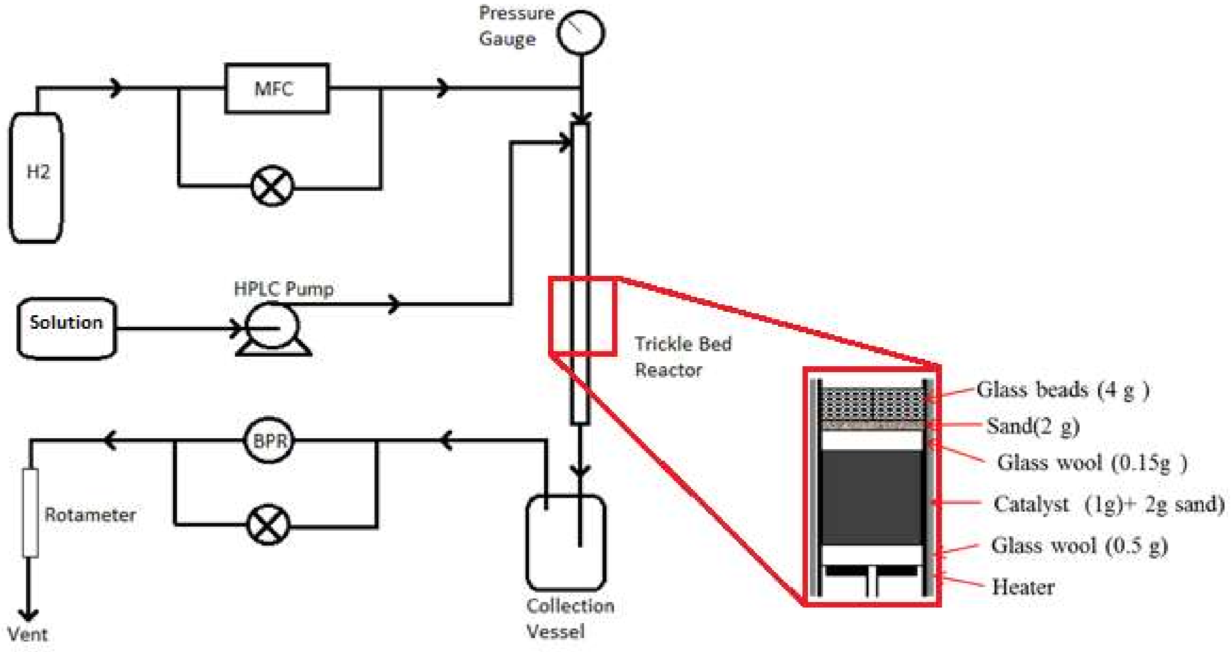

Figure 3.1 Trickle Bed Reactor and Bed Packing.

The reactor was packed with catalyst according to the expanded drawing in Figure 3.1. A typical experiment had approximately 1 g of catalyst diluted with 2 g of sand. Firstly, a stainless-steel rod was placed inside the reactor tube, 0.5 g of glass wool was loaded into the reactor, after packing it tightly downwards a homogeneous mixture of the catalyst powder and sand were added and packed down as well, then 0.2g of glass wool were introduced on top of the powder mixture, used to keep the catalyst fixed in the reactor. Finally, 2 g of sand and 4 g of glass beads were added on top of the catalyst bed which helped homogenize temperature and ensure that the liquid entering the reactor reached the desired temperature before touching the active catalyst bed.

3.2.4 Activation of tungsten oxide catalyst

Reduced tungsten oxide hydrogen bronzes were prepared in-situ, following previously reported procedures by Thibodeau et al. [125], by flowing H_2 in the continuous flow reactor. Previous data suggests that tungsten oxide bronzes are unstable when air is present; therefore, all catalysts were activated in-situ and used immediately to avoid combustion of the active bronze phase. Prior to catalytic testing, bulk WO_3 was activated to tungsten oxide bronzes (H_yWO_{3-z}) under a flow of H_2 with a flow rate of 100 mL min^{-1} at atmospheric pressure. The reactor shown in Fig 3.1 was wrapped with heating tape that was connected to a Variac Model 3PN1010B regulated by a temperature controller (Micromega). An insulating tube was used to cover the whole reactor to keep the temperature constant throughout the experiment. The temperature was measured inside the reactor using a thermocouple, connected through a thermowell which is in contact with the catalyst bed.

The catalyst bed was heated at a rate of 10 °C min^{-1} to the selected temperature within the range 250 – 400 °C and held for 10 h (7 different temperatures were used within this range in 25 °C increments), using the same activation procedure reported by Thibodeau et al. [125]. After the 10 h treatment the reactor was heated or allowed to cool under flowing hydrogen until the desired reaction temperature was reached.

3.2.5 Catalytic activity measurements on trickle bed reactor

The feed solutions used for each set of experiments were guaiacol, phenol or cyclohexanol at a concentration of 0.232 mol L^{-1} in dodecane; hexadecane was used as an internal standard for quantitative GC analysis. Each model compound was introduced separately into the reactor using an HPLC pump (series III). The liquid reactant mixture and hydrogen were connected to the reactor inlet where they flowed downward through the catalyst bed. The HDO reaction temperatures used were 300, 325 or 350 °C. The hydrogen pressure was maintained at 4 MPa by a backpressure regulator, H_2 flow rate of 22.2 mL min^{-1}. The liquid feed rate of 0.1 ml min^{-1} corresponded to a liquid hourly space velocity (LHSV) of 43 h^{-1}.The H_2 gas hourly space velocity (GHSV) was 3600 h^{-1}.

$$LHSV = \frac{F}{m_{cat} * d^{-1}} \tag{3.1}$$

3.2.6 GC Data Analysis

Samples were analyzed by gas chromatography (GC). The liquid samples were collected in sealed septum vials and analyzed using a gas chromatograph (Thermo Scientific, GC Ultra) equipped with a flame ionization detector (FID) and a Stabilwax column (Agilent, 30 m × 0.53 mm ×1.0 µm film thickness).

The split/splitless injector and FID were held at 310 °C. The sample was directly injected ”neat” onto the column with 50:1 split ratio and 1 uL of injected volume. The GC oven program consisted of an initial temperature of 40 °C, followed by a heating rate of 8 °C min^{-1} to 125 °C without holding time, and a subsequent heating rate of 40 °C min^{-1} to 250 °C and held for 11 min. The product distributions were identified by their column retention time in comparison with available standards at the same conditions.

3.3 Results

3.3.1 Material characterization

3.3.1.1 Specific surface area

Nitrogen adsorption isotherms were measured for the three batches of WO_3 synthesized for the work in this thesis. The isotherms were similar and the total pore volume at P/P0 of 0.03 cm^3/g showed that the material was essentially non-porous. A representative isotherm is shown in

Figure. 3.2 A. The pore size distribution, as analyzed with the BJH model for cylindrical pores, from the desorption isotherm, is shown in Figure 3.2 B. The maximum in the pore size distribution is near 25 nm, probably due to void spaces between aggregated nanoparticles. The BET specific surface areas are shown in Table 3.2. The C parameter is within the acceptable range of 50 – 150, indicating that intermolecular interactions between the adsorptive (N_2) determine the packing in the monolayer.

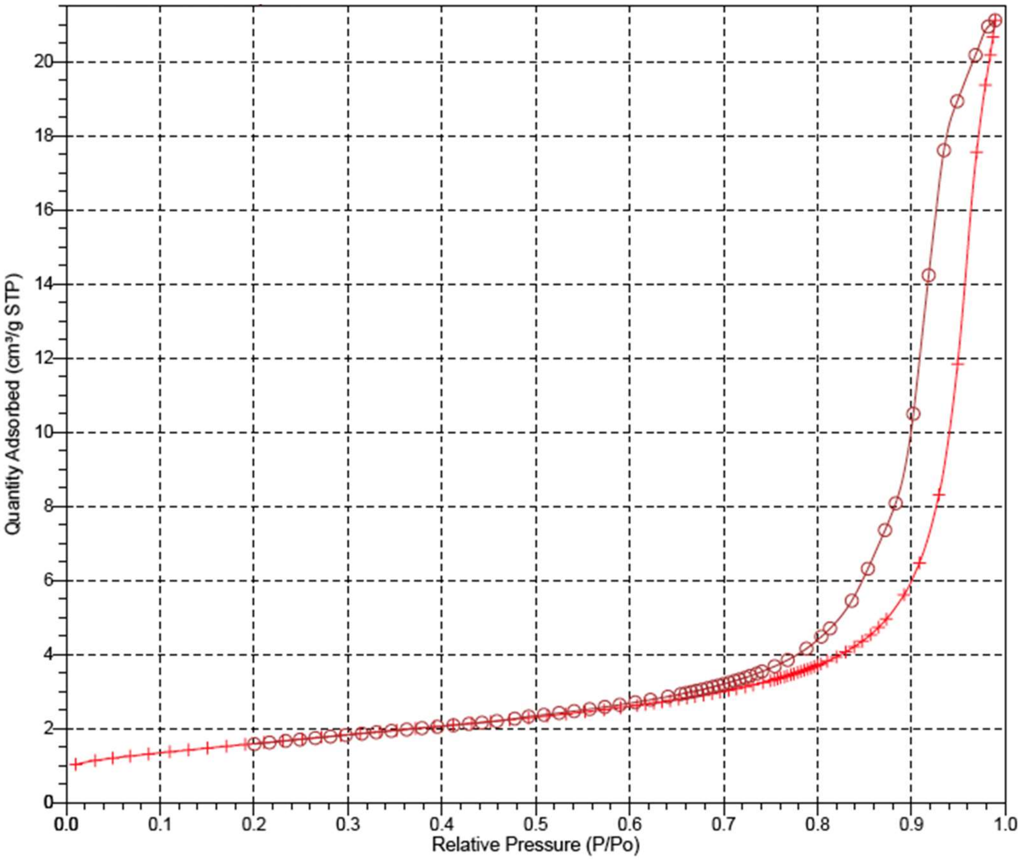

Figure 3.2. Top: Nitrogen adsorption (+) and desorption (o) isotherm; and Bottom: BJH pore size distribution for WO_3 catalyst synthesized in this work.

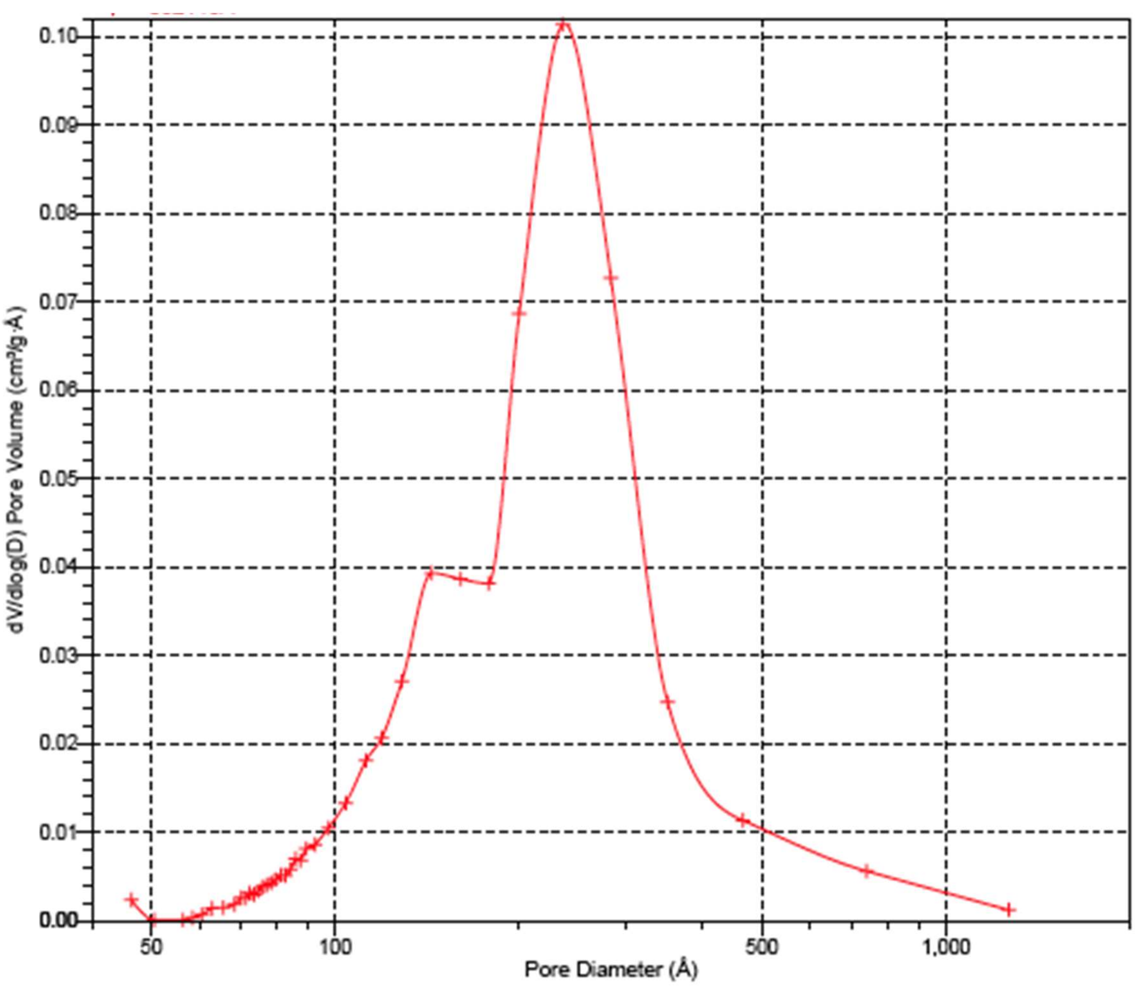

Figure 3.2. Continued.

Table 3.2. BET Surface areas of WO_3 materials synthesized

Batch	**BET area (m^2/g)**	**C**
#1 030813	6.00 ± 0.03	128
#2 031013	5.75 ± 0.01	150
#3 031113	5.75 ± 0.03	111
Average:	5.8± 0.1	

3.3.1.2 XRD of as-prepared and post-reaction catalysts

XRD patterns of powdered samples were recorded on a PANalytical X'Pert PRO X-ray diffractometer equipped with a graphite monochrometer and CuKα radiation (45 kV, 40 mA) in a parallel beam optical geometry. The standard scan parameters for bulk material identification were 15-85° 2θ with a step size of 0.02° and a counting time of 1 s per step. Identification of the phases was achieved by reference to JCPDS diffraction file data.

Figure 3.3 shows XRD patterns for three batches of WO_3 synthesized for this work. The phase was assigned to monoclinic WO_3 on the basis of JCP card 04-008-1962. Because the diffraction patterns and specific surface areas were similar, the material from the three batches was mixed together to provide sufficient catalyst for the reaction studies.

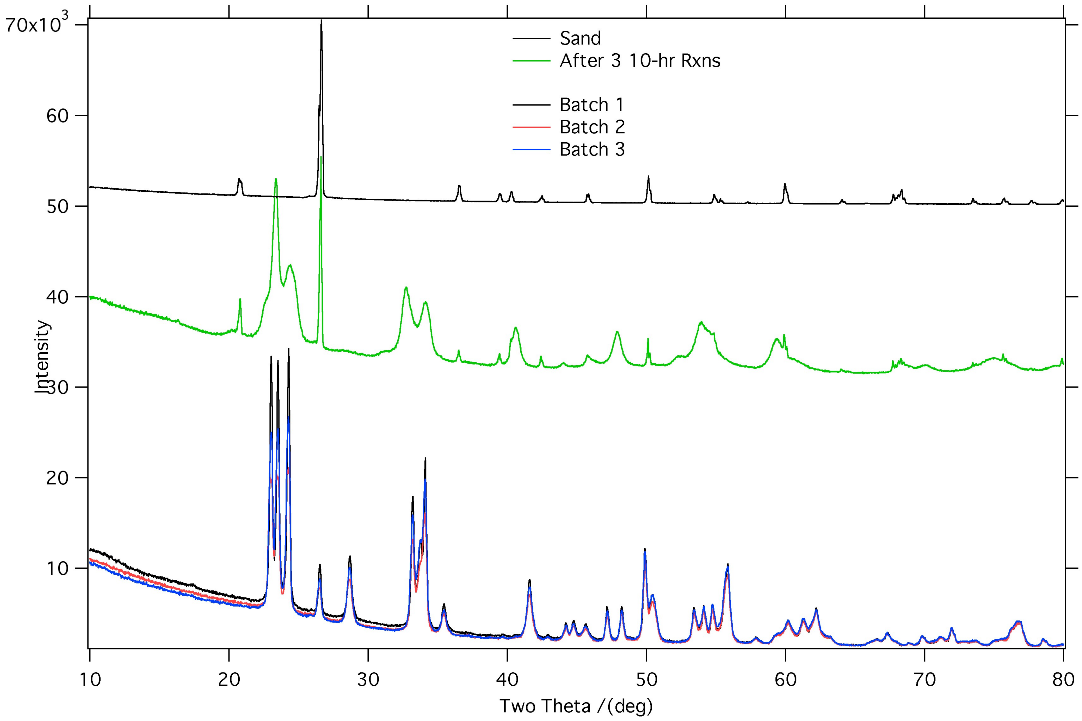

Figure 3.3. XRD patterns of the as-synthesized WO_3 and after activation in H_2 and three 10-hour guaiacol reactions in the trickle bed reactor.

After activation in H_2 and three 10-hour reactions in the trickle bed reactor, the catalyst was removed and analyzed by XRD. Distinct changes in the XRD pattern show that the catalyst was transformed under reaction conditions and was no longer stoichiometric m-WO_3. The sand used as bed support accounts for a number of sharp peaks, which can be assigned by reference to the diffraction pattern of pure sand, shown in Figure 3.3. As the hydrogen bronze reacts rapidly with oxygen, the XRD pattern post-reaction is unlikely to be representative of the active phase under reaction conditions; therefore, detailed analysis of the pattern was not of direct relevance. In-situ

XRD measurements of the active catalyst would be interesting but require specialized high pressure/temperature environmental cells.

3.3.2 Catalytic Activity of Reduced WO_3

Bulk tungsten oxide bronzes have been tested previously by Thibodeau et al. [125] as an active phase for the hydrogenation of acrolein to allyl alcohol and the hydrodeoxygenation of the latter to propene. For the catalyst to be active, pre-activation under flowing hydrogen is required. For the gas phase hydrogenation of acrolein in a continuous flow reactor, there is an optimum activity at a pretreatment temperature of 350 °C, corresponding to a composition of $H_{1.29}WO_{2.77}$ [125]. Similar experiments to establish the steady state activity and dependence on activation temperature were performed for hydrodeoxygenation of guaiacol in the liquid phase trickle bed reactor.

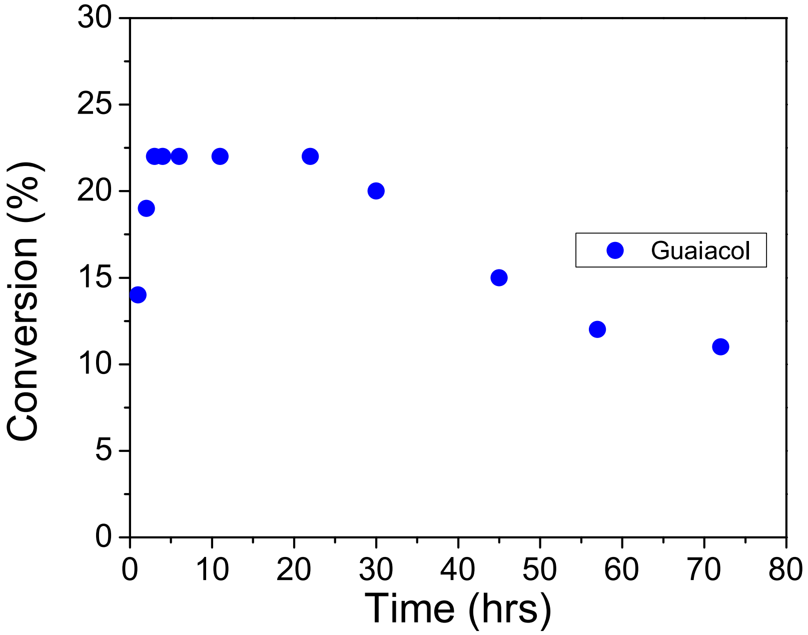

Figure 3.4 Guaiacol conversion over tungsten oxides bronze, 72 h on stream.

Figure 3.4 shows an example in which the WO_3 catalyst was pretreated and tested in the trickle bed reactor at 325 °C under flowing hydrogen at 3 MPa for 10 h as previously described in Section 3.2.4, and then after starting the guaiacol reactant flow, the product mixture was sampled for an extended period of time on stream. Figure 3.4 reveals several regimes regarding the activity and stability of the WO_3 bronze for conversion of guaiacol. The activity of the pre-reduced catalyst increases rapidily, achieving steady state conditions within the first 3 hours. The activity reaches a maximum of 22% between the 3rd and is constant until the 22nd hour on stream, but after that period the catalyst activity decreased to about 11% conversion when it reaches 72 hours on stream.

The initial composition of the bronze after activation at 325 °C was expected to be similar to the m-WO_3 nanopowder (9 m^2/g) determined as $H_{0.95}WO_{2.78}$ using thermogravimetric methods. During hydrodeoxygenation, proton transfer and C-O bond breaking steps occur, and dissociative adsorption of H_2 is needed to replenish the reservoir of hydrogen in the bulk as well as create surface oxygen vacancies via hydroxyl formation and dehydroxylation [125]. The decrease in conversion after 22 hours on stream suggests that the rate of hydrogen up-take was not sufficient to maintain the initial surface oxygen vacancy coverage (i.e. Lewis acid sites) or the surface hydroxyl coverage (i.e. Brønsted acid sites). Further work is required to investigate this behavior, but subsequent studies of the reaction rate and mechanism were limited to the steady state regime following the initial start-up transient.

3.3.3 Effect of pre-activation of WO_3 in the conversion of guaiacol

Figure 3.5 shows the conversion of guaiacol after reacting steady state conditions at three reaction temperatures, 300, 325, and 350 ºC for activation temperatures from 250 to 400 °C. The figure shows that the conversion of guaiacol gradually increased with increasing pre-activation temperature of WO_3 catalyst, as well as the expected Arhenius behavior in which conversion increases when the reaction temperature was increased. Thibodeau et al. [125] studied the composition of WO_3 catalysts at different pre-activation temperature. They reported that hydrogenation of acrolein to allyl alcohol reaches a maximum over a narrow pre-activation temperature. For the conversion of guaiacol, the behavior is distinctly different.

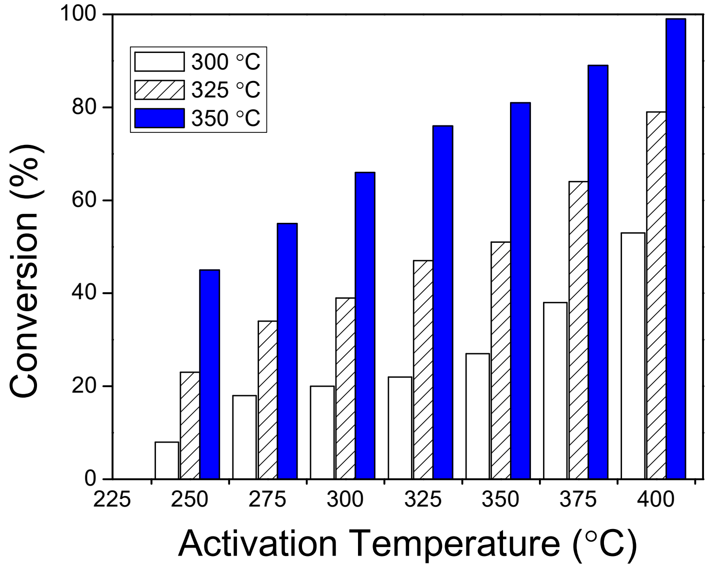

Figure 3.5 Effect of pre-activation temperature vs Reaction temperature on guaiacol conversion over of WO_3 Bronzes.

3.3.4 Acid site characterization

The type of acid sites can be determined from adsorption of pyridine. DRIFTS measurements were performed within the group, by Akbar Mahdvi-Shakib, for a mesoporous WO_3 material (70 m^2/g) synthesized by the Landry group at the Univ. of Vermont. As shown in Fig. 3.6, adsorption of pyridine at room temperature on the as-received WO_3 material gives bands attributed to both Lewis and Bronsted acid sites. After formation of the bronze by heating in H_2 at 200, 250, and

300 °C, pyridine adsorption shows an increase in the pyridine mode at 1535 cm^{-1} due to adsorption on Brønsted acid sites, relative to the mode at 1577 cm^{-1} assigned to adsorption on Lewis acid sites. The ratio of Bronsted to Lewis acid site adsorption as a function of hydrogen pretreatment temperature is shown in Figure 3.7. Notice that as the bronze forms and becomes more metallic, the background absorbance increases and the absolute magnitude of the change in absorbance decreases due to scattering of the infrared light. Similar measurements were not possible on the lower surface area materials (9 m^2/g) or on the mesoporous WO_3 materials at activation temperatures above 300 °C. Nevertheless, the DRIFTS data show that there is a strong increase in the Brønsted to Lewis acid site ratio with increasing H_2 activation energy which correlates with the increasing conversion observed in the guaiacol reaction data of Fig. 3.5, suggesting the role of Brønsted sites in the rate controlling step of the reaction.

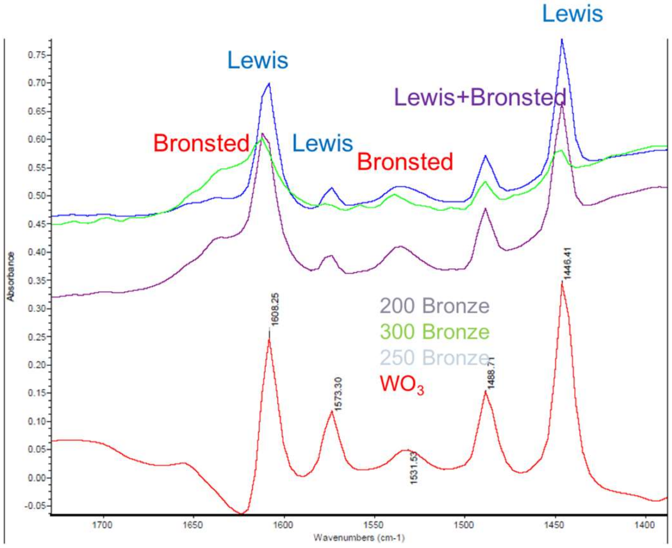

Figure 3.6 DRIFTS spectra for adsorption of pyridine on mesoporous WO_3 and for bronze formed by heating in H_2 at the indicated temperatures. Measurements courtesy of A. Mahdavi-Shakib.

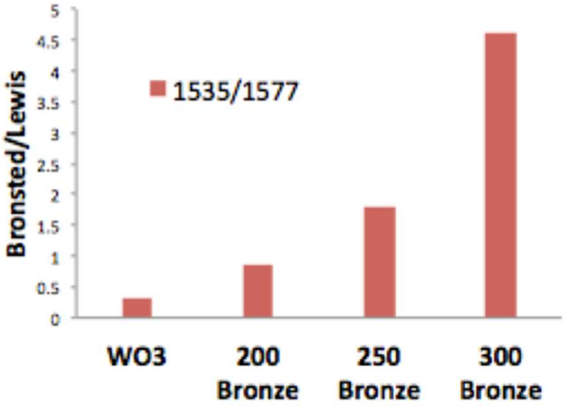

Figure 3.7. Brønsted to Lewis acid ratio as determined from the integrated peak areas of the 1535 (Brønsted) and 1577 cm^{-1} (Lewis) modes of pyridine adsorbed on mesoporous WO_3.

3.3.5 Product distribution and reaction pathway

Many research groups have proposed reaction pathways involving guaiacol conversion to phenol, catechol, cyclohexanol, as well as other compounds in minor quantities.

In the trickle bed reactor guaiacol, phenol and cyclohexanol were feed independently to determine the relative steady state rates and product distributions of each intermediate compound. The results of the reaction rate as a function of time for each feedstock are shown in Figure 3.8. The in-situ reduction temperature to produce WO_3 bronzes for the three reactants was 325 °C and the reactions were all carried out at 300 °C and an initial concentration of 0.232 M. The reaction reached steady state after 3 h on stream. Results in this figure show that guaiacol conversion reached 22%, phenol conversion was about 7.4% and cyclohexanol reached 99% conversion. This suggests that the relative rate of reaction was very fast for cyclohexanol compared to guaiacol and phenol was significantly slower under these conditions.

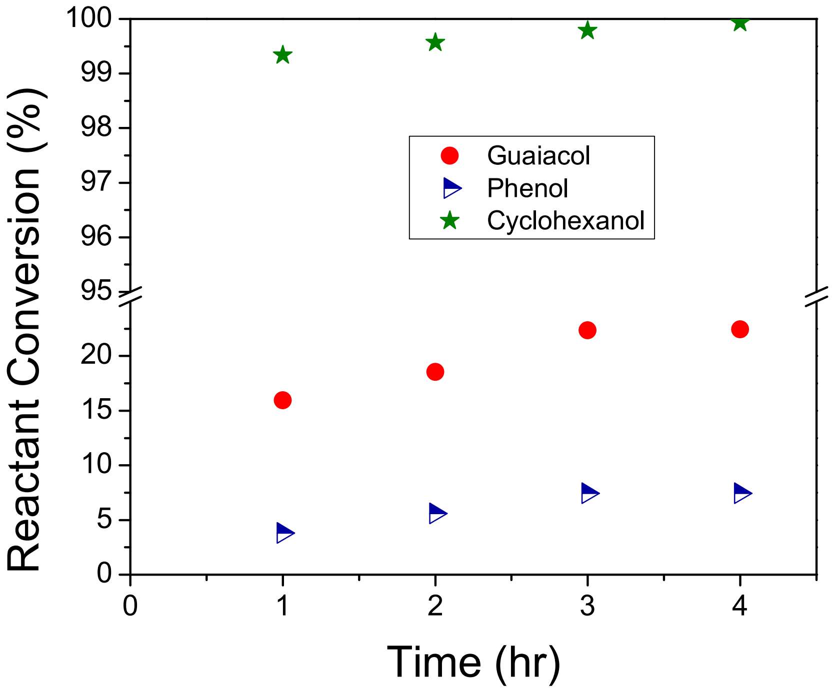

Figure 3.8 Guaiacol, phenol and cyclohexanol conversion over WO_3 bronzes.

To provide further insight to the reaction pathway, the product distribution is shown for each reactant in Figure 3.9-3.11. The reaction of guaiacol produced phenol as major compound of about 80%, followed by methanol (30%), benzene(3%) and cresols (6%).

Product selectivity's shown in the figure were calculated at time t as, $S_{i,t} = \frac{C_{product,t}}{C_{reactant,0} - C_{reactant,t}}$, where $C_{product,t}$ and $C_{reactant,t}$ are the concentrations of product and reactant at time t respectively, and $C_{reactant,0}$ is the initial concentration of reactant.

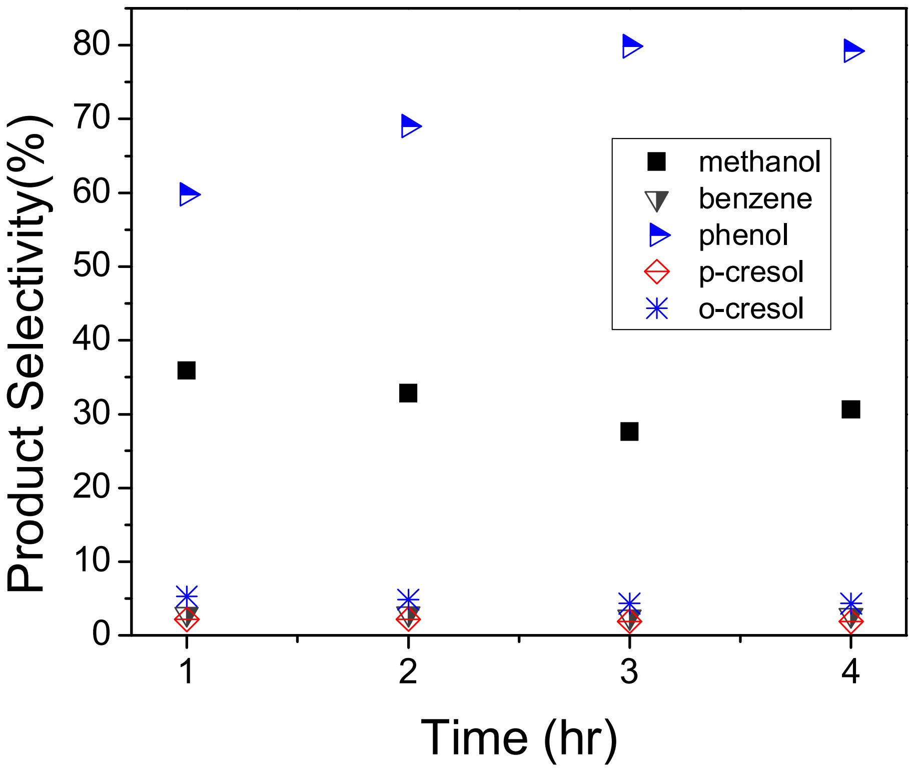

Figure 3.9 Product selectivity for reaction of guaiacol over Tungsten Oxide Bronze

The data shows that guaiacol was converted mainly to phenol (Figure 3.9) and methanol via demethoxylation (DMO). Although the amount of methanol found was less than expected compared to phenol stoichiometrically, methanol would contribute to cresol formation, which was found to be approximately 5% of the total products. Other products observed in lesser amounts were aromatics (benzene and toluene; less than 3%), and traces of aliphatic compounds (less than 1% corresponding to hexane, cyclohexene and methylcyclohexane).

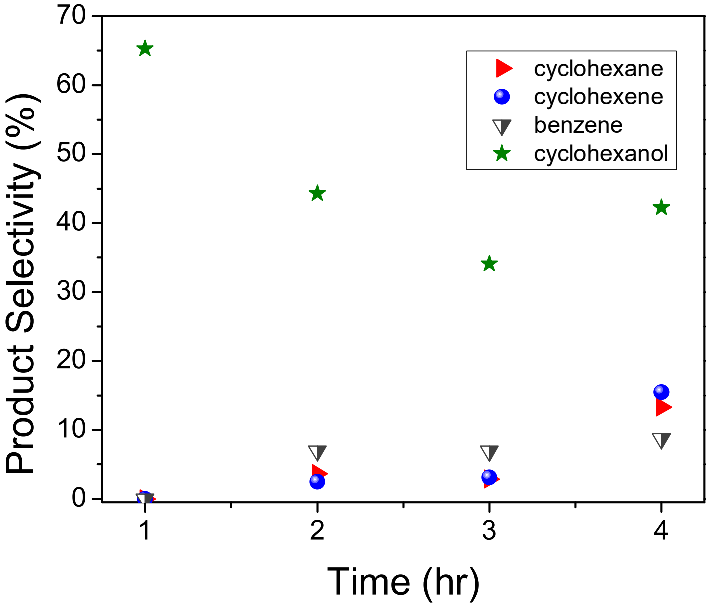

Figure 3.10 Product selectivity for reaction of phenol over Tungsten Oxide Bronze

Figure 3.10 shows that phenol was initially converted primarily to cyclohexanol and some benzene. With increasing time on stream, the amount of cyclohexanol decreased while cyclohexene and cyclohexane increased, but benzene production remained constant. Therefore, cyclohexanol and benzene are produced in a branching mechanism from phenol.

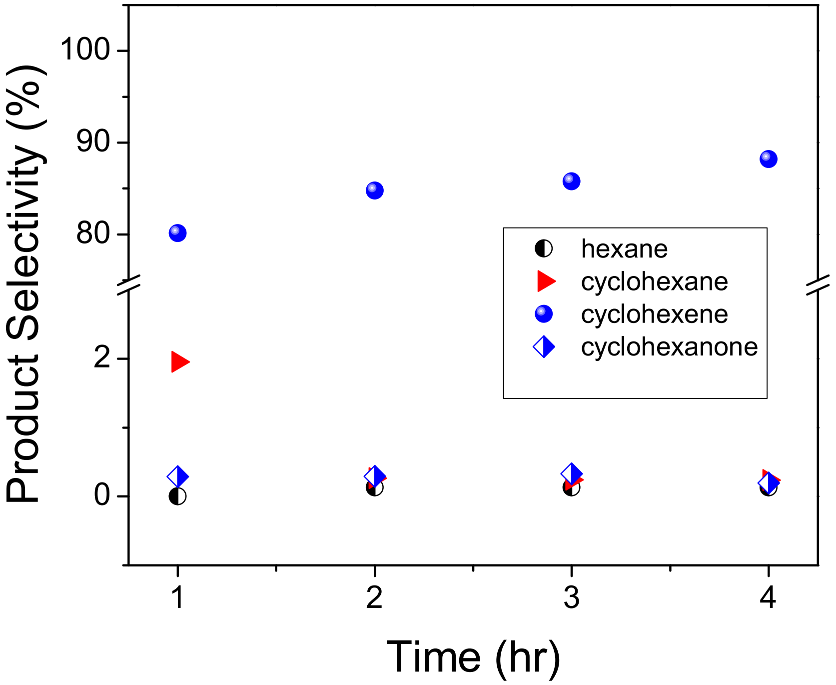

Figure 3.11. Product selectivity for reaction of cyclohexanol over Tungsten Oxide Bronze

Figure 3.11 shows that cyclohexanol reacts rapidly with high conversion (99.9 %) where cyclohexene was the major product, while less than 1% cyclohexane, hexane and cyclohexanone were produced.

From the relative rates of each reactant and product distribution shown in Figures 3.9-11, we conclude that the main pathway is as shown in Figure 3.12, where guaiacol is directly converted to phenol and methanol. Phenol can then be transformed via two parallel pathways: via aromatic ring hydrogenation to form cyclohexanone and cyclohexanol or via hydrogenolysis or direct deoxygenation (DDO) to produce benzene. The product distribution for the conversion of phenol depicted in Figure 3.10 is in agreement with most previously reported work, where phenol produced cyclohexanol as the major compound [126, 127]. Echeandia et al. [97], found high selectivity to cyclohexane when the reaction was carried out over Ni-W sulfided catalyst supported on activated carbon.

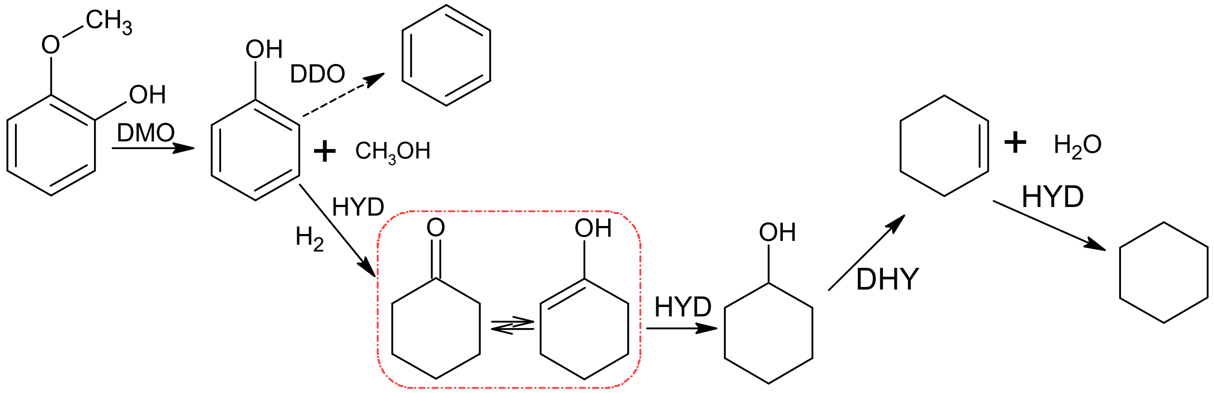

Figure 3.12 Main reaction pathway in the conversion of guaiacol over WO_3 bronze catalyst.

The high selectivity shown by WO_3 bronze catalyst to cyclohexanol, in the phenol conversion, was similar to other metal catalyst systems which follow the hydrogenation pathway. We note, however, that introduction of water dramatically changes the selectivity of the reaction and, in separate experiments, phenol reacted to produce benzene with high DDO selectivity (See Appendix.) We are aware of only a few catalysts that achieve high DDO selectivity. Olcese et al.

[86] studied gas-phase HDO of guaiacol over an Fe/SiO_2 catalyst at 400 °C and found this catalyst to be highly selective towards the production of benzene and toluene. Boullosa-Eiras et al. [35] studied the conversion of phenol over Mo_2C, MoP, Mo_2N and MoO_3 supported on TiO_2 and found high selectivity to benzene. Newman, et al.,[128] reported that highly dispersed Ru/TiO_2 was highly active and selective for conversion of phenol to benzene and suggested that the mechanism involved a bifunctional catalyst in which hydrogen spillover creates reduced titania sites that interact strongly with the hydroxyl group of phenol. Further work by Nelsen, et al.[129] proposed a mechanism, consistent with isotope labelled phenol studies, that hydrogen dissociates heterolytically to create a reactive water species that promotes C-O bond scission. Complementary studies by Crossley, et al., demonstrated that the DDO rate in gas phase cresol reactions correlated with the perimeter length of a series of Ru/TiO_2 catalysts of varying particle size.

3.3.6 Effect of H_2 pressure on the conversion of guaiacol

To gain further insight into the reaction, a set of experiments were carried out to determine the rate law. The catalyst was pre-activated at 325 ºC and the reaction temperature was 300 ºC. Figure 3.13 shows the effect of hydrogen pressure on the conversion of guaiacol as a function of time on stream. The hydrogen pressure was maintained at 3 MPa for 4 h and increased to 4 MPa for 4 h and then reduced back to 3 MPa for another 4 h.

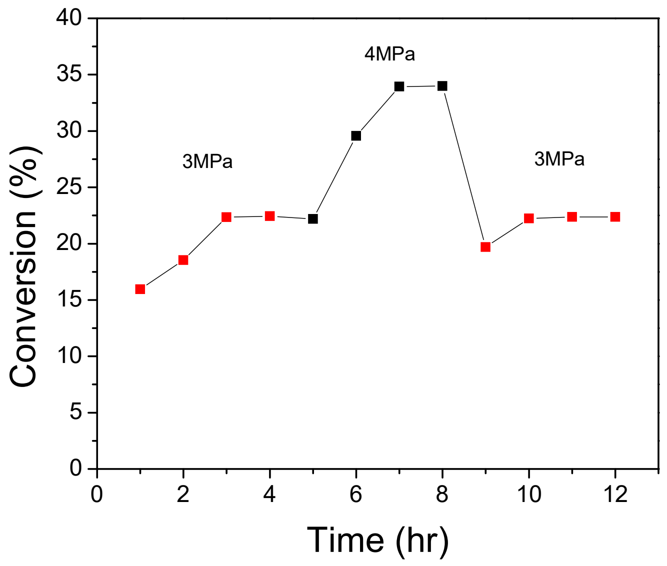

Figure 3.13 Effect of hydrogen pressure on guaiacol conversion

As shown in Figure 3.13, the guaiacol conversion increased when the H_2 pressure increased. Then, when the H_2 pressure was decreased from 4 MPa to 3 MPa the guaiacol conversion returned to the same initial value of conversion. The cycle of increase and decrease of H_2 pressure reaching the same initial value on the guaiacol conversion at 3 MPa, suggests that the catalyst is stable and has achieved steady state at 3MPa. In addition, the increase in the guaiacol conversion with increasing H_2 pressure can be attributed to an increase in solubility of hydrogen into the liquid phase, thereby increasing the surface hydrogen coverage. The distribution of the products did not change significantly with increasing hydrogen pressure (not shown), suggesting that hydrogen chemisorption on the tungsten oxide bronze catalyst doesn’t change the nature of the active sites.

3.3.7 Effect of initial guaiacol concentration

Figure 3.14 shows the effect on the guaiacol conversion as a function of the initial guaiacol concentration. The catalyst was pre-activated at 325 ºC and the reaction temperature was 300 ºC. A volumetric flow rate of 0.1 mL/min was maintained with four different guaiacol concentrations, as shown, and an additional condition was obtained for a concentration of 0.232 M and 0.03 mL/min flow rate. Conversions shown were obtained at steady state and the error bars were calculated from the standard deviation of the last three hourly samples. The figure shows that the guaiacol conversion decreases with increasing guaiacol concentration. Decreasing the flow rate from 0.1 to 0.03 mL/min also increased conversion.

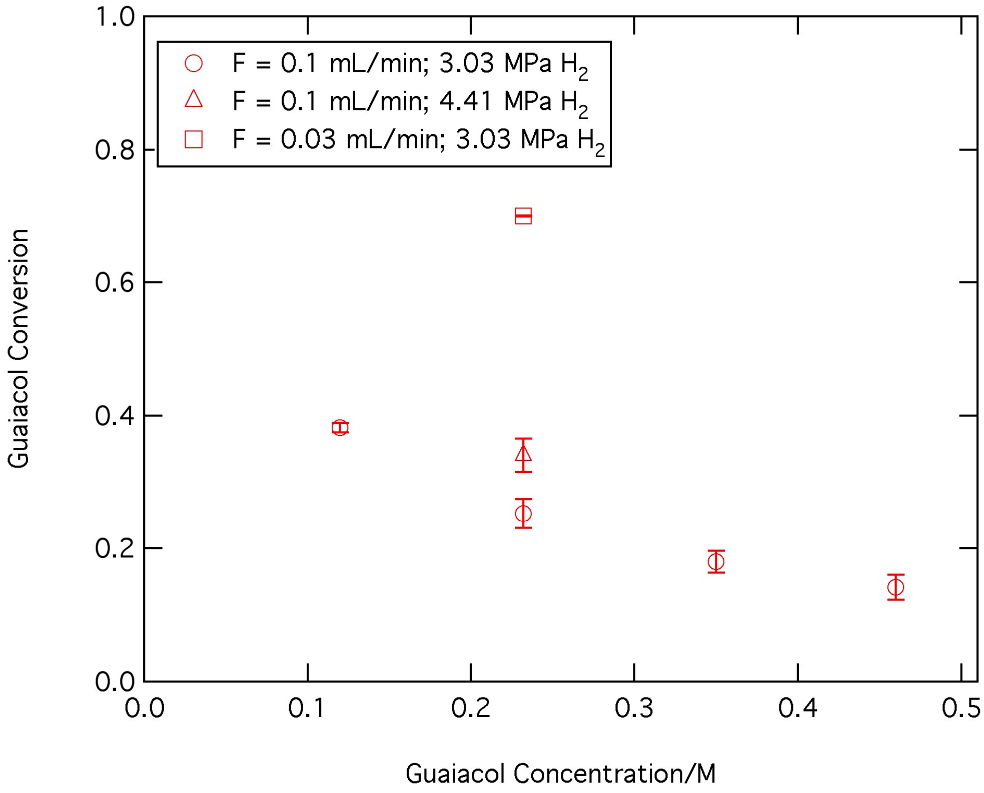

Figure 3.14 Guaiacol Conversion as a function of initial guaiacol concentration.

For a first order reaction, fractional conversion would be independent of concentration. The behavior in Figure 3.14 is generally characteristic of a 0^{th} order reaction, although a fit to a zeroth order rate law is only approximate. This decrease shown on the guaiacol conversion could attributed to a competition of active sites available on the surface of the catalyst between hydrogen and guaiacol, or other reactive intermediates that may be present. However, much is unknown about the reaction mechanism and kinetics on tungsten oxide bronze catalysts.

3.3.8 Reaction rate laws

Due to the complexity and the wide variety of compounds present in bio-oil, there is little information on the kinetics associated with the transformation processes involved. On the other hand, the conversion of guaiacol as a model compound has been widely studied and reported on different catalytic surfaces [41, 47, 130-132]. The reaction scheme in the conversion of guaiacol on a $Pt/\gamma\text{-}Al_2O_3$ catalyst was studied by Nimmanwudipong [67] et al. They also reported pseudo-first order rate constants for reactions at 573K. Bui et al. [46, 47] found first order kinetics for guaiacol conversion over CoMo catalysts. In another study based on bio-oil hydrodeoxygenation using $CoMoS/Al_2O_3$ in a batch reactor, between temperatures of 633 and 663 K, Zhang et al. [133] determined a general reaction order of 2.3 for HDO.

Evidently, despite the studies done on the conversion of guaiacol during HDO processes, there is a lack of detail in the kinetic study which would allow a better understanding of the reaction mechanism. Further kinetic studies could help understand adsorption behavior of reactants and catalytic reactions that could correspond to the Langmuir Hinshelwood-Hougen-Watson (LHHW) type [8]. Hydrogenation of furfural on Cu/SiO_2 was studied by Sitthisa et al.[134]; they reported that this reactions follow a LHHW mechanism considering the following assumptions: a) H_2 adsorbs dissociatively, b) all adsorption sites are equivalent and independent of coverage, and c) the surface reaction is the rate limiting step.

Leiva et al. [135] studied the mechanism of the conversion of guaiacol over $ReOx/SiO_2$ catalyst. The kinetic parameters obtained over $ReOx/SiO_2$ catalyst demonstrated that the reaction mechanism follows a LHHW model, where the guaiacol and hydrogen are adsorbed onto the same site of the catalyst. Also, the authors proposed 1 and 2-types of active sites for a LHHW model for the guaiacol conversion on ReOx and ReS catalysts, they found that the oxide catalyst had a better fit in a 1-site LHHW model, where guaiacol and hydrogen compete for the same site. The sulfide Re catalyst was adjusted better with a 2-site model.

Our experimental evidence, where guaiacol conversion decreases as the initial concentration increases similarly to a 0^{th} order dependence on guaiacol concentration, suggests that guaiacol competes for actives sites with hydrogen or other species that are site blocking. The increase in conversion with H_2 pressure implies that the reaction order is positive in H_2. To describe these trends more quantitatively, we considered several *LHHW* models.

Previous experimental and theoretical hydrodeoxygenation studies for acrolein and allyl alcohol can be extended to the present work and suggests that for guaiacol conversion, the active site on the tungsten oxide bronze catalyst should be oxygen vacancies, or Lewis acid sites, while surface hydroxyls, or Brønsted acid sites, may be involved in hydrogenolysis of the C-O-CH_3 bond. The increasing conversion with pretreatment temperature, which mirrors the increase in the Brønsted/Lewis acid ratio as determined from pyridine adsorption, provides further support for Brønsted sites contributing to the rate limiting step.

3.3.8.1 Langmuir Hinshelwood Models

We begin with the simplest model, assuming the presence of **one type** of active site (*) for both hydrogen and guaiacol adsorption, and then consider two-site models to determine if there is a significant improvement, given the range of data available. We expect Lewis acidic surface oxygen vacancy sites to be the active site for oxygenate adsorption, based on previous theoretical studies,[136, 137]] and also the site where hydrogen dissociation and formation of the bronze occurs based on experimental and theoretical evidence.[125, 136, 137]] After dissociation, hydrogens are very mobile and likely occupy hydroxyl positions in the bulk as well as at the surface. Therefore, a one-site model is physically reasonable. Hydrogen dissociation occurs homolytically on the surface. The elementary steps and associated quasi-equilibria for steps prior to the irreversible rate-controlling step (rcs) are as follows:

$$H_2 + \ 2* \overset{K_{H_2}}{\Longleftrightarrow} 2\,H* \qquad \text{Equilibrium} \quad [H*] = K_{H_2}{}^{1/2} P_{H_2}{}^{1/2} [*] \tag{3.2}$$

$$GUA + * \overset{K_{GUA}}{\Longleftrightarrow} GUA * \qquad \text{Equilibrium} \quad [GUA *] = K_{GUA}[GUA][*] \tag{3.3}$$

$$GUA * + 2H * \xrightarrow{k_3} PHE + MeOH + 3 * \qquad \text{rcs} \tag{3.4}$$

Site Balance

$$C_T = [H *] + [GUA *] + [*] \tag{3.5}$$

Substituting equations 3.2 and 3.3 in 3.5 gives:

$$C_T = [*] + K_{GUA}[GUA][*] + \sqrt{K_{H_2}P_{H_2}}\,[*] \tag{3.6}$$

$$C_T = [*]\left\{1 + K_{GUA}[GUA] + \sqrt{K_{H_2}P_{H_2}}\,\right\} \tag{3.7}$$

From equation 3.4:

$$r_3 = k_3 K_{GUA}[GUA]K_{H_2}P_{H_2}[*]^3 \tag{3.8}$$

Substituting equation 3.7 in 3.8:

$$r_3 = \frac{k_3 K_{GUA}[GUA]K_{H_2}P_{H_2}{C_T}^3}{\left\{1+K_{GUA}[GUA]+\sqrt{K_{H_2}P_{H_2}}\,\right\}^3}, \tag{3.9}$$

$$k_{eff} = k_3 {C_T}^3 \tag{3.10}$$

Models 2 and 3 are shown in appendix B-1 and B-2

Each rate law was evaluated by solving the material balance for plug-flow reactor for extent of reaction, ξ,

$$\frac{d}{dw}\xi(w) = -r_G\left(\frac{C_{G0}F_{in}-\xi(w)}{F_{in}}, P_{H_2}, k_{eff}, K_G, K_{H_2}\right), \tag{3.11}$$

where w is the catalyst weight (1 g), C_{G0} is the initial guaiacol concentration, F_{in} is the molar flow rate at the inlet, P_{H_2} is the hydrogen pressure, and the initial condition was $\xi(0) = 0$. The fitting parameters for each model (e.g. k_{eff}, K_G, K_{H_2}) were adjusted to obtain the best fit to the experimental data (4 data points for guaiacol initial concentration at 0.1 mL/min and 3 MPa H_2 pressure, one measurement at 3 MPa H_2 pressure, and one for 0.03 mL/min guaiacol flow rate). In Mathcad (vers. 15). two types of differential equation solvers (Adams/BDF and Radau) were used with each rate law. From the resulting fit, we calculated the reduced Chi Squared using the standard deviation of the data points from the guaiacol conversion at steady state. To decide which model fits our experimental data points better, the corrected Akaike criterion was used[138, 139], which takes into account the number of data points (n=6) and the number of fitting parameters (k=2-4). The best data fits and statistical information are described in detail in Tables 3.3 and 3.4.

The fit to LHHW Model 1 is shown in Figure 3.15. Although the rate law captures the general behavior quite well, the mechanism involves a ternary rate controlling step, which is generally of low probability, although a concerted 2-proton transfer process has been suggested in glucose conversion reactions [140] The model requires fitting 3 parameters, and with only 6 data points, leads to a relatively large corrected Akaike information criterion (cAIC). Therefore, two additional Langmuir-Hinshelwood rate laws were derived, distinguishing between the first and second proton transfer to the C-O bond.

The elementary steps considered were:

1. $G + * \rightleftharpoons G*$

2. $H_2 + 2* \rightleftharpoons 2H*$

3. $G* + H* \rightleftharpoons GH* + *$

4. $GH* + H* \rightleftharpoons GH_2* + *$

5. $GH_2* \rightleftharpoons CH_3OH + P*$

6. $P* \rightleftharpoons P + *$

The rate laws, reduced Chi Squared values, and the cAIC values for the three Langmuir-Hinshelwood models considered are provided in Table 3.3. Comparison of Model 1 and Model 2 shows that a better fit is obtained for 1st order dependence on H_2 than ½ order, suggesting that the rate controlling step is after the transfer of the second proton.

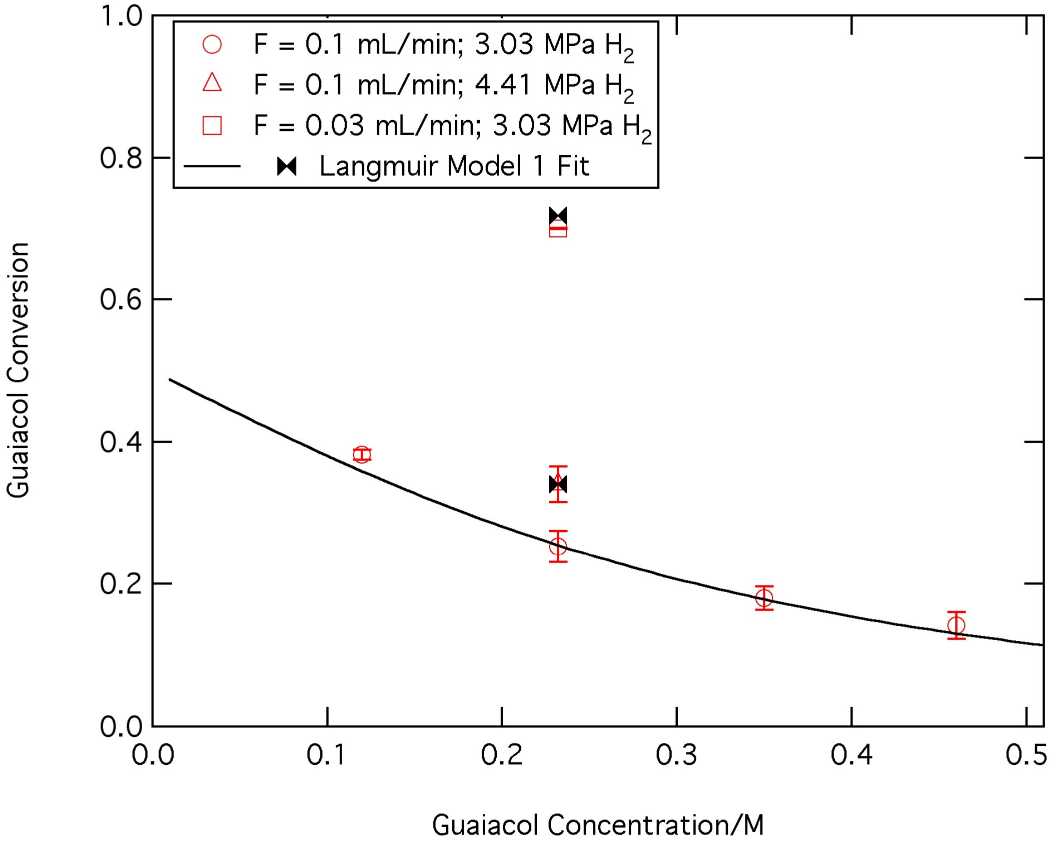

Figure 3.15. Langmuir-Hinshelwood Model 1 fit to guaiacol conversion data.

3.3.8.2 LH models with most abundant surface intermediates (MASI)

To simplify some of the LHHW models and considering that some species may block sites that stop guaiacol from adsorbing onto the surface, we also derived rate laws with a most abundant surface intermediate (MASI),[141] which is the species considered to be in highest amount on the surface, which in our case could be guaiacol or phenol. The models were designated as Case 1-3, corresponding to a rate controlling step 3-5, with adsorbed guaiacol (G*) as MASI. In addition, variants where the MASI corresponded to the intermediates GH*, GH_2*, and P* were designated as A, B, and C, resulting in 12 different cases. In addition, a model with step 5 (C-O bond cleavage) with both G* and P* as MASI was derived, designated as Case 6. A selection of the final rate laws is summarized below in Table 3.4, along with the statistical fitting information.

Of all the two parameter models tested, the variants of Case 2 fit our experimental data similarly and generally better than the Case 1 variants. In Case 2, we considered guaiacol as the most abundant surface intermediate (MASI), with the rate controlling step the addition of the second hydrogen. The fitted data is shown in figure 3.16. This rate law is first order in hydrogen and 1st order in guaiacol, but the dependence on guaiacol concentration in the denominator leads to zeroth order dependence at high coverage. Comparison of the fit of Case 1, which is mathematically identical except for ½ order dependence on H_2 pressure, illustrates the general inability of all the Case 1 variants to account for the increase in conversion with higher H_2 pressure.

Table 3.3 Summary of Langmuir Hinshelwood Rate Laws

Model	RCS	Rate Law	Chi Sq	cAIC
1	Addition of 2 H Trimolecular rxn	$r_3 = \frac{k_3 K_{GUA}[GUA] K_{H_2} P_{H_2} {C_T}^3}{\left\{1 + K_{GUA}[GUA] + \sqrt{K_{H_2} P_{H_2}}\right\}^3}$	156.7	59
2	Addition of 1st H	$r_3 = \frac{k_3 K_{GUA} C_T^2 [GUA] \sqrt{K_{H_2} P_{H_2}}}{\left\{1 + K_{GUA}[GUA] + \sqrt{K_{H_2} P_{H_2}}\right\}^2}$	312	65
3	Addition of 2nd H	$r_4 = \frac{k_4 K_3 K_{GUA}[GUA] K_{H_2} P_{H_2} [C_T]^2}{\left\{1 + {K_{H_2}}^{1/2} {P_{H_2}}^{1/2} + K_{GUA}[GUA] + K_3 K_{GUA}[GUA] {K_{H_2}}^{1/2} {P_{H_2}}^{1/2}\right\}^2}$	143	88

Table 3.4 Langmuir Hinshelwood Rate Laws considering MASI

Case	RCS	MASI	Rate Law	Chi Sq	cAIC
1	#3	G*	$r = \frac{k_3 K_1 K_2^{1/2} C_G P_{H_2}^{1/2}}{\left(1+K_1 C_G\right)^2} = \frac{k_{app} C_G P_{H_2}^{1/2}}{\left(1+K_{app} C_G\right)^2}$	170	50
2	#4	G*	$r = \frac{k_3 K_1 K_2 C_G P_{H_2}}{\left(1+K_1 C_G\right)^2} = \frac{k_{app} C_G P_{H_2}}{\left(1+K_{app} C_G\right)^2}$	80	45
4	#5	G*	$r = \frac{k_3 K_1 K_2 C_G P_{H_2}}{\left(1+K_1 C_G\right)} = \frac{k_{app} C_G P_{H_2}}{\left(1+K_{app} C_G\right)}$	76	45
5	#5	P*	$r = \frac{k_3 K_1 K_2 C_G P_{H_2}}{\left(1+K_6^{-1} C_P\right)} = \frac{k_{app} C_G P_{H_2}}{\left(1+K_{app} C_P\right)}$	60	43
6	#5	P* & G	$r = \frac{k_3 K_1 K_2 C_G P_{H_2}}{\left(1+K_6^{-1} C_P + K_1 C_G\right)} = \frac{k_{app} C_G P_{H_2}}{\left(1+K_{app} C_P + K_{app2} C_G\right)}$	0.56	25

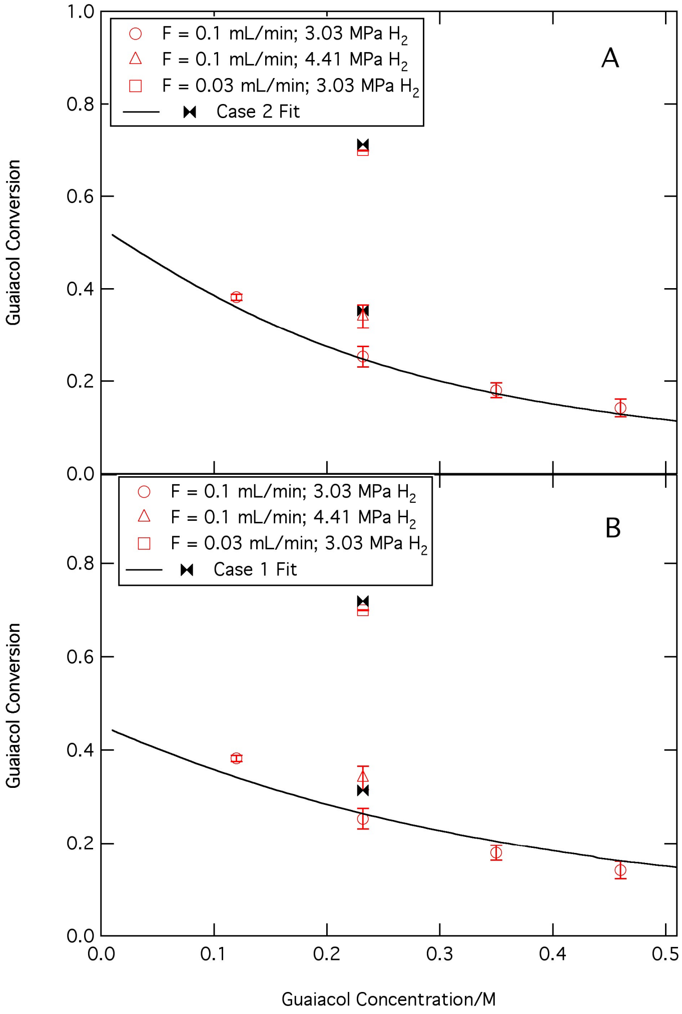

Figure 3.16. Comparison of Case 2 (rcs = 2nd H transfer; MASI = G*) with Case 1 (rcs = 1st H transfer; MASI = G*) illustrating the sensitivity of the rate law to H_2 pressure.

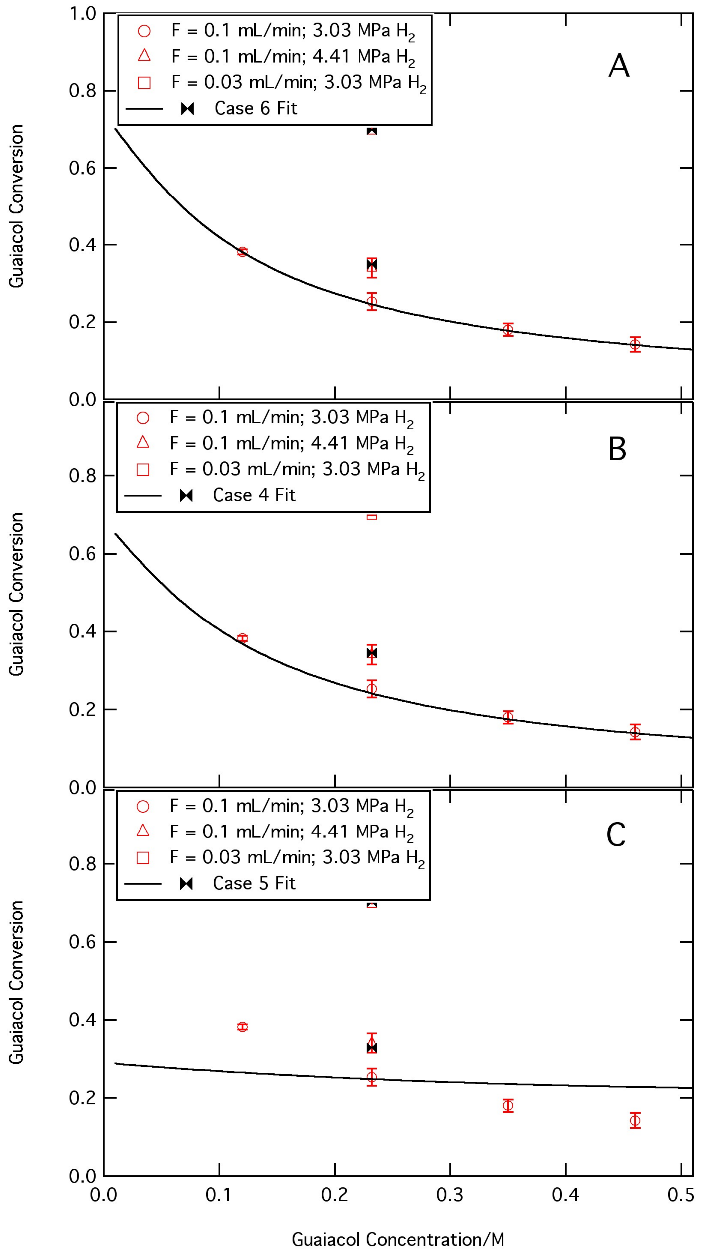

Figure 3.17. Comparison of models in which the C-O bond cleavage is the RCS and the MASI is P* (Case 5), G* (Case 4), and both G* and P* (Case 6), suggesting that guaiacol is the predominant surface intermediate, although there may be some phenol.

Of the 3-parameter fits, Case 6 has the lowest Chi Squared. Figure 3.17 compares Cases 4, 5 and 6, which involve the same RCS of breaking of the C-O bond, but different MASI; G*, P* and (P* & G*) respectively. Case 5 considers phenol as the most abundant on the surface, which does not produce the curvature observed in the guaiacol concentration dependence. As given in Table 3.4, Case 6 has the best fittings of all data points, Case 4 is nearly as good, but Case 5 has the poorest fit, suggesting that the surface is predominantly covered with guaiacol, although some phenol may also be present. The relative rates of conversion of guaiacol and phenol would suggest that phenol may cover the surface, although phenol was the major product in the guaiacol product distribution.

3.3.8.3 Two-site models

We also developed a two site LHHW Model based on Case 2, which gave the rate law,

$$r = \frac{k_{app}[C_G\,]P_{H_2}}{(1+K_{app1}\,[C_G\,])((1+\sqrt{K_{app2}P_{H_2}})}. \tag{11}$$

After testing with Mathcad, we found a poorer fit as described by the Reduced Chi Square as well as by the corrected Akaike information criterion (AICc = 56 for the 2-site Case 2 compared to AICc = 43 for Case 2) when an extra parameter is considered.

In summary, the best rate laws are first order in hydrogen and guaiacol as MASI. When comparing Case 1 and Case 2 both considered guaiacol as the MASI, but with a different rate controlling step. The RCS of Case 6, involving C-O bond cleavage, not only better accounts for the increase in conversion when the hydrogen pressure increased, but also is consistent with the aromatic C-O bond being relatively strong.

3.3.9 Activation energy

The effects of reaction temperature and activation temperature on conversion, shown in Figure 3.18, provide information about the activation energy of the rate controlling step as well as the relative increase in active sites with higher activation temperature. The conversion for each reaction temperature was converted into a rate constant using a 0^{th} order reactor model and an Arhenius plot was constructed to obtain a direct analysis of the activation energy. We obtained a value of 71 kJ/mol for the apparent activation energy. For comparison, assuming a first order reactor model gave a value of Ea = 93 kJ/mol. Based on the rate law for Case 6, in which the fitting parameter, $k_{app} = k_3K_1C_T$, we estimated the activation energy assuming that the temperature dependence of k_3 is large compared to the equilibrium constant, K_1, for adsorption of guaiacol. Figure 3.18 shows a plot of the log of $k_{app}(T)/k_{1pp}(300)$ vs. 1/T. The slope of the Arrhenius plot gives a value of Ea = 89 kJ/mol.

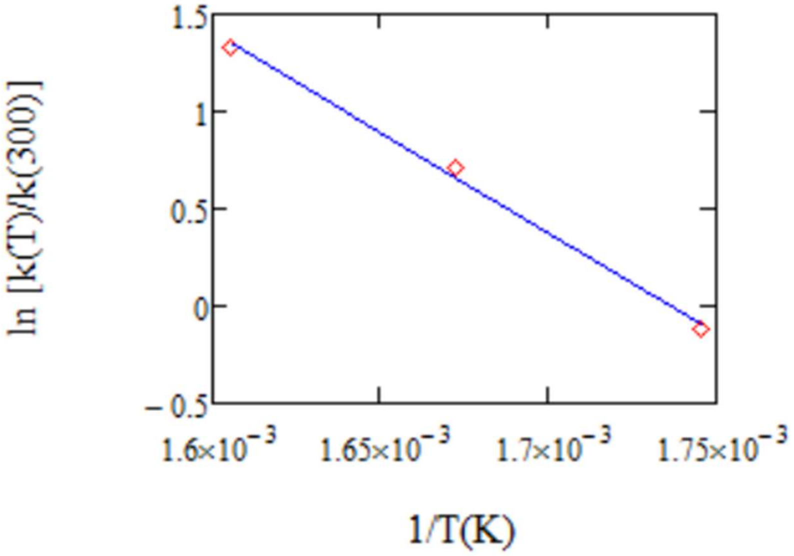

Figure 3.18. Plot of the log of $k_{app}(T)/k_{1pp}(300)$ vs. 1/T for reactions at 300, 325, and 350 °C after activation at 325 °C; where the rate law of Case 6 was used to extract k_{app} from the conversion data of Figure 3.5. Estimated activation energy is 89 kJ/mol.

3.3.10 Acid site density

In a similar process, we compared the relative values of k_{app} at a reaction temperature of 300 °C for each activation temperature, as shown in Figure 3.19. The dependence of k_{app} on the site density, C_T, provides a qualitative indication of the increase in sites as the bronze was formed at increasing temperatures.

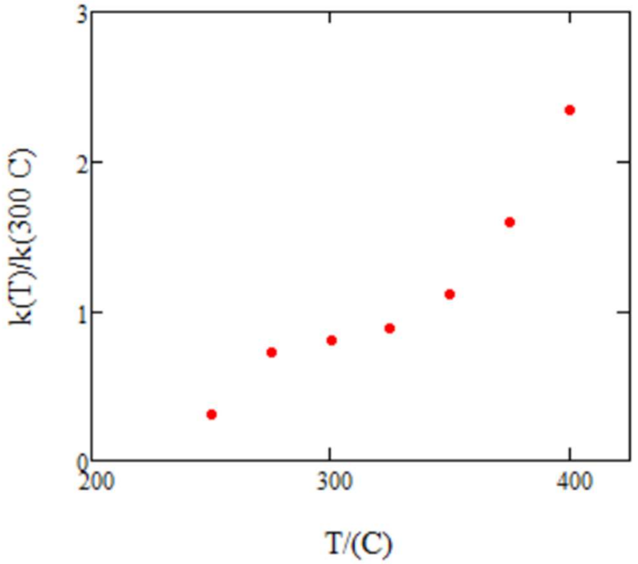

Figure 3.19. Plot of k_{app} $(T_{act})/k_{1pp}$ (325) vs. activation Temperature for reactions at 300°C; where the rate law of Case 6 was used to extract k_{app} from the conversion data of Figure 3.5.

The thermogravimetric analysis by Thibodeau, et al.[124] shows that the sub-stoichiometry increases with activation temperature, suggesting that the surface oxygen vacancy coverage also increases with activation temperature. However, the pyridine probe molecule studies by Mahdavi-Shakib of the Brønsted to Lewis acid site ratio also increase with activation temperature, as shown in Figure 3.7. A more detailed microkinetic model would be required to assess the extent to which the hydrogen transfer (steps 3 and 4) vs. C-O bond cleavage is rate controlling.

3.4 Conclusions

We have shown that the reaction pathway for guaiacol on reduced tungsten oxide bronze catalysts under liquid phase, water-free conditions, proceeds via demethoxylation to phenol, followed by hydrogenation to cyclohexanol, and dehydration to cyclohexene. LHHW mechanisms have been applied to model the liquid phase HDO of guaiacol on unsupported WO_3 bronzes. Good agreement was found for rate laws based on a rate controlling step in which the C-O bond cleavage occurs at a Lewis acidic surface oxygen vacancy site. The increase in conversion correlates with both the greater reduction (z) of the tungsten oxide bronze, H_xWO_{3-z}, and the increasing Brønsted/Lewis acid site density observed by pyridine adsorption as the temperature of hydrogen activation increases. The zeroth order behavior is accounted for within the LHHW model by site-blocking, predominantly by guaiacol, but probably to some extent also phenol.

CHAPTER 4

EFFECT OF SUPPORT AND METAL CONTENT ON Ni CATALYSTS FOR THE CONVERSION OF 2-METHOXYPHENOL

4.1 Introduction

This chapter presents reactivity and selectivity in a series of catalysts prepared for the study of the conversion of 2-methoxyphenol, commonly known as guaiacol, as a model compound. The active phase studied was nickel prepared with approximately the same metal content on three different supports (Al_2O_3, SiO_2 and SiO_2-Al_2O_3), chosen due to their marked differences in acidity. The most active catalyst was chosen for additional studies using the same model compound to investigate the effect of Ni metal content using Al_2O_3 as support. All catalysts were activated ex-situ at 500 °C for 4 h and tested in a batch reactor at 300 °C and 3 MPa.

The effects of metal-support interaction, acidity and particle size were related to the catalytic activities observed. The initial reaction rate, corresponding to the demethoxylation of guiacol, was highest on Ni/ Al_2O_3 which had the highest nickel dispersion. The selectivity for deoxygenation, at constant conversion, was used as a measure of the relative rate of dehydration to hydrogenation, at constant metal loading and conversion. The deoxygenation selectivity was highest on the Ni/ SiO_2-Al_2O_3 catalyst which also had the highest acidity.

4.2 Experimental Methods

4.2.1 Reactants and catalyst precursors

Table 4.1 lists the materials used in the preparation of nickel supported catalysts and reactants used in the hydrodeoxygenation (HDO) reactions of guaiacol in the batch reactor, described below in Section 4.2.5.

Table 4.1 Reactants and catalyst precursors

Name	**Formula**	**Manufacturer**
Nickel nitrate hexahydrate	$Ni(NO_3)_2 \cdot 6\ H_2O$	Sigma Aldrich, ≥99.99
2- Methoxyphenol	$C_6H_4(OH)(OCH_3)$	Acros, 99.9%
Dodecane	$CH_3(CH_2)_{10}CH_3$	Fisher, 99%
Hexadecane	$C_{16}H_{34}$	Sigma Aldrich, 99%
Hydrogen	H_2	Ultra-high purity, Matheson Gas
Gamma Alumina	γ-Al_2O_3	Alfa Aesar
Silica	SiO_2	Grace, Co., DAVICAT SI 1101
Silica-Alumina	SiO_2-Al_2O_3	Grace, Co., DAVICAT SIAL 3115

4.2.2 Preparation of Ni-supported catalysts

Ni-supported catalysts were prepared using three commercial supports: γ-Al_2O_3, SiO_2 and SiO_2-Al_2O_3 as shown in Table 4.2. The supports were ground and sieved to obtain an 80-125 μm particle size. The catalysts were prepared by incipient wetness impregnation using an aqueous solution of nickel nitrate hexahydrate ($Ni(NO_3)_2*6H_2O$). The resulting mixture was mixed with a spatula until the formation of a homogeneous paste. Then the samples were left covered for 24 h at room temperature, then dried overnight for 12 h at 100 °C. The dried materials were then calcined at 450 °C for 4 hours to thermally decompose the precursor and form nickel oxide on the support. The catalysts prepared had a theoretical amount of 10% nickel on each support. Additionally, catalysts with varying Ni loadings were prepared using γ-Al_2O_3 as supporting material.

4.2.3 Chemical analysis

Identification and quantification of atomic species present in catalyst materials is essential; elemental analysis is used to determine the amounts of elements present in a determined sample. The element of interest is volatilized and atomized by application of high heat, using an argon plasma source that excites the atoms and ions to an electronically excited state, which then emits light. For this thesis, inductively coupled plasma optical emission ICP OES was used.

The Ni content analysis in the calcined catalysts was determined in-house (at Bates College, courtesy of Prof. Rachel Austin and Ben Ghoundie) using a Thermo Scientific iCAP 600 ICP-OES spectrometer with microwave-assisted digestion. Microwave digestion was performed using a CEM MARS 6 microwave and CEM EasyPrep digestion vessels. Approximately 25 mg of catalyst was placed in each vessel with 8 mL of $1HNO_3$:3HCl and allowed to sit for 12 h. The temperature was then ramped to 513 K over 25 min, and held for 30 min. The pressure was not allowed to exceed 350 psi. After cooling the digested materials were diluted to a total volume of 50 mL in EPure water and filtered before ICP-OES analysis.

4.2.4 Activation of Nickel-supported catalysts

All nickel catalysts used in this thesis were activated ex-situ in a 10 mm i.d. × 12 mm o.d. × 1 m long quartz reactor fitted with a quartz wool plug. The reactor tube was placed inside a tube furnace (Mellen). The temperature was monitored using a K-type thermocouple which was controlled by a programmable temperature controller (Omega Series CN- 4321) connected to the furnace. High purity gases were connected to the reactor via stainless steel tubing. The gas flow rates were controlled using needle valves and measured with a soap bubble flow meter. For a typical synthesis, the reactor tube was loaded with 100 mg of powder and then purged with nitrogen gas for 15 min to remove air, before switching to a pure hydrogen flow at a rate of 100 mL min^{-1}, used to reduce the catalysts. Once hydrogen started to flow through the bed the temperature was increased at 5 °C min^{-1} up to 450 °C and maintained for 4 hours. After the 4 hours were completed, the system was cooled down to room temperature while maintaining hydrogen flow. Once ambient temperature was reached, the catalyst was quickly removed and weighed for loading into the batch reactor.

4.2.5 Determination of catalytic activity of guaiacol in the batch reactor

All experiments were carried out in a 300 mL stainless steel batch autoclave (Parr, Series 450 Mini Bench Top Reactor) operated at 300 °C and under a H_2 pressure of 5 MPa. A schematic of the reaction set-up is shown in Figure 4.1.

The reactor (Parr, Model 4875) had a gas entrainment stirrer that ensures the homogeneity of hydrogen throughout the reactor. A stirring rate of 700 rpm was necessary to ensure the proper mixing of the catalyst with the model compound solution and hydrogen present. A heating mantle and temperature control system was used to regulate the heating and cooling temperature of the system for each experimental run. A thermocouple placed inside a thermowell was used to measure the temperature inside the reactor.

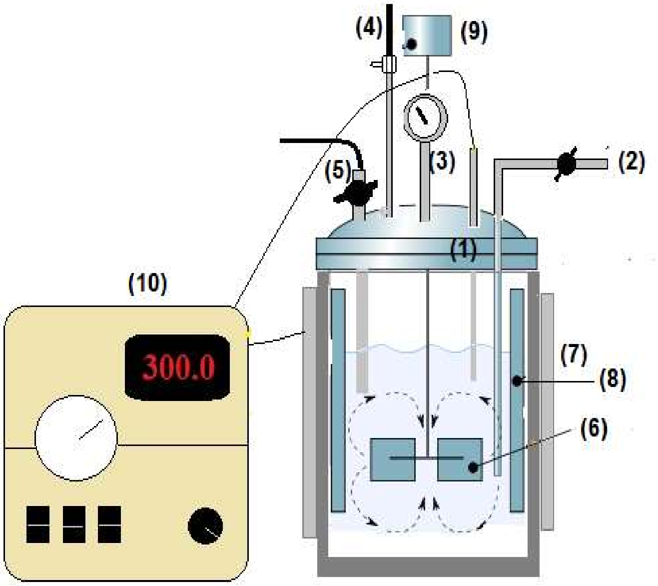

Figure 4.1 Schematic drawing of the batch reactor: (1) thermowell, (2) gas outlet, (3) high pressure regulator, (4) purge, (5) sample withdrawal dip tube, (6) magnetically coupled stirrer, (7) heating mantle, (8) baffles, (9) motor, and (10) temperature controller (Figure, courtesy of Dr. Catherine Sepulveda, Chile).

About 50 mg of freshly pretreated catalyst was used for each experiment. The reactor was charged with 80 mL of dodecane solution containing guaiacol (0.232 mol L^{-1}) and hexadecane as internal standard for GC analysis. The sealed reactor was flushed with hydrogen to evacuate air from the system by pressurization-depressurization cycles. While continuously stirring the mixture, the reactor was heated to 300 °C under approximately 1 atmosphere of H_2. Once the reaction temperature was attained, the H_2 pressure was pressurized to 5 MPa. This pressure was maintained for the entire duration of the experiment by adding H_2 to the reactor whenever necessary. Samples were periodically withdrawn from the reactor through a $\frac{1}{16}$-in diameter tube (incorporated with a stainless-steel filter inside the reactor) after the sampling line has been purged with small amounts of the reactant mixture. The liquid samples were collected and sealed in septum vials and analyzed using the same method described in section 3.2.6. The concentration of guaiacol at the start of the reaction, from a sample after heating and pressurizing with H_2, was taken as 100% in order to exclude small amounts of conversion during heating of the system.

The catalytic activity for guaiacol conversion was determined by the initial reaction rate which was calculated from the slopes of the conversion vs. reaction time plot, according to the following equation:

$$r_s = \frac{[b \times n]}{m} \tag{4.1}$$

where r_s is the initial reaction rate, expressed in mol g^{-1} min^{-1}, where *b* represents the slope of the initial conversion of the guaiacol, *n* is the initial number of moles of the compound and *m* is the mass of catalyst used(mg)[40]

Percent selectivities, S%, were determined at 10 % conversion of guaiacol to exclude contributions from internal and external mass transfers,

$$S\% = \frac{M_i(\frac{g}{L})}{M_T(\frac{g}{L})} * 100 \qquad (4.2)$$

where M_i is the amount of compound *i* in mol/L and M_T is the total amount of compounds produced in grams per liter in the conversion of guaiacol.

4.2.6 Nitrogen adsorption isotherm

The nitrogen adsorption technique was described previously in section 2.1. Nitrogen adsorption/desorption isotherms for all Ni-supported catalysts were measured at 77 K using using a Micromeritics-TriStar II 3020 (Courtesy Prof. Nestor Escalona, University of Concepcion) shown in Figure 2.4 to determine the BET specific surface area (S_{BET}) and total pore volume (Vp) of supports and nickel catalysts. Prior to the analysis, the samples were degassed at 300 °C for 2 h.

Figure 4.2 Micromeritics TRISTAR II 3020 used for determination of specific surface areas.

4.2.7 X-Ray Diffraction (XRD)

X-ray diffraction has been previously described in section 2.2 and was also used for all Ni-supported catalysts. X-ray diffraction (XRD) patterns of the samples were obtained using a Rigaku diffractometer (Courtesy Prof. Nestor Escalona, University of Concepcion) equipped with Ni-filtered Cu $K_{\alpha1}$ radiation (λ =1.5418 Å). The standard scan parameters were 10–90° 2θ with a step size of 0.02° and a counting time of 0.4 s per step. Identification of the phases was achieved by reference to the ICDD files using EVA analysis software.

4.2.8 Temperature programmed reduction (TPR)

TPR allows the determination of the reducibility of supported catalysts and reveals the temperature at which the reduction process occurs.

The analysis begins by flowing a gas, typically a diluted hydrogen/argon mixture. While gas flows through the sample, the temperature increases linearly with time. The experiments were carried out in a quartz cell on a conventional system equipped with a thermal conductivity detector.

Each catalyst was analyzed by performing a sequence of pretreatment, TPR and CO chemisorption steps, in which approximately 50 mg of the sample was pretreated by heating to (100 °C at 10 °C/min) under Ar with a flow of 40 sccm, and holding at 100 °C for 60 min. After cooling to 30 °C, at the beginning of the TPR experiment, the gas mixture was replaced with a 10% H_2/Ar mixture, the sample was heated at a rate of 10°C min^{-1} from 30 to 550 °C. After the completion of the TPR step, the sample was cooled to room temperature with a ramp rate of 10 °C/min in argon and held for 10min.

4.2.9 Chemisorption

The IUPAC defines chemisorption as an adsorption that results from strong interaction between the adsorbent and the adsorbate in a monolayer on a surface [110]. Unlike physisorption, chemisorption results from chemical bond formation between the probe gas (CO, H_2, or O_2) and localized, or specific, surface sites. This technique provides a measure of the number of surface metal atoms from measurement of the amount of chemisorptive gas adsorbed on the surface. The information about the active surface allows one to evaluate catalyst materials in the design and production phases. The quantity of chemisorbed gas can be determined using the static volumetric method or the dynamic flow method after catalyst pretreatment that includes cleaning and/or reduction to prepare the surface for exposure to reactive gas. The static volumetric technique measures the volume of chemisorbed gas as a function of gas pressure at constant sample temperature. The isotherm generated is used to determine the monolayer capacity of a catalyst sample. The dynamic flow method involves injecting precise pulses of chemisorbing gas into a flowing inert gas stream over the catalyst. A thermal conductivity detector (TCD) is used to quantitatively monitor changes in gas composition exiting the sample cell.

CO chemisorption measurements were performed using a Micromeritics ASAP 2020 apparatus, from which the metal dispersion was estimated. The catalysts were reduced in situ with flowing H_2 using the same conditions prior to catalytic tests, evacuated with flowing He and cooled down to 303 K. Then CO chemisorption was measured at 303K and 0.003-0.07 MPa, Ni dispersion was calculated assuming an average CO:Ni stoichiometry of 1:1.

4.3 Results

4.3.1 Effect of support: characterization of supports and catalysts

4.3.1.1 Chemical analysis ICP

Elemental analysis was done for all Ni/support catalysts to determine the amount of metallic nickel. All the catalysts used in this chapter are presented in Table 4.2.

Table 4.2. Nominal and actual nickel loadings of catalysts.

Theoretical Ni/Support	Real Ni content(%)	Thesis Notation
6%Ni/Al_2O_3	5.3	Ni(5)/ Al_2O_3
8%Ni/ Al_2O_3	6.1	Ni(6)/ Al_2O_3
10%Ni/ Al_2O_3	8.5	Ni(8)/ Al_2O_3
12%Ni/ Al_2O_3	10.1	Ni(10)/ Al_2O_3
15%Ni/ Al_2O_3	13.2	Ni(13)/ Al_2O_3
20%Ni/ Al_2O_3	17.4	Ni(17)/ Al_2O_3
10%Ni/SiO_2	10.6	Ni(10)/ SiO_2
10%Ni/ SiO_2- Al_2O_3	10.1	Ni(10)/ SiO_2- Al_2O_3

4.3.1.2 CO chemisorption

Table 4.3 gives the CO uptake at STP (273 K, 1 atm), the number of surface Ni atoms per gram catalyst, the percent dispersion, *D*, based on the total amount of Ni atoms impregnated per gram catalyst, the surface area of Ni particles per gram catalyst, and the particle size assuming a cubic and a hemispherical shape. The particle sizes generally increase with loading and are significantly larger on the SiO_2 and SiO_2-Al_2O_3 supports.

Table 4.3. CO chemisorption data for nickel catalysts.

%Ni	Monolayer capacity (ccSTP/g)	Ni atoms on surface	D	Impregnated Ni (atoms/gcat)	S_{met} (m^2Ni/gcat)	Spheres (nm)
Ni-Al_2O_3						
5.3	0.5652	1.52E+19	2.80%	5.44E+20	0.817	14.6
5.3	0.5669	1.52E+19	2.80%	5.44E+20	0.818	14.6
5.3	0.5701	1.53E+19	2.82%	5.44E+20	0.822	14.5
6.1	0.6439	1.73E+19	2.77%	6.26E+20	0.929	14.7
6.1	0.6324	1.70E+19	2.72%	6.26E+20	0.912	15.0
6.1	0.6295	1.69E+19	2.70%	6.26E+20	0.908	15.1
8.5	0.8519	2.29E+19	2.63%	8.72E+20	1.229	15.5
8.5	0.8401	2.26E+19	2.59%	8.72E+20	1.212	15.7
8.5	0.8491	2.28E+19	2.62%	8.72E+20	1.225	15.6
10.1	0.9507	2.56E+19	2.47%	1.04E+21	1.371	16.5
10.1	0.9496	2.55E+19	2.46%	1.04E+21	1.370	16.6
10.1	0.9543	2.57E+19	2.48%	1.04E+21	1.377	16.5
13.2	0.9135	2.46E+19	1.81%	1.35E+21	1.318	22.5
13.2	0.9115	2.45E+19	1.81%	1.35E+21	1.315	22.5
13.2	0.9095	2.45E+19	1.81%	1.35E+21	1.312	22.6
17	0.9418	2.53E+19	1.45%	1.74E+21	1.359	28.1
17	0.9302	2.50E+19	1.43%	1.74E+21	1.342	28.4
17	0.9460	2.54E+19	1.46%	1.74E+21	1.365	28.0
Ni-SiO_2						
10.6	0.5762	1.55E+19	1.42%	1.09E+21	0.831	28.6
10.6	0.5680	1.53E+19	1.40%	1.09E+21	0.819	29.0
10.6	0.5702	1.53E+19	1.41%	1.09E+21	0.823	28.9
Ni-$SiO_2Al_2O_3$						
10	0.5045	1.36E+19	1.32%	1.03E+21	0.728	30.9
10	0.5101	1.37E+19	1.34%	1.03E+21	0.736	30.5
10	0.4987	1.34E+19	1.31%	1.03E+21	0.719	31.2

4.3.1.3 Nitrogen adsorption isotherms

The adsorption of reactants on the surface of the catalyst is one of the most important steps in catalysis. So, isotherm adsorption is very important to characterize porous solids and obtain qualitatively the type of porous material being used. From this measurement an adsorption curve can be drawn which can then be used to estimate the BET surface area, pore volume and pore size distribution of the solid material, as previously described in Chapter 2 [111].

The adsorption-desorption isotherms for the supports are shown in Figure 4.3.

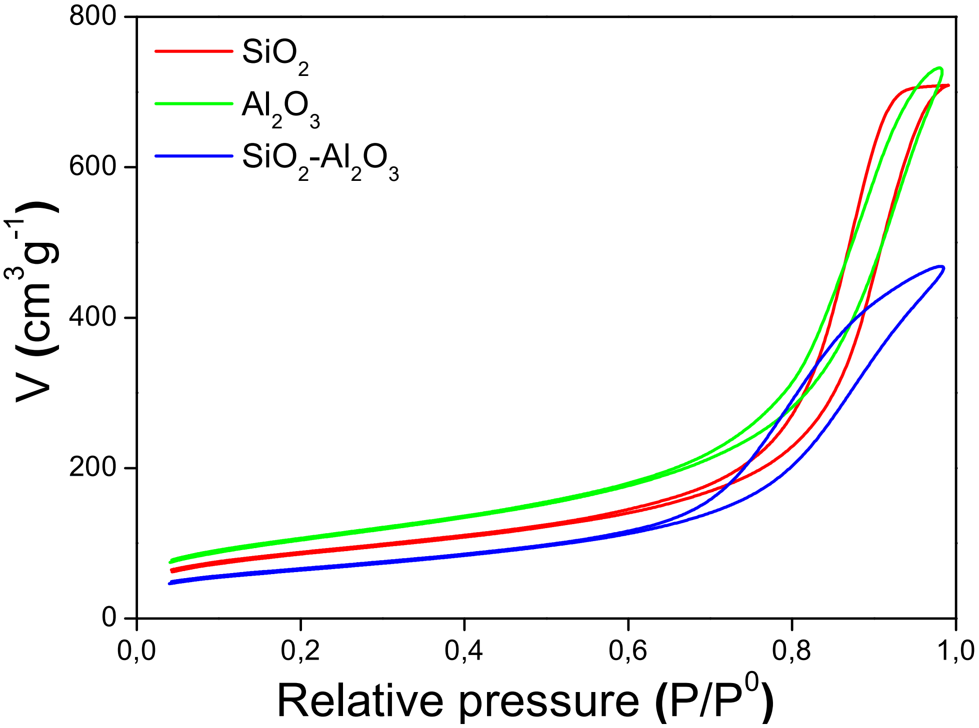

Figure 4.3 Nitrogen adsorption-desorption Isotherms

According to the classification of Brunauer, Deming, Deming and Teller (BDDT), the isotherms correspond to a type IV isotherm [111], characteristic of mesoporous solids; moreover, this type of isotherm presents a characteristic hysteresis loop, where the processes of adsorption and desorption follow different pathways. In Figure 4.3 silica and alumina supports have a type H1 hysteresis loop, attributed to cylindrical pores; while silica-alumina presents a type H2 hysteresis loop, attributed to bottle neck pores. All the textural properties of the catalysts and their corresponding supports are shown in Table 4.4.

Table 4.4 Composition and textural properties of supports and catalysts

Supports	Ni Content (%)	Surface density (atoms nm^{-2})	S_{BET} (m^2 g^{-1})	$^*V_p$ (cm^3 g^{-1})	$^{***}V_0$ (cm^3 g^{-1})	$^{**}V_m$ (cm^3 g^{-1})
Al_2O_3	-	-	226	0.66	0.11	0.55
SiO_2	-	-	312	1.09	0.14	0.94
SiO_2-Al_2O_3	-	-	378	1.01	0.10	0.91
Catalysts						
Ni(8)/Al_2O_3	8.5	4.2	209	0.56	0.10	0.46
Ni(10)/SiO_2	10.6	4.2	262	0.92	0.12	0.80
Ni(10)/SiO_2-Al_2O_3	10.0	3.3	313	0.89	0.14	0.75

* Vp = total volume.

** Vm = mesopore volume.

*** Vo = micropore volume.

Table 4.4 shows that silica-alumina has the highest surface area, followed by silica and then alumina. Also, the mesopore volume is higher than the micropore, which is characteristic for these types of solids. As expected, the surface area and total pore volume of the supports decreased after Ni impregnation and calcination. The surface area of Al_2O_3 decreased by 3% with Ni oxide introduction, while SiO_2 and SiO_2-Al_2O_3 decreased by 16% and 17%, respectively. This suggests that Ni oxide was better dispersed on alumina compared to silica and silica alumina.

4.3.1.4 X-ray diffraction

Figure 4.4 shows the X-ray diffraction patterns for all the calcined catalysts. The XRD patterns show that Ni(8)/γ-Al_2O_3, Ni(10)/SiO_2 and Ni(10)/SiO_2-Al_2O_3 catalysts displayed diffraction peaks at 2θ =37.2, 43.2 and 63° which could be attributed to the cubic NiO phase (111), (200) and (220) lines, respectively (JCPDS 00-044-1159). Also, in the Ni(8)/γ-Al_2O_3 XRD pattern, the γ-Al_2O_3 2θ angles of 37.4°, 45.8°, and 66.9°(JCPDS 86-1410) are present. There were no detectable $NiAl_2O_4$ spinel peaks, although spinels have been identified previously by Sievers, et al.[142] If the spinel was present, it could be highly dispersed within the alumina support or may have formed very small particles below the detection limit of XRD.

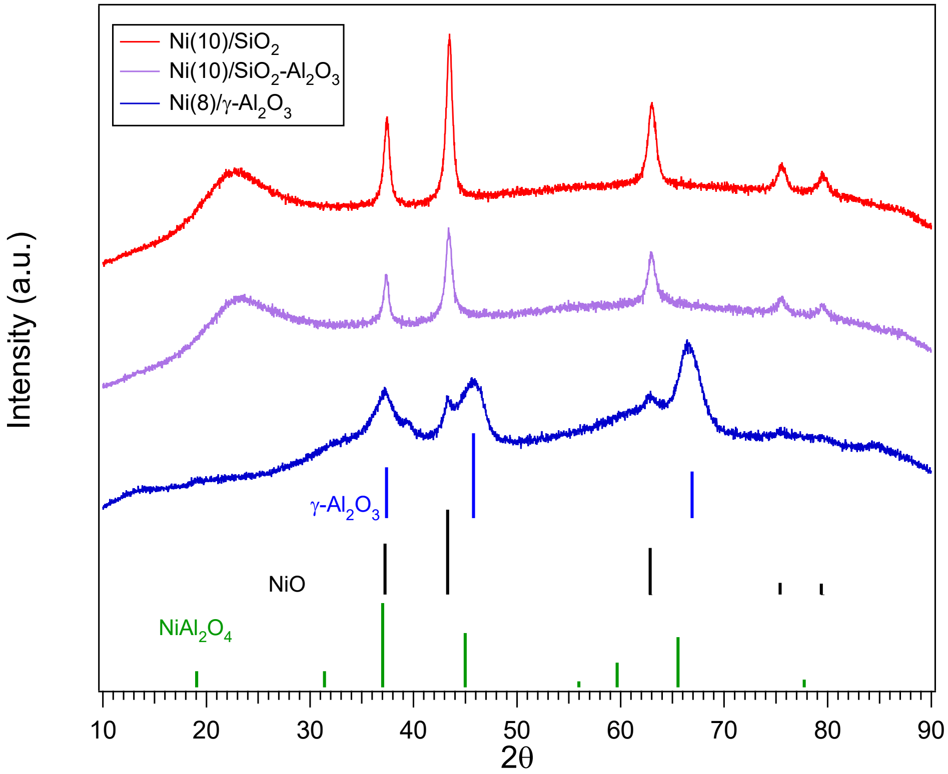

Figure 4.4 X-ray diffraction patterns for supported nickel catalysts.

The sharper peak shapes of NiO in both the SiO_2 and SiO_2-Al_2O_3 supports compared to NiO in γ-Al_2O_3, suggests a larger particle size and a weaker NiO-support interaction. On the other hand, the pattern for the Ni/γ-Al_2O_3 catalyst reveals less intense and broader diffraction peaks, which could be attributed to the existence of smaller particle size, associated with higher dispersion of NiO on the alumina support, as well as a stronger interaction of NiO with this support [143]. The XRD patterns for Ni/SiO_2 and Ni/SiO_2-Al_2O_3 also show a peak around 23° which is characteristic of non-crystalline amorphous silica [144-146]. From the Scherrer equation, we calculated the crystallite size of NiO for each support, choosing the peak at $2\theta = 63°$ that does not overlap with other peaks for Ni/SiO_2 and Ni/SiO_2-Al_2O_3. Three Lorentzian peaks were required to determine the $2\theta = 63°$ peak from non-linear least squares fitting of the Ni/γ-Al_2O_3 XRD pattern. Table 4.5 presents the NiO crystallite size for each nickel supported catalyst, where, Ni/ γ-Al_2O_3 has the smaller crystallite size followed by NiO on silica and NiO/ silica-alumina, as predicted by XRD patterns of their respective oxidized catalyst.

Table 4.5 Crystallite and particle size analysis

Catalyst	**Peak width (FWHM)**	**(2θ)**	**XRD NiO Crystallite size / (nm)**	**Equiv. XRD Ni crystallite size /(nm)**	**TEM Ni Particle size/ (nm)**
NiO/γ-Al_2O_3	1.581°	62.9°	6.2	5.2	4.3
NiO/SiO_2	0.899°	63.0°	9.8	8.2	6.5
NiO/SiO_2-Al_2O_3	0.997°	63.0°	10.8	9.1	7.5

For comparison with TEM data (below) after reduction of NiO particles to Ni metal, the equivalent particle size, D_{Ni}, was estimated from the atomic (AW) and molecular (MW) weights and densities,

$$D_{Ni} = D_{NiO}\left(\frac{\rho_{NiO}}{\rho_{Ni}}\frac{AW_{Ni}}{MW_{NiO}}\right)^{1/3}, \tag{4.3}$$

where $\rho_{NiO} = 6.67\ g/cm^3$ and $\rho_{Ni} = 8.908\ g/cm^3$. The estimated Ni crystallite sizes were about 10% larger than the mean particle size observed by TEM after reduction. We attribute the differences to systematic errors in estimating particle sizes; however, the results provide no evidence of aggregation after reduction to Ni metal.

4.3.1.5 H_2 Temperature programmed reduction (TPR)

The reducibility of the catalysts prepared was investigated by H_2-TPR measurements. The profiles of the Ni catalysts are shown in Figure 4.5. The TPR profiles show that Ni/SiO_2 presents a sharp well defined reduction peak at 343 °C, indicating that the reduction of Ni^{2+} to Ni metal occurs in one step and is characteristic of the presence of Ni^{2+} species in bulk NiO that interacts weakly with the support [147]. A small shoulder can be observed at 400 °C for Ni/SiO_2 which could be due to the presence of small NiO crystallites interacting more strongly with the support. On the other hand, both Ni/γ-Al_2O_3 and Ni/SiO_2-Al_2O_3 present broad double peaks with lower peak area, suggesting the presence of Ni species with different degrees of interaction on these catalysts. The reduction temperatures of Ni/Al_2O_3 are centered at 430 °C and 508 °C, while that of Ni/SiO_2-Al_2O_3 are centered at 350 °C and 420 °C.

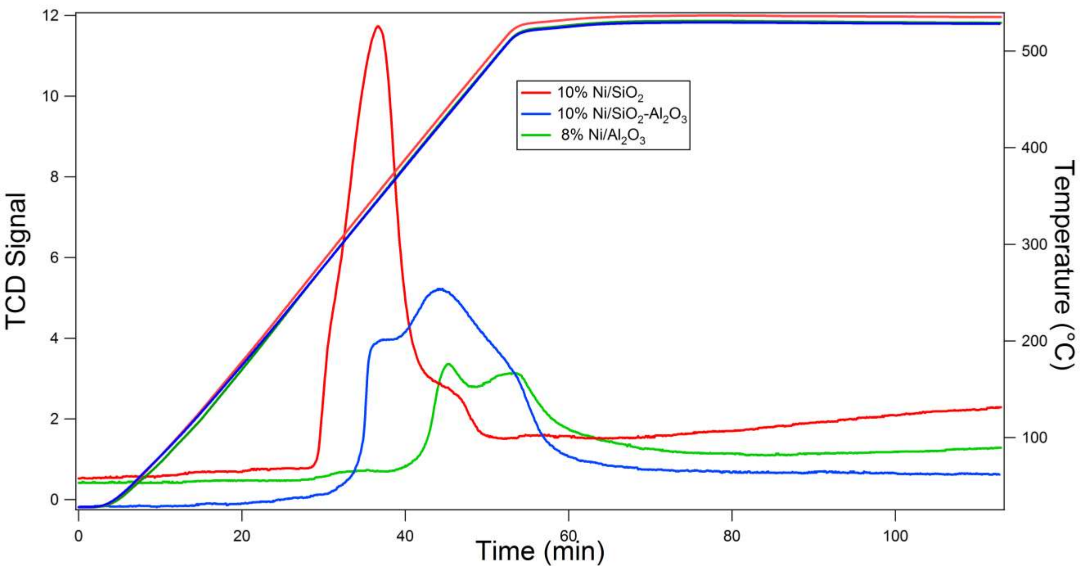

Figure 4.5 Temperature programmed reduction (TPR) for Ni/support catalysts.

It has been reported in the literature that four different nickel oxide species exist: the first one with a temperature range between 250 to 350°C is attributed to NiO crystallites interacting weakly with the support known as "free NiO species" [148], which was observed for Ni/SiO$_2$; a second NiO species which is reducible within 350 °C to 500 °C temperature range is characteristic of NiO interacting strongly with the support; species reduced between 500 °C to 750 °C consists of non-stoichiometric nickel aluminate species (NiO-Al$_2$O$_3$); and that reduced above 750 °C corresponds to the presence of stoichiometric nickel aluminate (NiAl$_2$O$_4$), which could not be confirmed by XRD. In this study, the reduction behavior of the catalysts up to temperatures of 550°C was investigated to provide insights into the nature of Ni species on the catalyst after activation at this temperature. The existence of stoichiometric nickel aluminate on Ni/γ-Al_2O_3 and Ni/SiO_2-Al_2O_3 could not be confirmed by this measurement. What is indisputable, though, is that while Ni/SiO_2 contains mostly free NiO species with a weak interaction of the oxide species with the silica support, Ni/γ-Al_2O_3 and Ni/SiO_2-Al_2O_3 contains a mixture of the previously suggested nickel oxide species. It can also be deduced from this TPR data that Ni/SiO_2 was most easily reduced, followed by Ni/SiO_2-Al_2O_3 and Ni/γ-Al_2O_3, which reflects also the strength of the Ni-support interaction. Mortensen et al. [95] reported a similar behavior for Ni/Al_2O_3 catalysts where there was less reduction of the nickel species forming mixed oxides or spinels, retarding reduction.

The data agrees well with the XRD data presented in Figure 4.4, where sharper XRD peaks are related to weaker interaction of the active metal and the support, reflected in the TPR data with a lower reduction temperature of isolated NiO species and a single reduction peak for Ni/SiO_2.

4.3.1.6 Transmission electron microscopy (TEM)

TEM analysis was carried out on freshly reduced catalysts and the results are shown in Figure 4.6 along with their particle size distribution. By examination of over 200 particles, the particle size distribution for Ni in Ni/SiO_2-Al_2O_3 ranged from 4-16 nm with a mean particle size of 7.5 nm. Figure 4.6b shows the particle size distribution for Ni in Ni/SiO_2, which varied from 4-18 nm with a mean particle size of 6.5 nm. Figure 4.6c shows that the particle size distribution for Ni in Ni/Al_2O_3 was narrower, varying between 2-10 nm with a mean size of 4.3 nm. The comparison of the TEM average particle size of the three Ni supported catalyst in Table 4.5 shows the same trend as found from XRD for NiO. Note that the bright areas in the TEM images were due to the copper grid.

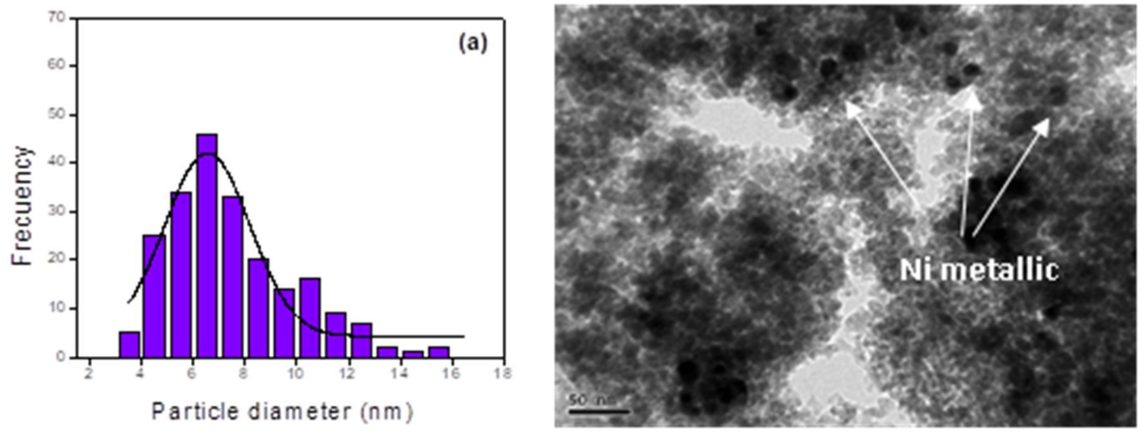

Figure 4.6 TEM micrographs and particles size distribution for a) Ni (10)/SiO_2-Al_2O_3

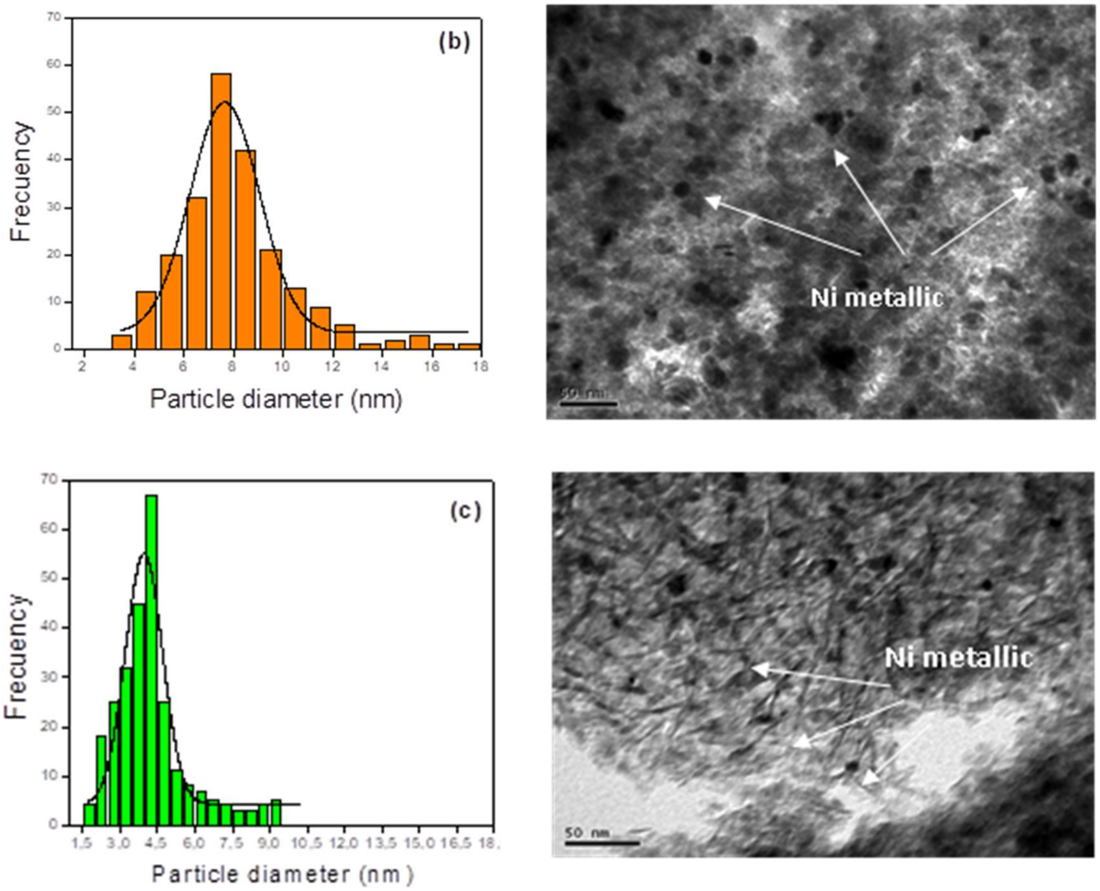

Figure 4.6- continued b) Ni(10)/SiO_2 and c) Ni(8)/Al_2O_3.

4.3.1.7 Surface acidity of supported nickel catalysts

The surface acidity of the supported Ni catalysts was estimated from potentiometric titration curves using n-butylamine as a probe molecule. The reported results include maximum acidity strength of surface sites and total number of acid sites normalized by the surface area. Figure 4.7 shows the titration curve of reduced catalysts.

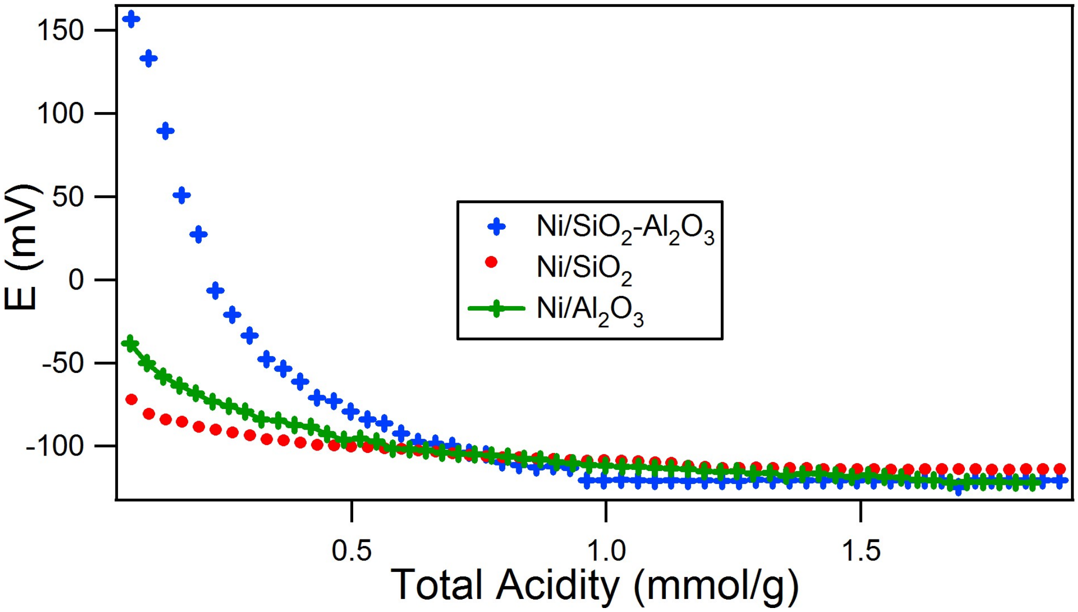

Figure 4.7 Potentiometric curves for Ni/Support catalysts

Results are summarized in Table 4.6. Based on the criteria proposed by Cid and Pecchi [118], Ni/SiO_2-Al_2O_3 displayed strong acid sites with E_0> 100 mV, whereas Ni/Al_2O_3 and Ni-SiO_2 displayed weak acid sites with $0 < E_0 < 100$ mV[118].

Table 4.6 Total acidity determined by n-butylamine titration

Catalyst	E_o (mV)	Total Acid strength	Density of Acid sites (molecules nm^{-2})
Ni/SiO_2-Al_2O_3	156.8	Strong	1.85
Ni/Al_2O_3	-38.1	Weak	2.60
Ni/SiO_2	-72	Weak	2.28

The acidity increased in the order Ni-SiO_2 < Ni/Al_2O_3 < Ni/SiO_2-Al_2O_3. A similar trend has been reported by Guimon et at. [149]. The density of acid sites was estimated from the amount of n-butylamine titrated until it reached a plateau (constant potential) in the titration curve. The data show that Ni/Al_2O_3 had the highest density of acid sites followed by Ni/SiO_2 and then Ni/SiO_2-Al_2O_3. This method gives a general measurement of acidity of solids and is not able to distinguish between Brønsted or Lewis acid sites.

4.3.1.8 X-ray photoelectron spectroscopy

All the catalysts were characterized by XPS to identify and quantify surface species present on the catalysts. All the catalysts were reduced in-situ and were not exposed to air prior to XPS analysis. The XPS spectra of the Ni 2p region of the catalysts (Ni/SiO_2, Ni/SiO_2-Al_2O_3, and Ni/γ-Al_2O_3) are shown in Figure 4.8 (a), (b) and (c), respectively.

The spectrum for Ni(10)/SiO_2 shown in Fig. 4.8(a) reveals peaks at binding energies (BE) of 852.2 eV and 856.1 eV, attributed to metallic Ni and Ni^{2+} species, respectively. [150]. Figure 4.8(b) shows that for Ni/SiO_2-Al_2O_3, three overlapping peaks were observed at 852.5 eV, 856.3, and 862.5 eV which correspond to Ni^0, the Ni^{2+} $2p^5 3d^9 L^{-1}$ and the Ni^{2+} $2p^5 3d^8$ transitions, respectively. In general, all the catalysts contained Ni^{2+} and Ni^0 species, the presence of non-reducible Ni species (some higher than 50%) might be attributed to partial re-oxidation in the XPS chamber or impurities in the carrier gas may cause reoxidation of the nickel metal to the oxide. According to previous literature [149] reactive Ni^0 particles could be re-oxidized even in ultra-high vacuum atmosphere.

Figure 4.8(c) shows the spectrum of the Ni $2p_{3/2}$ spectrum for (8)Ni/γ-Al_2O_3 has three overlapping peaks at a BE of 853.0, 856.5, and 862.5 eV, indicative of Ni^0 and Ni^{2+} species. Compared to the BE of stoichiometric NiO (854.5 eV)[149], the higher binding energy suggests that Ni^{2+} does not exist as free NiO and that there is a strong interaction between Ni species and alumina. The XPS spectrum of $NiAl_2O_4$, for nanomaterials confirmed by XRD to have the spinel structure, is similar to the peaks at 856.5 and 862.5 eV. The peak at 856.5 eV is generally assigned to a charge transfer process from a ligand to the Ni atoms. Ewbank, et al.[142] have shown, with TEM that surface aluminate species exist and correspond to higher reduction temperatures in TPR. The XPS data therefore indicates the existence of aluminate type species on the Al_2O_3 component of the supports. However, the existence of spinel in this case is not completely confirmed, given that the particle size could be below the detection limit of XRD.

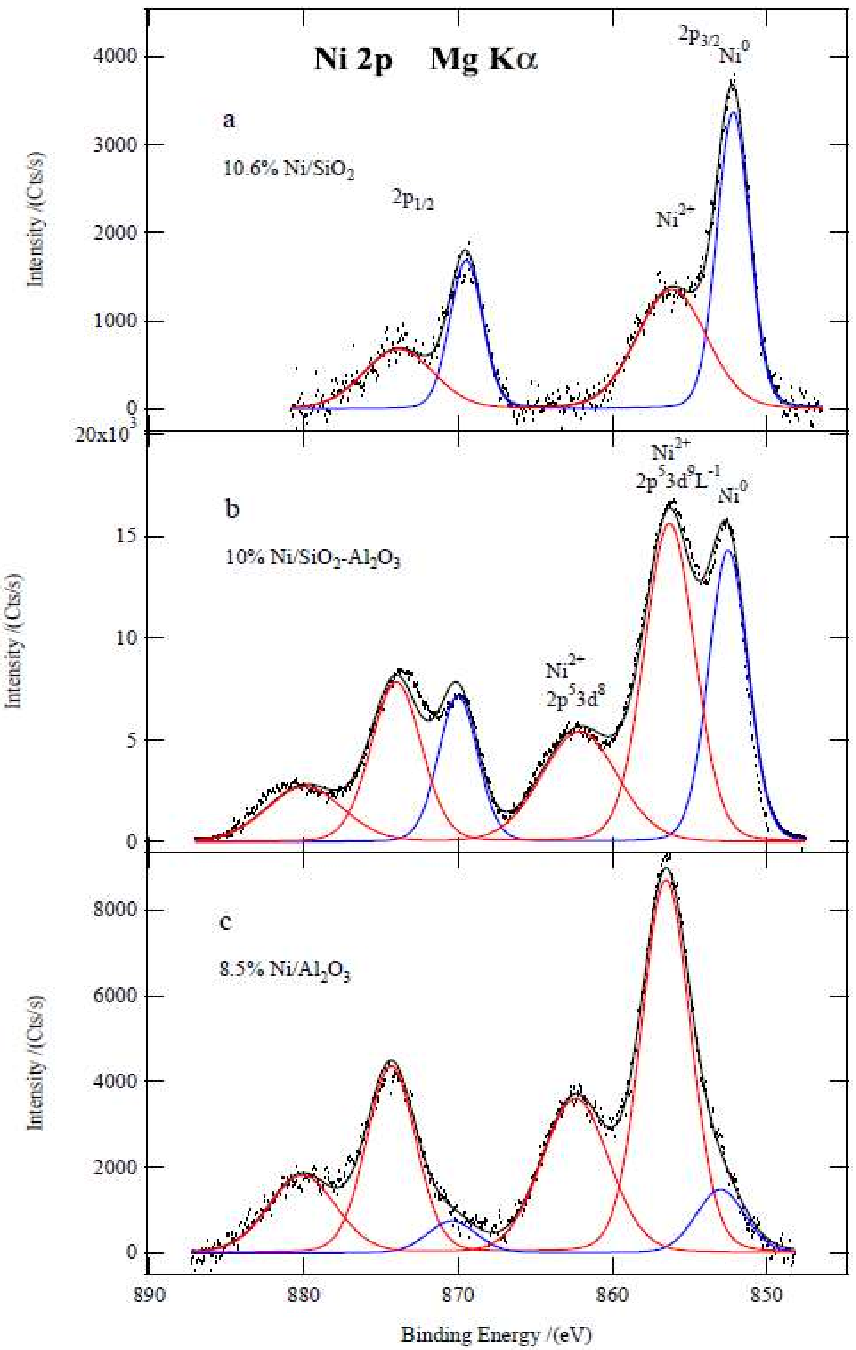

Figure 4.8 XPS spectra of Ni 2p region of the Ni supported on (a) SiO_2, (b) SiO_2-Al_2O_3 and (c) Al_2O_3.

Table 4.7 presents a summary of the binding energies and the amount of Ni^0 in each catalyst. Ni(8) /Al_2O_3 has 10% of Ni^0 and 90% is Ni^{2+}. In Ni(10)/SiO_2-Al_2O_3, nickel metal is present at 32% and 68% as Ni^{2+} species and Ni (10.6)/SiO_2 contains 54% of nickel metal and 46%of Ni^{2+}.

Table 4.7 Binding energies (eV) of core-levels and atomic surface ratios of H_2 reduced Ni catalysts

	Al2p	**Si2p**	**$Ni2p_{3/2}^0$ $Ni2p_{3/2}^{2+}$**	**O1s**	**Ni/Al(Si) at**	**Al/Si at**
Ni(8)/Al_2O_3	74.5	-	853.0 (10) 856.5 (90)	531.3	0.076	-
Ni(10)/SiO_2-Al_2O_3	74.4	103.4	852.5 (32) 856.3 (68)	530.2	0.038	0.815
Ni(10.6)/SiO_2	-	103.4	852.2 (54) 856.1 (46)	532.8	0.023	-

These results agree with TPR data, where Ni on alumina had a broad double peak above 400 °C characteristic of Ni species that interacts strongly with the support and are harder to reduce. Ni(10)/SiO_2-Al_2O_3 catalyst also presented broad double peaks with maxima at around 400 and 430 °C, also suggesting two types of Ni species interacting strongly with the support, given the lower reduction temperature peak, suggests that this catalyst can be easier to reduced compared to that of alumina. On the other hand, Ni(10)/SiO_2 only a single sharp peak was observed, characteristic of "free NiO" species that interact weakly with the support and hence are easier to reduce.

4.3.1.9 NH_3 Temperature programmed desorption

Ammonia-TPD analysis was conducted on the catalysts with the different supports that contain approximately the same amount of metal on the surface of each support. The area under the curve represents the total acidity, and the maximum peak temperature indicates the acid strength, where the acid sites have been classified as weak (T< 300 °C), medium (300 °C< T < 500 °C), or strong (T> 500 °C)[151]. The desorption peak profiles over the whole temperature range indicated the presence of acid sites of different strength. The acid sites distribution was determined by fitting a Gaussian function to deconvolute the peaks shown and calculating the areas under the curve corresponding to the acid site strength classification. The NH_3-TPD profiles of the reduced catalysts are shown in Figure 4.9 and summarized in Table 4.8. All catalysts have intense peaks in the low temperature region, indicating the presence of weak acid sites on all catalysts. The medium strength acid sites had a peak maximum of 321 °C for the Ni/Al_2O_3 catalyst, followed by Ni/SiO_2-Al_2O_3 at 340 °C and with very low intensity for Ni/SiO_2 catalyst. The TPD profile for reduced Ni/Si-Al catalyst, gave rise to three overlapping peak in the weak acid temperature region, while reduced Ni/Al_2O_3 presented overlapping double peaks in the weak acid temperature region. In the strong acid range, Ni/SiO_2-Al_2O_3 gave one well resolved peak at 650 °C, while reduced Ni/Al_2O_3 produced a peak above 500 °C, with a small shoulder above 800 °C. The

TPD profile of Ni/SiO_2 gave rise to two overlapping peaks in the weak acid temperature range Shown in Figure 4.9 a small shoulder in the medium acid temperature range at 300 °C and a double peak above 600 °C, but their low intensity is consistent with the SiO_2 support having low surface acidity. Note that this method cannot distinguish between Bronsted and Lewis acid sites.

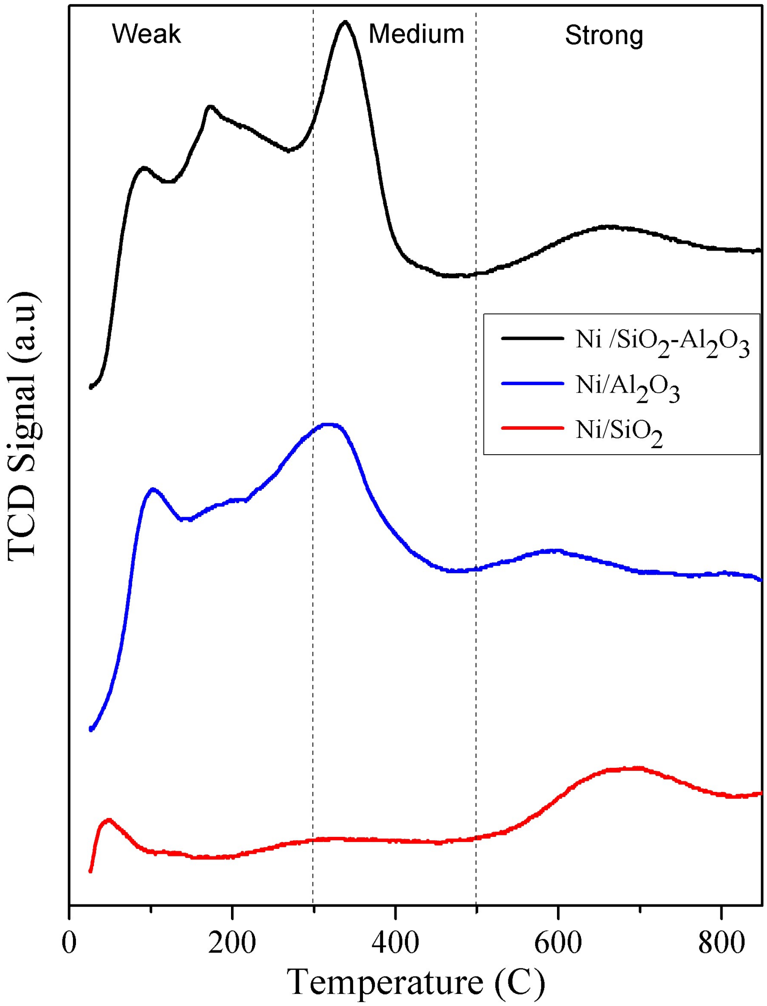

Figure 4.9 NH_3-TPD profiles of Ni/Support catalysts

Table 4.8 shows that the total amount of acid sites ranged from 154 to 1020 umol NH_3/g; however, the acid site distribution indicates that the predominance of weak acid sites on Ni/SiO_2-Al_2O_3 while Ni/Al_2O_3 contains a relatively even distribution of total acid sites.

Table 4.8 NH_3-TPD summary for Ni/Support catalysts

Catalysts	**Weak acid sites (umol NH_3/g)**	**Medium acid sites (umol NH_3/g)**	**Strong acid sites (umol NH_3/g)**	**Total acid sites (umol NH_3/g)**
Ni/SiO_2	40	17	97	154
Ni/SiO_2-Al_2O_3	640	240	120	1000
Ni/Al_2O_3	360	380	280	1020

4.3.2 Comparison of catalytic activity of Ni/support

Figure 4.10 (a,b and c) shows the conversion of guaiacol and yield of products as a function of time for the three Ni/Support catalysts. Several compounds were detected in the products throughout the reaction. Figure 4.10(a) shows that the main products from the conversion of guaiacol on the Ni/SiO_2 catalyst after 4 h is cyclohexane, followed by methanol, cyclohexanol, phenol, benzene and cyclohexanone. In all Ni/support catalysts phenol is an intermediate because it reaches a maximum and then decreased.

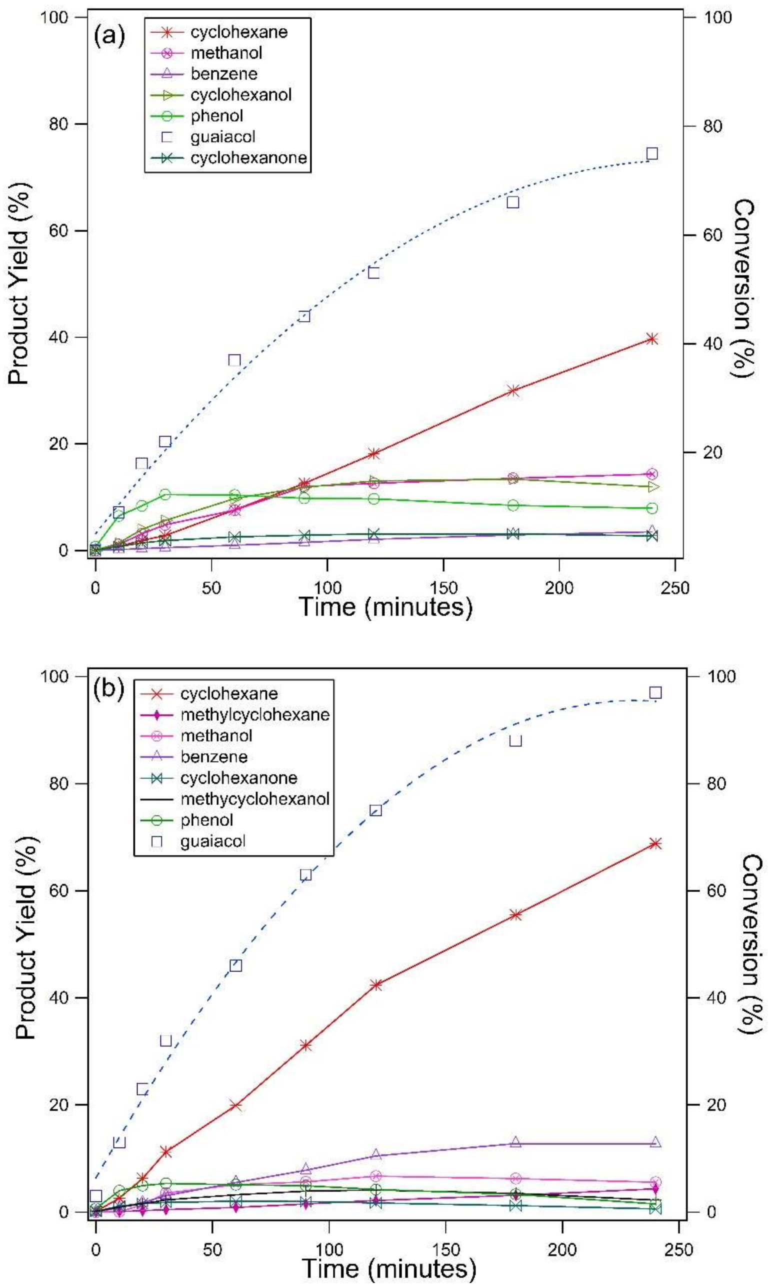

Figure 4.10 Conversion of guaiacol over (a)Ni/SiO_2, (b)Ni/Al_2O_3 and (c) Ni/SiO_2-Al_2O_3.

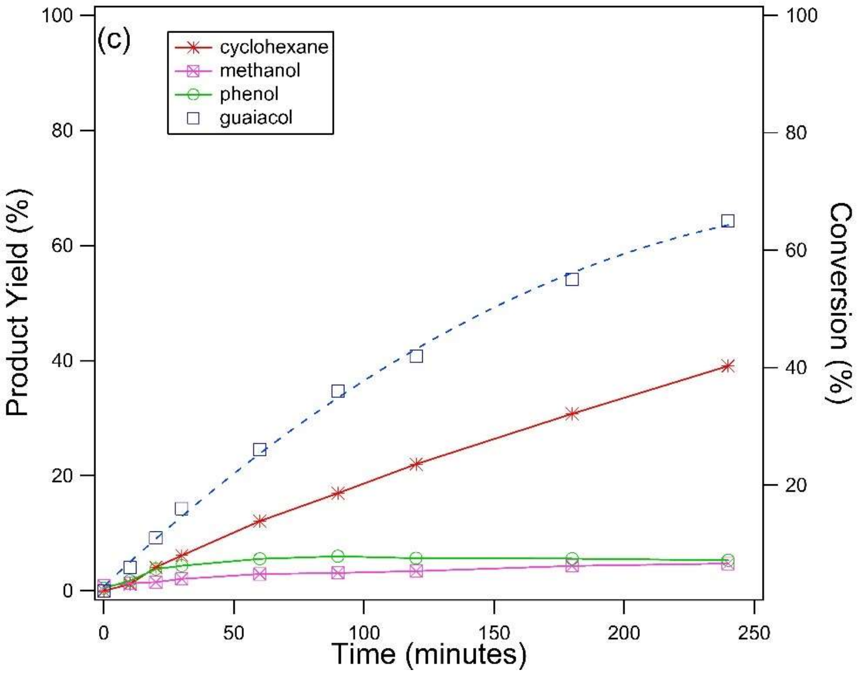

Figure 4.10 Continued.

Other products including hexane, methylcyclohexane, cyclohexene, toluene and 2-methylcyclohexanone were detected in quantities lower than 1.5%. Figure 4.10 (b) shows that cyclohexane was also the main product from the conversion of guaiacol over the Ni/Al_2O_3 catalyst. However, benzene was more prominent whereas methanol was observed in much lower amounts compared to the products over Ni/SiO_2. Other appreciable products observed are methylcyclohexane, methylcyclohexanol, phenol and cyclohexanone.

For the Ni/SiO_2-Al_2O_3 catalyst (Fig. 4.10 (c)), cyclohexane was the major product while methanol and phenol were also observed. Trace amount of methylcyclohexane, hexane, cyclohexene, toluene, cyclohexanone, methycyclohexanone, cyclohexanol, methylcyclohexanol, p-cresol and catechol were observed but are not shown in 4.10 (c).

Overall the main conversion of guaiacol consist of three major steps. A reaction scheme for the conversion of guaiacol is proposed in Figure 4.11. The first step is the breaking of the O-CH_3 bond of the methoxy group, resulting in the formation of phenol, also known as the demethylation route (DMO) [46, 47]. The second step is the hydrogenation (HYD) of the aromatic ring to produce cyclohexanol. Phenol also can undergo direct deoxygenation (DDO) to produce benzene. The last step is the deoxygenation of cyclohexanol, which can occur by intramolecular dehydration of the hydroxyl group, with cyclohexene as intermediate, and subsequent hydrogenation to cyclohexane, in agreement with previous data reported by Mochizuki et al [94] in the conversion of guaiacol and Jin et al [152] in the conversion of anisole.

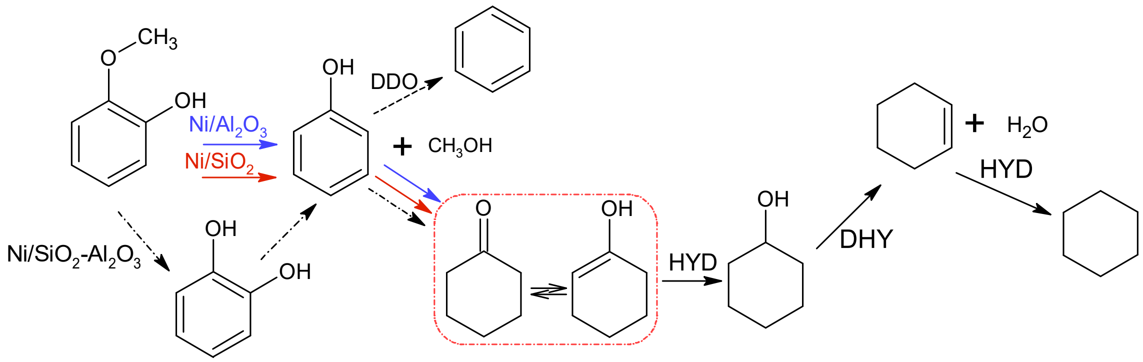

Figure 4.11 Guaiacol Reaction Scheme.

Hydrogenation sites in Ni/supported catalyst are confirmed by the production of cyclohexanol (produced from phenol hydrogenation). The formation of methylated compounds can be attributed to the methyl transfer group from guaiacol to aromatic rings present. It is known that acid sites present catalyze this type of reaction, previously suggested by Zhu et al[153].

The initial rate of reaction (mol g^{-1} min^{-1}) for each supported nickel catalyst are summarized in Figure 4.12, obtained from the slope of guaiacol conversion for each plot in Figure 4.10.

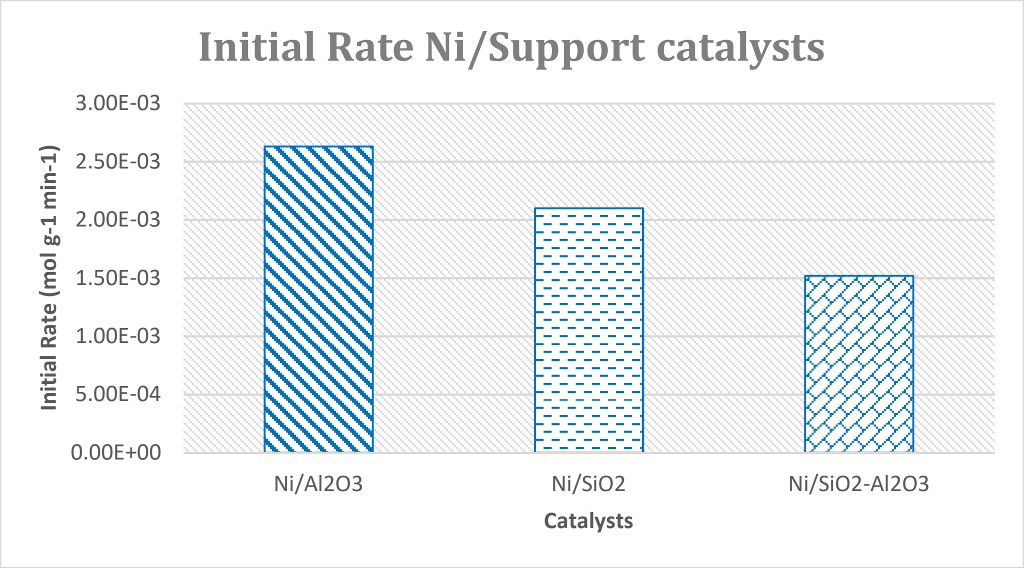

Figure 4.12 Initial Reaction rates of guaiacol on different supported Ni catalyst.

Figure 4.12 depicts that Ni (8.5)/Al_2O_3 was the catalyst with the highest catalytic activity followed by Ni/SiO_2 and Ni/SiO_2-Al_2O_3. The highest activity is attributed to the smallest particle size present in the Ni/Al_2O_3 catalyst that would result in better dispersion of the metal on the alumina support. This conclusion is also supported by the highest Ni/Al(Si) peak area ratio in the XPS (Table 4.7) and as assessed by TEM with a particle size distribution of 4.3 nm (Figure 4.6c) and the metallic particle size of nickel estimated from the NiO particle size estimated from XRD.

Ni/SiO_2 had an intermediate rate of reaction and had a bigger particle size compared to that of the nickel on alumina. The TEM average particle size distribution was 6.5 nm. The Ni/SiO_2-Al_2O_3 was the catalyst with lowest catalytic activity, due to formation of larger clusters of nickel on the surface of the support with an average size of 7.5 nm. These results are also in agreement with the intensity ratios obtained by XPS.

Product distributions at 10% conversion for all three supported catalysts are exhibited in Figure 4.13.

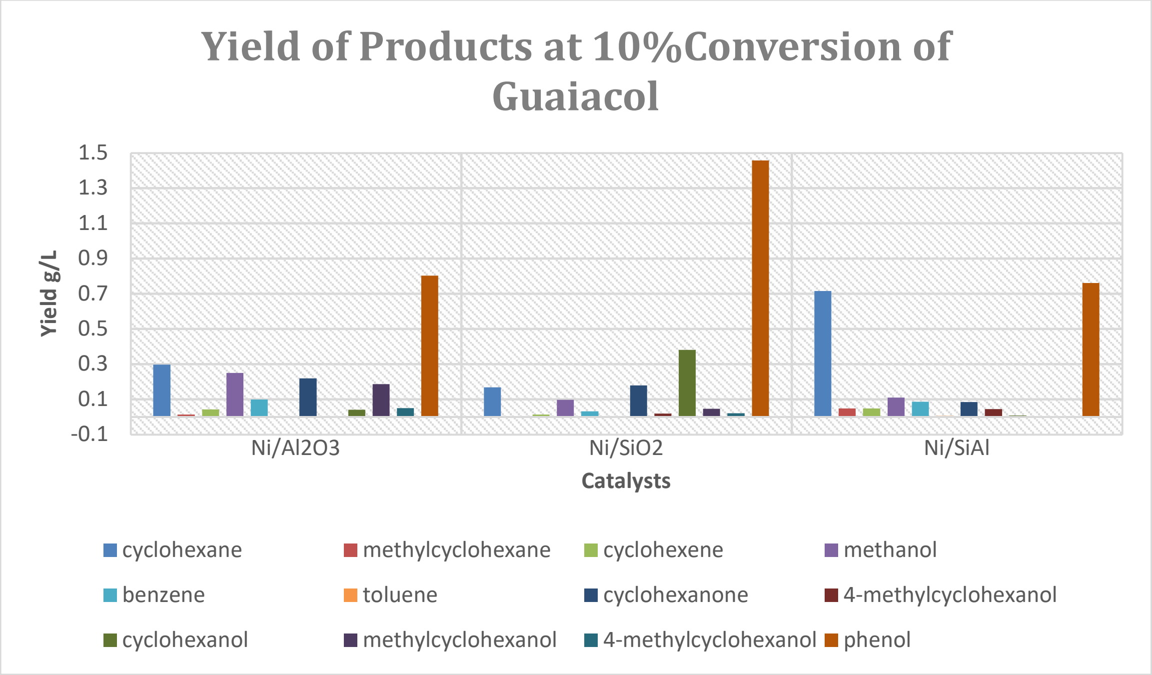

Figure 4.13 Yield of Products at 10% conversion of guaiacol.

All three catalysts at 10 % conversion produced phenol as the major compound. The formation of phenol is favored Ni/SiO_2 due to the less acidic character of the catalyst which has been reported by Sepulveda et al[76]. About the same quantity of phenol was produced on Ni/Al_2O_3 and Ni/SiO_2-Al_2O_3 catalysts. The selectivity to cyclohexanol decreased in the following order Ni/SiO_2, Ni/Al_2O_3 and Ni/ SiO_2-Al_2O_3. This trend is comparable to their ammonia TPD acidities reported. In contrast the amount of cyclohexane produced, decreased in the reverse order, suggesting that strong acid sites favor formation of cyclohexane by dehydration of cyclohexanol[94]. Methylated compounds formed are related to acidic supports, because strongly acidic catalysts favor isomerization products during the conversion of guaiacol. Demethylation activity to produce catechol is attributed to metal sites [47], only Ni/ SiO_2-Al_2O_3 had traces of this compound detected, it does not mean that the product was not formed, but the demethylation reaction on other supports could be too fast compared to the nickel silica-alumina. However, the presence of methanol formed during the conversion of guaiacol is a pathway more likely to take place, thus explaining the low production of catechol.

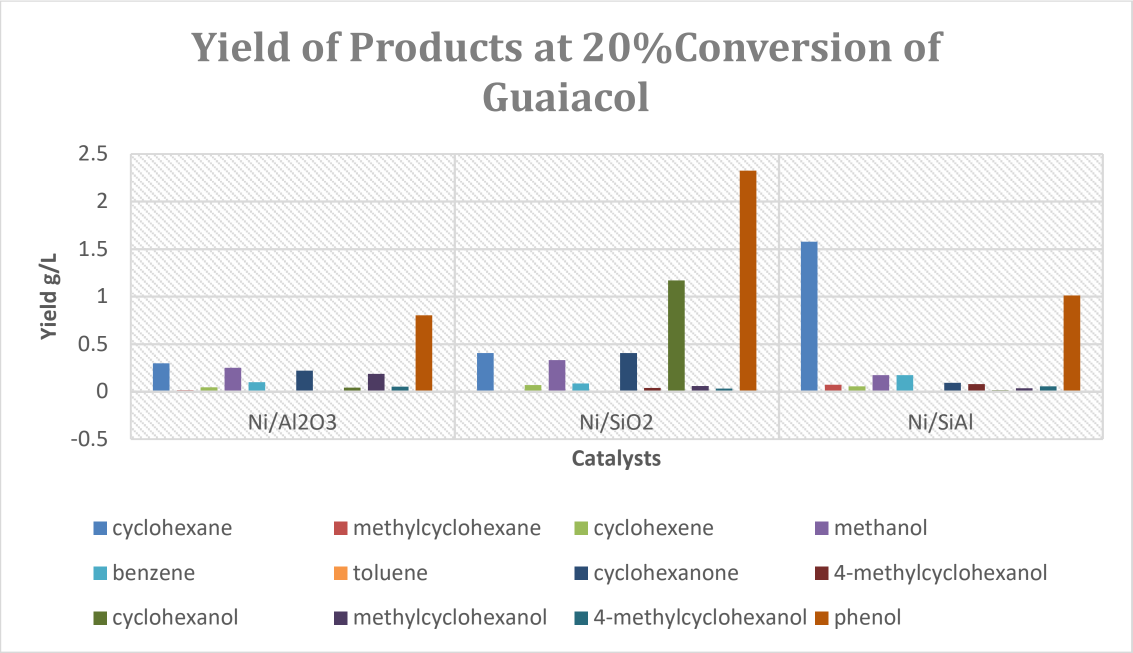

Figure 4.14 Product distribution at 20%conversion of guaiacol

The product distribution of guaiacol at 20% conversion was also calculated to compare changes from that at 10%, shown in Figure 4.14. The major compound is again phenol, decreasing in the following order Ni/ SiO_2, Ni/ SiO_2-Al_2O_3 and Ni/ Al_2O_3. Cyclohexanol selectivity decreased in the following order Ni/ SiO_2, Ni/ Al_2O_3 and Ni/ SiO_2-Al_2O_3, the same as the results observed at 10% conversion. The selectivity to cyclohexane was highest for Ni/SiO_2-Al_2O_3, followed by Ni/ SiO_2 and Ni/ Al_2O_3. It is not clear why more cyclohexane was produced on Ni/SiO_2 compared to Ni/Al_2O_3 given that the latter is much more acidic than the former. Mortensen et al. [95] reported the conversion of phenol of Ni/SiO_2 catalyst with 5% loading of metal, the major compounds found were cyclohexane and cyclohexanol, in agreement with our findings.

4.3.3 Effect of Nickel loading on alumina catalysts

4.3.3.1 Nitrogen adsorption Isotherms vs. Nickel loadings on alumina

Specific surface area (S_{BET}), pore volume (V_p), micropore volume and mesopore volume of the calcined Ni on alumina catalysts was determined from N_2 adsorption isotherms. In Table 4.9 there is a summary with all textural properties for each nickel loading on alumina. The decrease in surface area is relatively low at first, ranging from 3 to 12% for the first four loadings, indicating better particle dispersion on the support. Pore volume, mesopore and micropore volume do not have a huge variation for the first four catalysts, suggesting that the Ni species impregnated are homogeneously dispersed on the Al_2O_3 support. Ni(13) and Ni(17) have the biggest decrease in surface area by 18 and 41% respectively; also, there is a small decrease in pore volume and mesopore volume. The micropore volume has the smallest value for the highest nickel loading.

Table 4.9 Surface Area of Ni loadings on alumina

Catalysts	Ni Content (%)	Surface density (atoms nm^{-2})	S_{BET} (m^2 g^{-1})	$^*V_p$ (cm^3 g^{-1})	$^{***}V_0$ (cm^3 g^{-1})	$^{**}V_m$ (cm^3 g^{-1})
Ni(5)/Al_2O_3	5.3	2.5	220	0.61	0.10	0.51
Ni(6)/Al_2O_3	6.0	2.9	209	0.59	0.09	0.50
Ni(8)/Al_2O_3	8.5	4.2	209	0.56	0.10	0.46
Ni(10)/Al_2O_3	10.1	5.2	198	0.55	0.09	0.46
Ni(13)/Al_2O_3	13.2	7.2	186	0.42	0.09	0.33
Ni(17)/Al_2O_3	17.0	13	133	0.35	0.06	0.29

* Vp = total volume.

** Vm = mesopore volume.

*** Vo = micropore volume.

4.3.3.2 Temperature programmed reduction

Figure 4.15 shows the reduction profiles of nickel catalysts supported on alumina. In the figure it is observed that all peaks have wide reduction temperature ranges, between 300 and 515 °C, assigned to the reduction of Ni^{2+} species to Ni^0 that interact differently with the alumina. The TPR curves for Ni(5) show three distinct reduction peaks, at 300 °C, 413 °C and 500 °C, where the lower temperature peak is associated with isolated NiO species that comes from the un-calcined salt precursor, higher temperature peaks are characteristic of bulk type NiO species that interact strongly with the support.

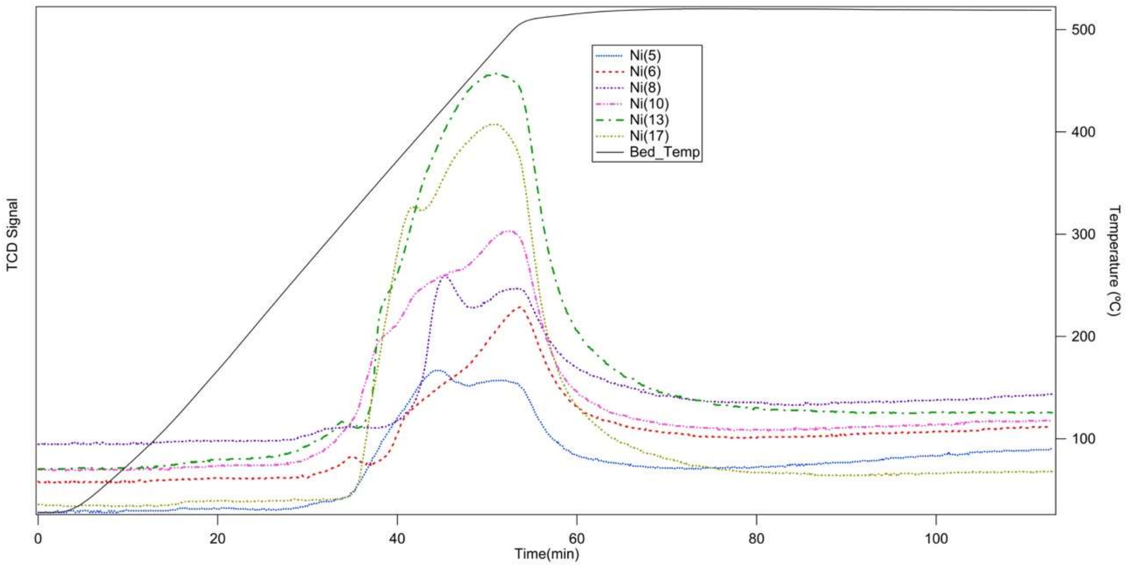

Figure 4.15 TPR for catalysts with varying nickel loading on alumina.

Three of the lowest nickel loading presented low temperature reduction associated with NiO that interacts very weakly with the support.

A lower metal/support interaction leads to lower temperature reduction peaks. While increasing the amount of nickel loaded onto the alumina support there is a clear increase in the hydrogen consumption, hence a bigger reduction peak. Also, there is a small shift to lower temperatures as the metal loading increases; this behavior could be attributed to a lower interaction between the NiO with the support due to an increase in the particle size with the metal content.

4.3.3.3 XRD effect of Ni loading on alumina

The XRD patterns of Ni/γ-Al_2O_3 samples with varying nickel loadings from 5% to 17% are shown in Figure 4.16. Two distinct phases are observed. As the percentage of Ni in the sample increased, the $2\theta = 42°$ and 63° NiO peaks started to be distinguishable from the support, starting at 8.5% Ni, indicating an increase in the metal loading as well as the particle size of NiO on the support.

Also new peaks are more distinguishable at higher loading number at 10, 13 and 17% Ni content. Two new peaks appeared at $2\theta = 76$ and 79° characteristic of the (311) and (222) cubic planes of NiO with larger particle size. Still, it is not easy to distinguish the Al_2O_3 from $NiAl_2O_4$ phase, although a shift in the (211) Al_2O_3 peak at $2\theta = 66.7°$ to lower angle is evidence of nickel species incorporated into the structure of the alumina to form $NiAl_2O_4$ [154]. The lowest nickel loading have no specific peaks for the oxide phase, possibly due to the size of the particles and/or the amount impregnated as well as the detection limit of the XRD instrument.

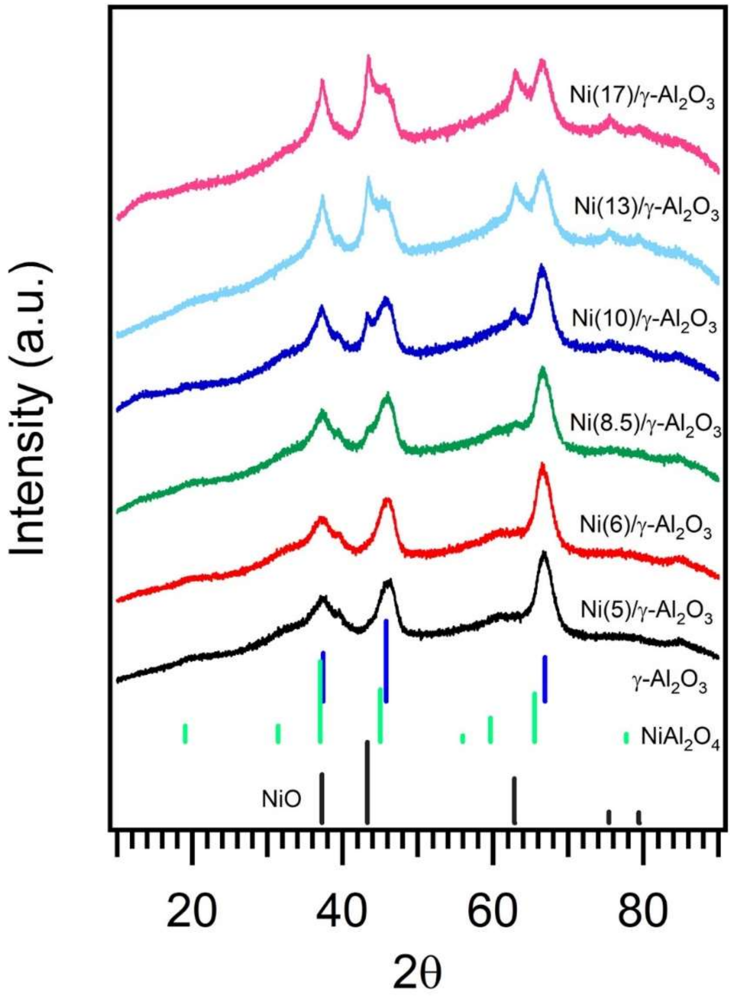

Figure 4.16 X-ray diffraction patterns for calcined Ni loadings on alumina support

4.3.3.4 XPS effects of Ni loadings

All the catalysts were characterized by XPS to identify and quantify surface species present on the catalysts. The XPS spectra of the Ni 2p region of the Ni loading on alumina catalysts (5,6,10,13 and 17%) are shown in Figure 4.17 a-e.

All spectra show three overlapping peaks that were observed at 853 eV, 856.5, and 862.5 eV, which correspond to Ni^0 and Ni^{2+} species, respectively. In general, all the catalysts contained Ni^{2+} and Ni^0 species, the reducibility of Ni increased with the loading, and some Ni species were non-reducible due to formation of spinel or mixed oxides. Also, according to previous literature [149] reactive Ni^0 particles could be re-oxidize even in ultra-high vacuum atmosphere.

Compared to the BE of stoichiometric NiO (854.5 eV)[149], the higher binding energy suggests that Ni^{2+} does not exist as free NiO and that there is a strong interaction between Ni species and alumina.

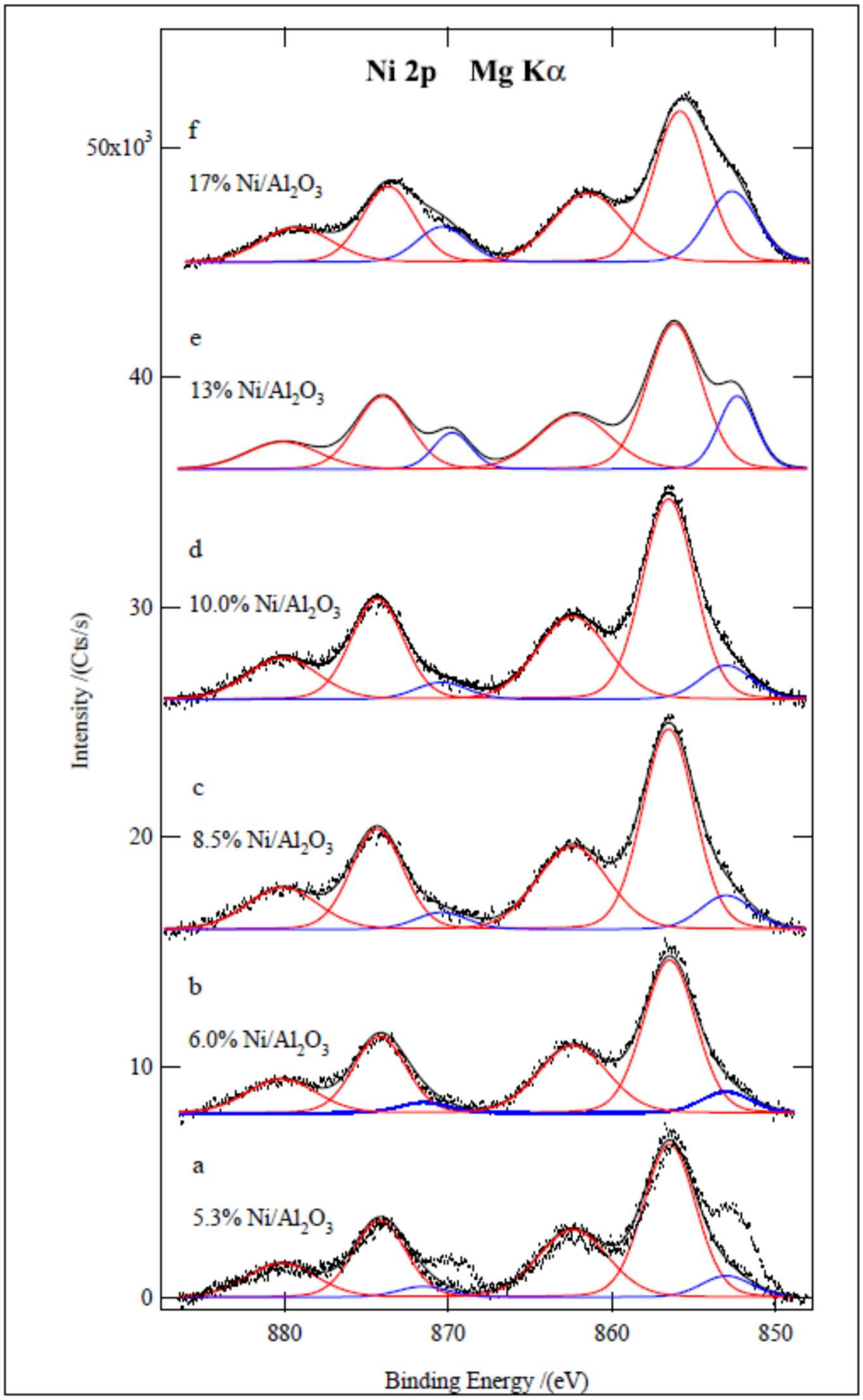

Figure 4.17 XPS Ni 2p spectra for varying Ni loading on Al_2O_3.

As the Ni loading was increased there was a clear trend for increased reducibility of NiO to Ni metal. From literature it has been reported that nickel spinel could be formed at low loadings, Ni diffuses through the alumina support forming the spinel [142] while further increasing the amount of nickel on the surface will create “free NiO” which is more reducible, thus increasing the Ni metal present on the surface. The Ni^{2+} is centered at 856.5 eV without changing much as the loading of Ni increased. Although it is not clear whether any contamination of the chamber was responsible for the reoxidation of the nickel.

Table 4.10 XPS of Nickel loading on Al_2O_3

	Al2p	**Si2p**	**$Ni2p_{3/2}^{0}$** **$Ni2p_{3/2}^{2+}$**	**O1s**	**Ni/Al(Si) at**	**Al/Si at**
Ni(5.3)/Al, H_2	74.5	-	853.0 (6) 856.5 (94)	531.4	0.048	-
Ni(6)/Al, H_2	74.5	-	853.0 (7) 856.5 (93)	531.5	0.066	-
Ni(8.5)/Al, H_2	74.5	-	853.0 (10) 856.5 (90)	531.3	0.076	-
Ni(10)/Al, H_2	74.5	-	852.5 (8) 856.0 (92)	531.4	0.165	-
Ni(13)/Al, H_2	74.5	-	852.5 (19) 856.2 (81)	531.5	0.211	-
Ni(17)/Al, H2	74.5	-	852.7 (22) 855.8 (78)	531.3	0.296	-

4.3.3.5 TEM

Figure 4.18 shows TEM particle size distributions for Ni/γ-Al_2O_3 catalysts with varying Ni loadings; (a)Ni(5), (b) Ni(6), (c) Ni(8), and (d) Ni(10). The particle sizes could not be estimated for higher nickel loading of 13 and 17% due to agglomerations observed on the TEM images. The particle size distribution for Ni(5) and Ni(6) was 1.5-9 nm centered at 3.8 nm and 3.7 nm respectively. For Ni (8) the distribution was 2-10 nm centered at 4.3 nm, with a broader distribution for Ni(10) between 1.5-10.5 nm centered at 4.5 nm.

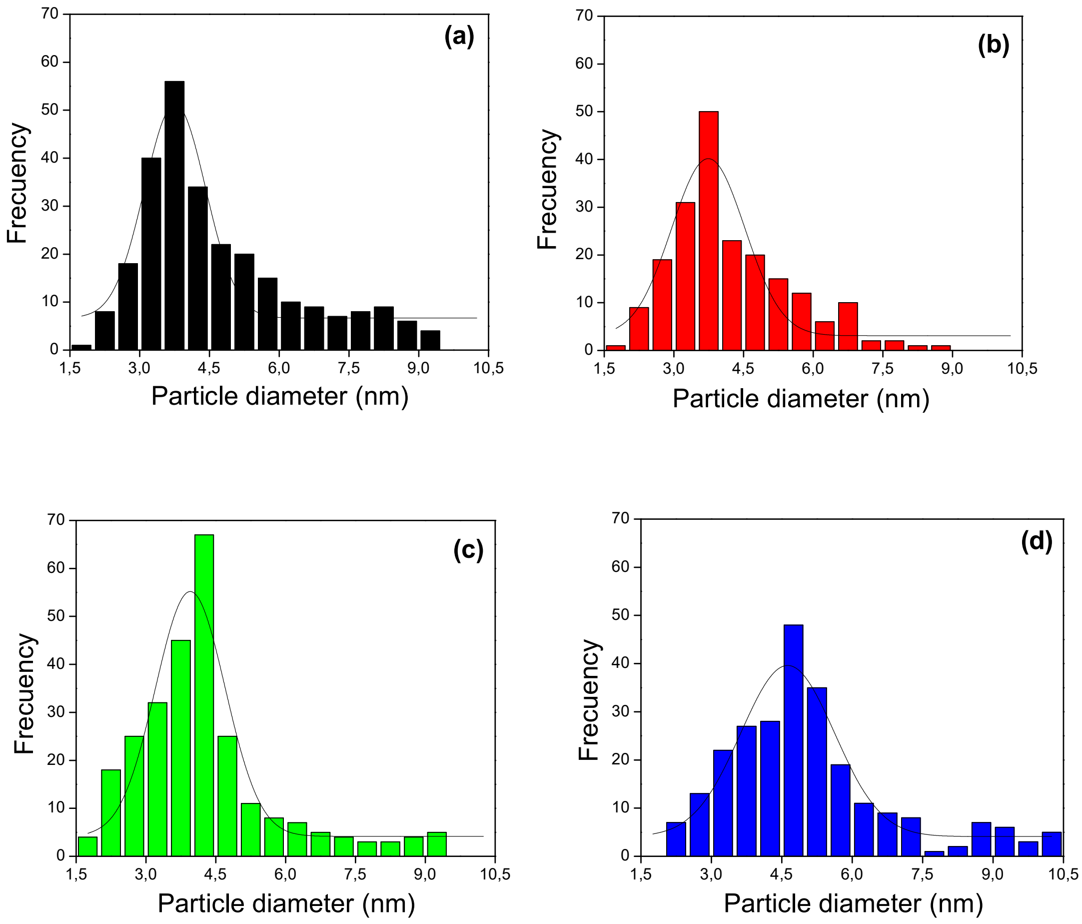

Figure 4.18 TEM particle size distributions for Ni/Al_2O_3 catalysts with varying Ni loading of (a)Ni(5), (b) Ni(6), (c) Ni(8), and (d) Ni(10).

4.3.4 Activity and selectivity of Ni loading on alumina support

Figure 4.19 shows the conversion of guaiacol and the products formed as a function of time with varying Ni loadings. In this figure we observed that the main products were cyclohexane, phenol, and methanol, while secondary products were cyclohexanol, cyclohexanone, methylcyclohexane and benzene. The product distribution does not have significant variations, suggesting that the nickel loadings on alumina do not modify the active sites present. Cyclohexane was produced as the major compound in all nickel loadings. Phenol increased and then decreased with time in all the catalysts, suggesting that that is an intermediate.

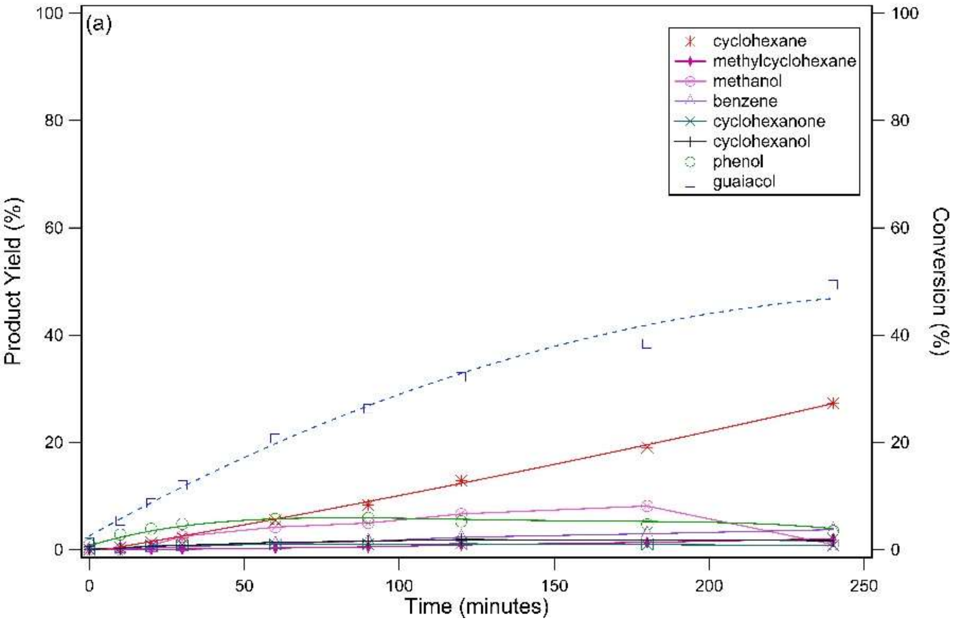

Figure 4.19. Conversion of guaiacol over (a)Ni(5)/Al_2O_3, (b)Ni(6)/Al_2O_3, (c) Ni(8)/Al_2O_3, (d)Ni(10)/Al_2O_3, (e)Ni(13)/Al_2O_3, (f)Ni(17)/Al_2O_3.

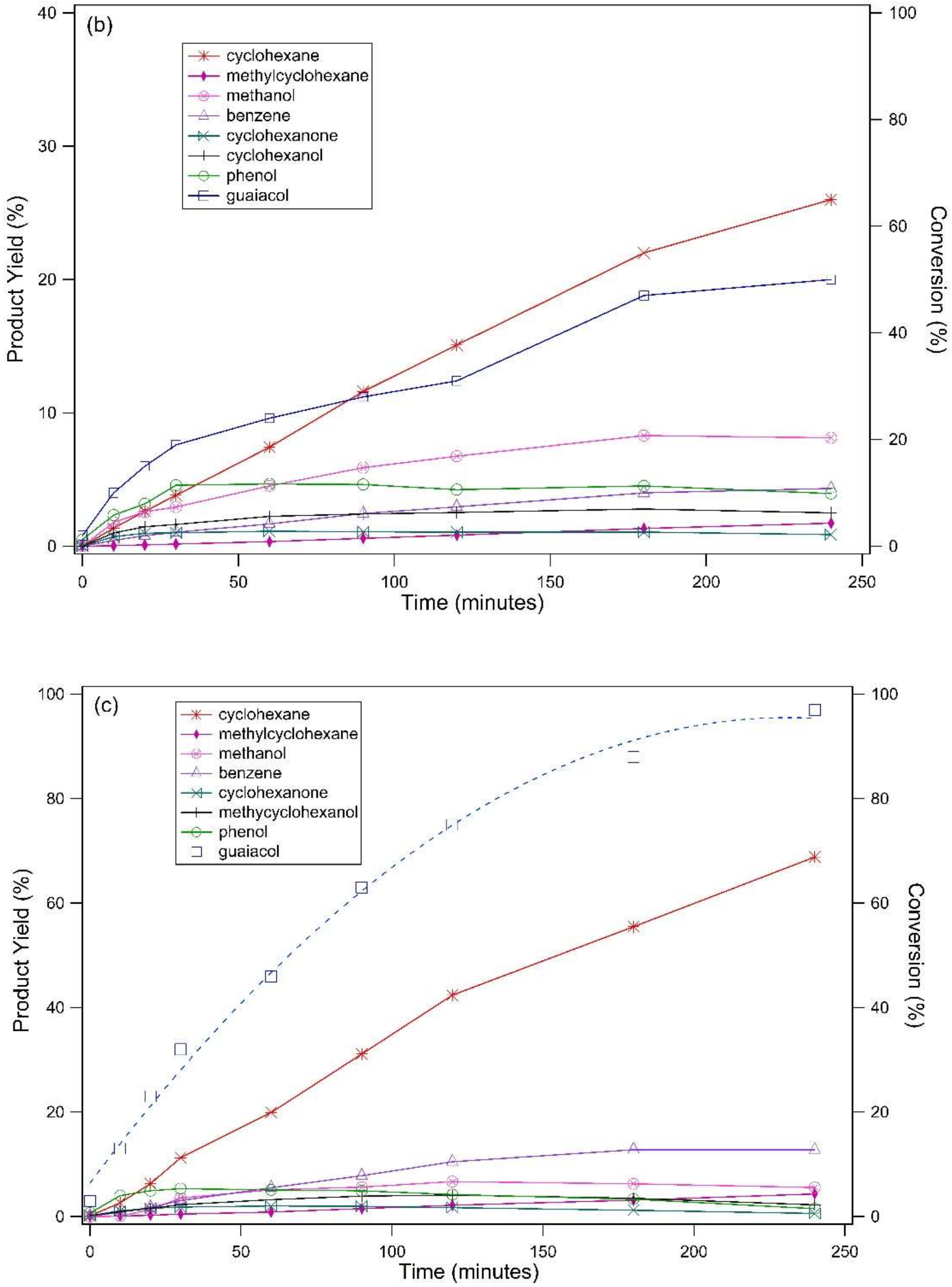

Figure 4.19. Continued

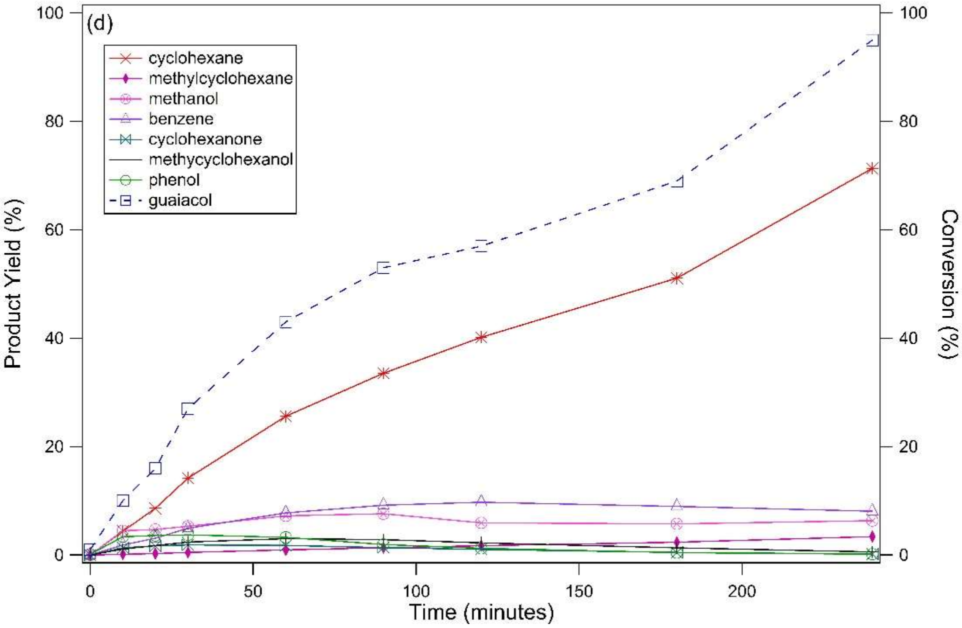

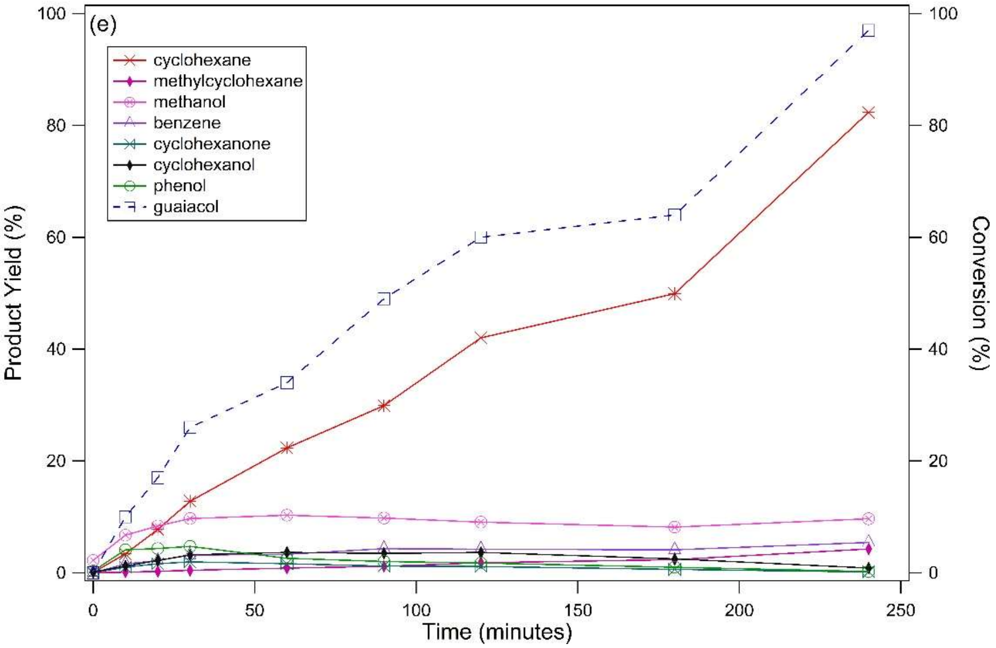

Figure 4.19. Continued.

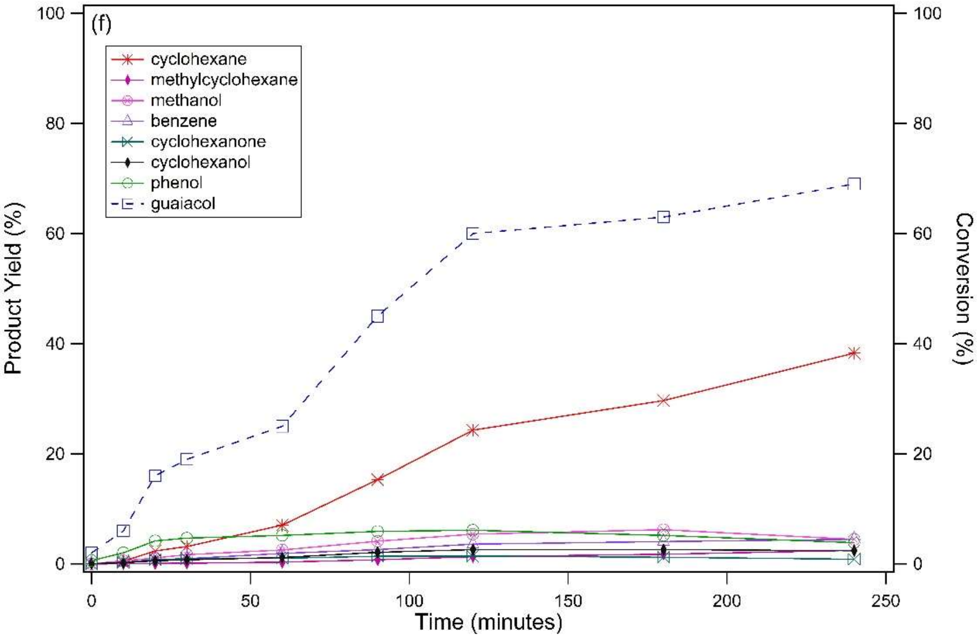

Figure 4.19. Continued.

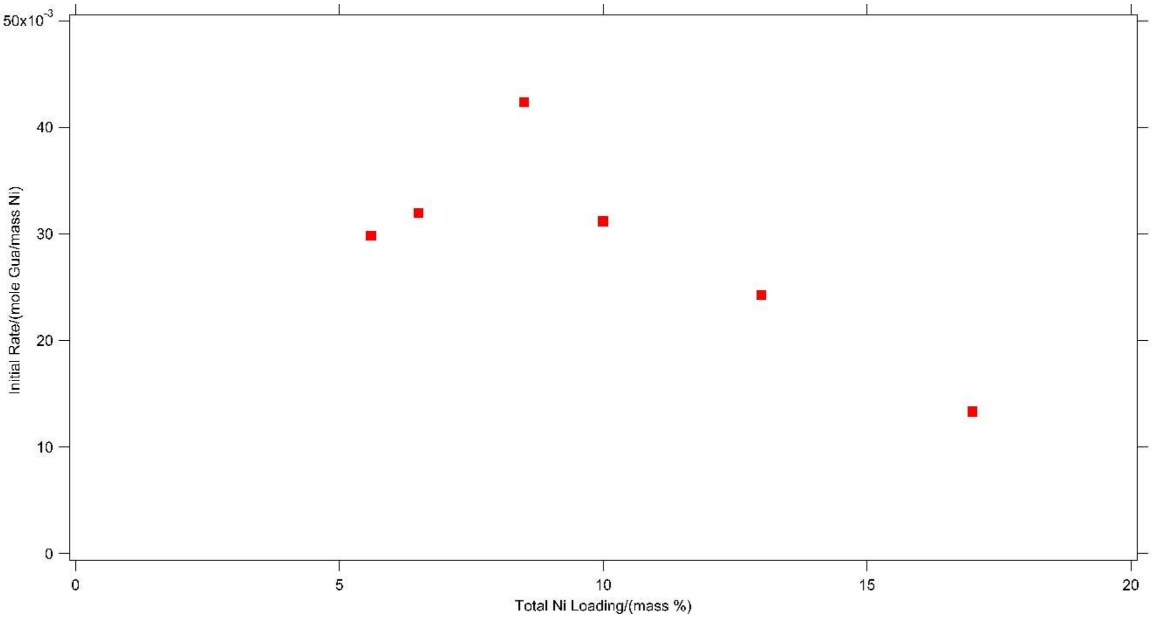

Figure 4.20. Initial reaction rate of guaiacol on different loadings of Ni/Al_2O_3.

The results of catalytic activity obtained in the guaiacol conversion with different metal content of Ni/A_2O_3 are shown in Figure 4.20. In this figure it is observed that the catalytic activity increased initially with nickel content until it reached a maximum at 8.5%Ni, but at higher nickel content the catalytic activity decreased. The increase in catalytic activity up to 8.5 %wt of Ni is related to the formation of well dispersed Ni species on the surface of the catalyst, that generates an increase in active sites during the reaction, as shown with TEM and CO chemisorption data, where the particle size measured was 4 and 15 nm respectively. The loss of catalytic activity reported above 10 %wt is attributed to the formation of Ni aggregates, which suggests a decrease in the number of actives sites on the catalyst when the Ni loading goes above 10 %wt. When the nickel content was below 10 %wt the peaks of the oxides observed on the XRD were almost undetectable, suggesting a smaller particle size, hence a better dispersion. Loss in dispersion above 10 %wt nickel was observed by CO chemisorption data. In addition, XRD showed an increase in the NiO particle size, since the peaks of the oxide can be observed at higher nickel content.

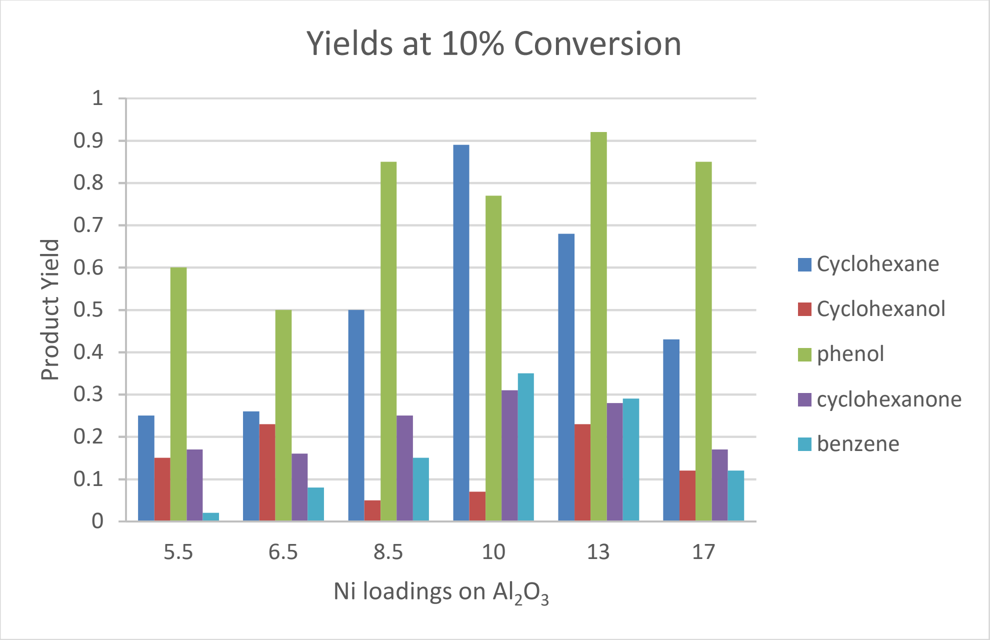

Figure 4.21. Selectivities at 10% conversion for each nickel loading.

In Figure 4.21, we showed that the amount of cyclohexane produced at 10% conversion reaches a maximum for Ni(10) and it decreased at higher content. No clear trend is observed for cyclohexanol, although the formation of this compound reached a minimum on Ni(8.5). The amount of phenol is more or less constant for nickel loadings above 8%, suggesting that actives sites do not change considerably at higher metal content.

The ratio of (cyclohexane+cyclohexene)/(cyclohexanol+cyclohexanone) was also calculated at 10% conversion for all nickel loadings and compared to the nickel on silica and silica-alumina catalysts, as shown in Figure 4.22.

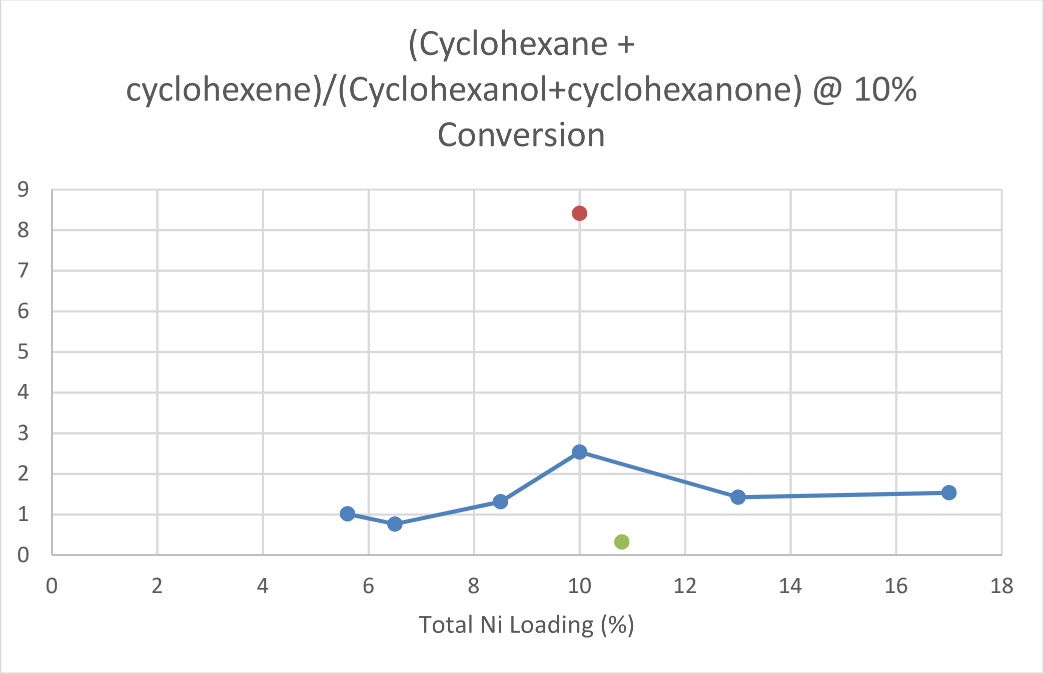

Figure 4.22. Selectivity (cyclohexane+cyclohexene)/cyclohexanol+cyclohexanone) at 10% conversion vs. nickel loading at 10 % conversion for (blue) Ni/Al_2O_3, (green) Ni/SiO_2, and (red) Ni/ SiO_2- Al_2O_3.

The dehydration of cyclohexanol requires a Bronsted acid site, which explains the high selectivity of the silica-alumina supported catalyst, compared to the alumina and silica supported catalysts. We suggest that the change in selectivity with Ni loading on the alumina support is complicated by $NiAl_2O_4$ spinel formation, where the amount of acid sites on the alumina support decrease with Ni loading.

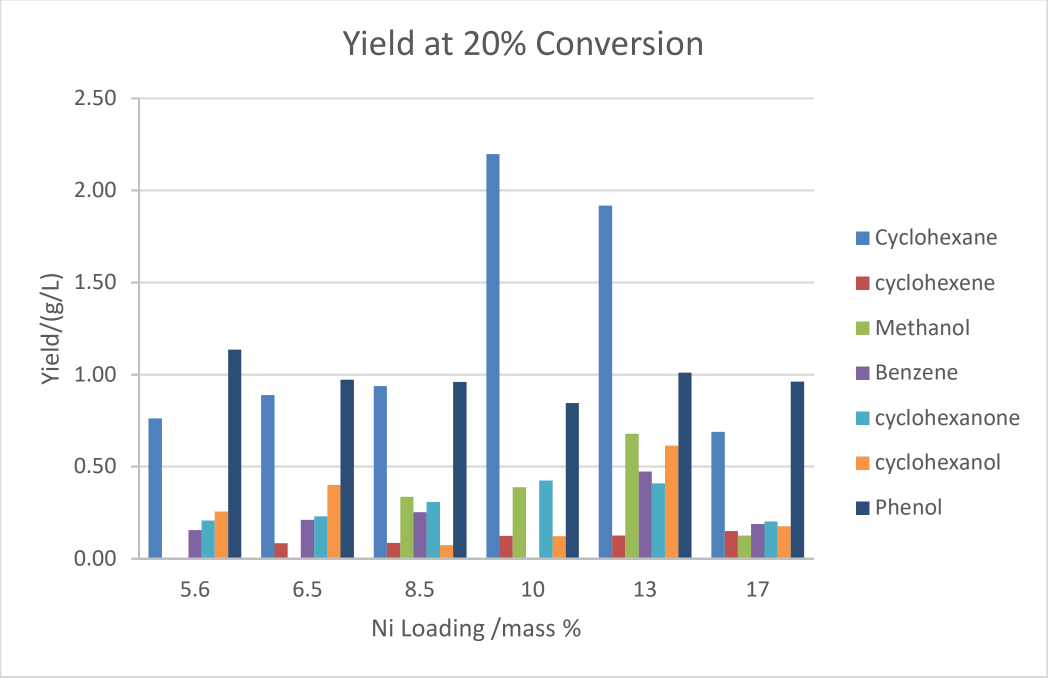

Figure 4.23. Product yields at 20% conversion for each Nickel loading.

Selectivities at 20% conversion are shown in Figure 4.23. The amount of cyclohexane is highest for catalysts with nickel loadings of 10 and 13%. Phenol seemed to remain constant for all Ni loadings suggesting that at 20% conversion the actives sites for DMO are the same. No clear trend was observed for cyclohexanol, similar to the behavior as observed at 10% conversion. The amount of phenol is constant for all nickel catalysts. The selectivity at 20% conversion, shown in Figure 4.24, is similar to the behavior at 10% conversion.

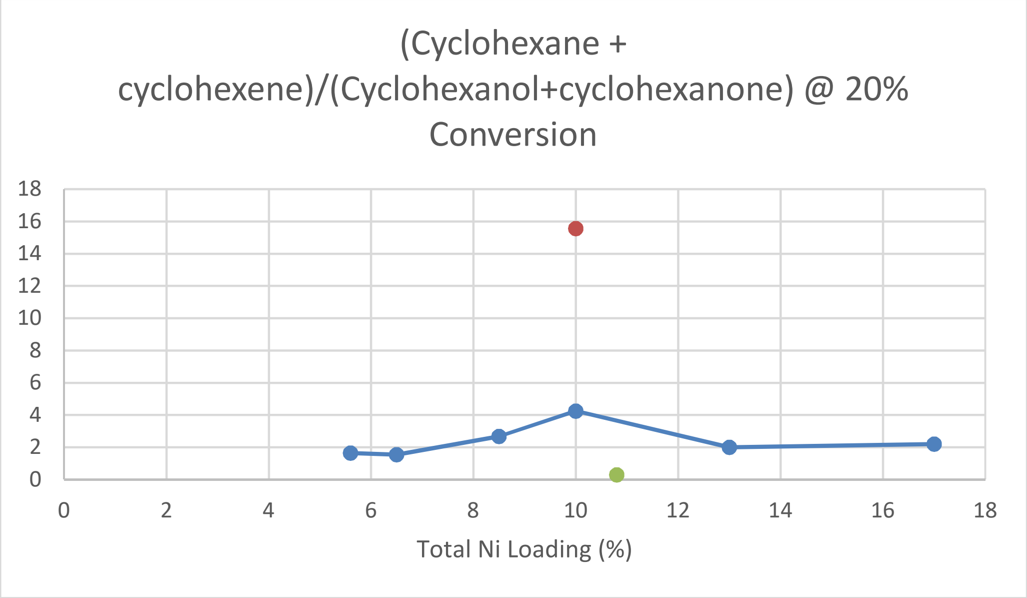

Figure 4.24. Selectivity (cyclohexane+cyxlohexene)/cyclohexanol+cyclohexanone) at 10% conversion vs. Nickel loading at 20 % conversion for (blue) Ni/Al_2O_3, (green) Ni/SiO_2, and (red) Ni/ SiO_2- Al_2O_3.

4.4 Conclusions

We prepared a series of Ni catalysts with different supports (Al_2O_3, SiO_2 and SiO_2-Al_2O_3) and compared their acidity and the effect on the guaiacol conversion. Ni/Al_2O_3 showed the highest activity, likely due to the better nickel-support interaction, higher dispersion and smaller particle size of this catalyst. The lowest catalytic activity was reported for Ni/SiO_2-Al_2O_3, likely due to the weaker interaction of the nickel with the support, as well as the larger particle size reported by TEM, and XRD. This correlation between activity and metal surface area shows that conversion of guaiacol to phenol, which is a demethoxylation reaction, occurs primarily on the metal functionality of the catalyst.

The main products observed were hydrogenated products such as cyclohexane, cyclohexanol, and methylcyclohexanol. The higher selectivity over the SiO_2-Al_2O_3 supported catalyst toward deoxygenated products, which are formed via dehydration of the alcohols at acid sites, clearly correlates with the greater acidity of the SiO_2-Al_2O_3 support compared to the SiO_2 and Al_2O_3 supports. At 10% conversion, phenol was the major product on Ni/SiO_2, which is due to the low acidity of this catalyst as shown by total acidity and ammonia TPD measurements.

CHAPTER 5

SUMMARY AND FUTURE DIRECTIONS

5.1 Conclusions

In this thesis we investigated the conversion of guaiacol as a representative molecule of bio-oil on unsupported tungsten oxide bronzes in a continuous flow fixed bed reactor and over supported nickel catalysts in a batch reactor. For both tungsten oxide bronzes and Ni-based catalysts the conversion of guaiacol, there are two paths that lead to deoxygenated products; hydrogenation of the aromatic ring and direct deoxygenation.

Although the hydrogenation reaction pathway for hydrodeoxygenation of guaiacol was originally determined experimentally over sulfide catalysts and is widely accepted for metal catalysts, there is no previous determination of the reaction pathways over reducible oxide surfaces. For the tungsten oxide bronze catalysts, by feeding the major product of each step in the reaction pathway over the catalyst we have confirmed that, in dodecane solution, guaiacol is first converted to phenol, then to cyclohexanol, cyclohexene, and finally cyclohexanol. In this sense, the reduced tungsten oxide bronze, H_xWO_{3-z}, behaves like noble metal catalysts, such as Pt, Pd, and Ru. The activity of the catalyst for conversion of guaiacol to phenol increased with the activation temperature used in formation of the reduced hydrogen tungsten oxide bronze, i.e. as z increases.

We have analyzed the activity under a variety of experimental conditions and developed a model that best represents how these catalysts transform our model compound. The reaction rate law is approximately first order in hydrogen pressure and zeroth order in guaiacol. A Langmuir-Hinshelwood-Hougan-Watson mechanism in which the methoxy C-O bond cleavage is the rate controlling step and guaiacol (and to some extent phenol) adsorb on the surface and block active sites, best describes the experimental data. Use of the model to estimate the apparent activation energy barrier from reactions at temperatures from 300 – 350 °C gives 89 kJ/mol, which is comparable to estimates of aromatic C-O bond strength.

For Ni-based catalysts, we compared the effects of loading and support acidity on guaiacol initial activity and selectivity toward deoxygenated products. The stronger interaction of Ni with alumina, compared to silica and silica-alumina supports, was evident from TEM, XRD, and CO chemisorption, leading to smaller particle sizes and so higher dispersion accounts for greater activity for the initial demethoxylation step. The phenol intermediate was converted to cyclohexanol via hydrogenation, also on the nickel surface. Deoxygenation of cyclohexanol to cyclohexene occurs by dehydration at acid sites, as shown by the strong increase in deoxygenation selectivity (at constant conversion and metal loading) on the acidic silica-alumina support.

5.2 Future work

Suggestions can be made to continue and improve this work. Experimental investigations should be continued to get more insight into the reaction mechanism involved. To improve the Mathcad models more data points would be necessary to have more accurate results. The data set of WO_3 bronzes should be extended by investigating the influence of flow rate (LHSV) at different guaiacol feed concentrations, as well as varying the hydrogen pressure under a wider range of concentration and liquid space velocities.

An understanding of the reaction mechanism at a molecular level could be improved through both experimental and theoretical methods. The zeroth order kinetics suggest that guaiacol is the most abundant surface intermediate, so measurements and calculations of the adsorption energy of guaiacol, phenol, and other species in the pathway would be valuable. The reduction of the surface is likely to affect the adsorption energy for both structural and electronic reasons. Is a single oxygen vacancy sufficient to bind guaiacol or is an ensemble of Lewis acid sites required? Comparison with the heats of adsorption on noble metal surfaces would provide perspective on the extent to which the bronze acts like a metal.

In-situ vibrational spectroscopy using a flow cell, for example with an ATR-IR cell, could be used to confirm whether guaiacol or phenol is predominant and how the coverage varies with reaction temperature.

The effect of water content it is also something important to consider for future investigation, since bio-oil is a complex mixture and contains about 30% wt. of water. In preliminary experiments using “liquified phenol”, which contains 10-11% water, we found high selectivity to benzene. The role of water in dramatically changing the selectivity of the reaction between the hydrogenation and direct deoxygenation (DDO) pathways if particularly interesting. We found a catalytic effect of water in the DDO of phenol over Ru/TiO_2 catalysts[129], which is not well understood. It is unknown how the composition and oxidation states of tungsten oxide bronzes or nickel-based catalysts behave when water is present during the course of the reaction.

Nickel-supported catalysts have shown to be effective by deoxygenating our model compound. However, the stability of this catalyst in a continuous flow reactor as well as its recyclability should be investigated.

REFERENCES

[1] U.S.E.I. Administration, Annual Energy Outlook 2015 with Projections to 2040, in: U.S.D.o. Energy (Ed.), Washington, DC, 2015.

[2] N. Armaroli, V. Balzani, The Future of Energy Supply: Challenges and Opportunities, Angewandte Chemie International Edition, 46 (2006) 52-66.

[3] J.L.A. Jan Ban, Roberto F Aguilera, Martin Tallett World Oil Outlook 2015, in, www.opec.org, 2015, pp. 406.

[4] OPEC, Annual Statistical Bulletin 50th Edition, in: Organization of the Petroleum Exporting Countries, OPEC.org, 2015, pp. 120.

[5] G.W. Huber, S. Iborra, A. Corma, Synthesis of Transportation Fuels from Biomass: Chemistry, Catalysts, and Engineering, Chemical Reviews, 106 (2006) 4044-4098.

[6] J.C. Hicks, Advances in CO bond transformations in ligninderived compounds for biofuels production, Journal of Physical Chemistry, 2 (2011) 2280-2287.

[7] C. Zhao, D.M. Camaioni, J.A. Lercher, J. Catal., 288 (2012) 92.

[8] M. Saidi, F. Samimi, D. Karimipourfard, T. Nimmanwudipong, B.C. Gates, M.R. Rahimpour, Upgrading of lignin-derived bio-oils by catalytic hydrodeoxygenation, Energy & Environmental Science, 7 (2014) 103-129.

[9] A.V. Bridgwater, D. Meier, D. Radlein, An overview of fast pyrolysis of biomass, Organic Geochemistry, 30 (1999) 1479-1493.

[10] J.D. Adjaye, N.N. Bakhshi, Fuel Process. Technol., 45 (1995) 185.

[11] Q. Zhang, J. Chang, T. Wang, Y. Xu, Review of biomass pyrolysis oil properties and upgrading research, Energy Conversion and Management, 48 (2007) 87-92.

[12] D.L. Klass, Biomass for Renewable Energy, Fuels, and Chemicals, 1998.

[13] A.V. Bridgwater, Renewable fuels and chemicals by thermal processing of biomass, Chemical Engineering Journal, 91 (2003) 87-102.

[14] A.V. Bridgwater, Advances in thermochemical biomass conversion, 1st ed., Blackie Academic & Professiona, London ; New York, 1994.

[15] D. Mohan, C.U. Pittman, P.H. Steele, Pyrolysis of Wood/Biomass for Bio-oil: A Critical Review, Energy & Fuels, 20 (2006) 848-889.

[16] A. Oasmaa, E. Kuoppala, A. Ardiyanti, R.H. Venderbosch, H.J. Heeres, Characterization of Hydrotreated Fast Pyrolysis Liquids, Energy & Fuels, 24 (2010) 5264-5272.

[17] A.V. Bridgwater, Production of high grade fuels and chemicals from catalytic pyrolysis of biomass, Catalysis Today, 29 (1996) 285-295.

[18] T. Bridgwater, Biomass for energy, Journal of the Science of Food and Agriculture, 86 (2006) 1755-1768.

[19] S. Yaman, Pyrolysis of biomass to produce fuels and chemical feedstocks, Energy Conversion and Management, 45 (2004) 651-671.

[20] A.V. Bridgwater, Production of high grade fuels and chemicals from catalytic pyrolysis of biomass, in, 1996, pp. 285-295.

[21] A.V. Bridgwater, S. Czernik, J.P. Diebold, D. Meier, A. Oasmaa, C. Peackocke, J. Piskorz, D. Radlein, Fast pyrolysis of biomass: A handbook CPL Press, Newbury Berkshire, 1999.

[22] S. Czernik, A. Bridgwater, Overview of applications of biomass fast pyrolysis oil, Energy & Fuels, 18 (2004) 590-598.

[23] D. Mohan, C.U. Pittman, P.H. Steele, Energy Fuels, 20 (2006) 848.

[24] J. Lédé, F. Broust, F.-T. Ndiaye, M. Ferrer, Properties of bio-oils produced by biomass fast pyrolysis in a cyclone reactor, Fuel, 86 (2007) 1800-1810.

[25] Z.W. Yao, A.J. Zhang, Y. Li, Y.Z. Zhang, X.Q. Cheng, C. Shi, An investigation of the thermal stability, crystal structure and catalytic properties of bulk and alumina-supported transition metal nitrides, Journal of Alloys and Compounds, 464 (2008) 488-496.

[26] M.J.G. J. B. Binder, J. F. White, Z. C. Zhang, J. E. Holladay, Biomass and Bioenergy, 33 (2009) 1122.

[27] W.J. DeSisto, N. Hill, S.H. Beis, S. Mukkamala, J. Joseph, C. Baker, T.-H. Ong, E.A. Stemmler, M.C. Wheeler, B.G. Frederick, A. van Heiningen, Fast Pyrolysis of Pine Sawdust in a Fluidized-Bed Reactor, Energy & Fuels, 24 (2010) 2642-2651.

[28] L. Ingram, D. Mohan, M. Bricka, P. Steele, D. Strobel, D. Crocker, B. Mitchell, J. Mohammad, K. Cantrell, C.U. Pittman, Pyrolysis of Wood and Bark in an Auger Reactor: Physical Properties and Chemical Analysis of the Produced Bio-oils, Energy & Fuels, 22 (2008) 614-625.

[29] J. Alvarez, G. Lopez, M. Amutio, J. Bilbao, M. Olazar, Bio-oil production from rice husk fast pyrolysis in a conical spouted bed reactor, Fuel, 128 (2014) 162-169.

[30] P.C. Badger, P. Fransham, Use of mobile fast pyrolysis plants to densify biomass and reduce biomass handling costs—A preliminary assessment, Biomass and Bioenergy, 30 (2006) 321-325.

[31] D.M. Alonso, S.G. Wettstein, J.A. Dumesic, Bimetallic catalysts for upgrading of biomass to fuels and chemicals, Chemical Society Reviews, 41 (2012) 8075-8098.

[32] A. Bridgwater, G. Peacocke, Fast pyrolysis processes for biomass, Renewable and Sustainable Energy Reviews, 4 (2000) 1-73.

[33] E. Furimsky, Catalytic hydrodeoxygenation, Applied Catalysis A: General, 199 (2000) 147-190.

[34] A.R. Ardiyanti, S.A. Khromova, R.H. Venderbosch, V.A. Yakovlev, H.J. Heeres, Catalytic hydrotreatment of fast-pyrolysis oil using non-sulfided bimetallic Ni-Cu catalysts on a δ-Al2O3 support, Applied Catalysis B: Environmental, 117–118 (2012) 105-117.

[35] S. Boullosa-Eiras, R. Lødeng, H. Bergem, M. Stöcker, L. Hannevold, E.A. Blekkan, Catalytic hydrodeoxygenation (HDO) of phenol over supported molybdenum carbide, nitride, phosphide and oxide catalysts, Catalysis Today, 223 (2014) 44-53.

[36] N. Joshi, A. Lawal, Hydrodeoxygenation of pyrolysis oil in a microreactor, Chemical Engineering Science, 74 (2012) 1-8.

[37] K. Pstrowska, J. Walendziewski, R. Łużny, M. Stolarski, Hydroprocessing of rapeseed pyrolysis bio-oil over NiMo/Al2O3 catalyst, Catalysis Today, 223 (2014) 54-65.

[38] H. Zuo, Q. Liu, T. Wang, L. Ma, Q. Zhang, Q. Zhang, Hydrodeoxygenation of Methyl Palmitate over Supported Ni Catalysts for Diesel-like Fuel Production, Energy & Fuels, 26 (2012) 3747-3755.

[39] X. Xu, C. Zhang, Y. Liu, Y. Zhai, R. Zhang, Two-step catalytic hydrodeoxygenation of fast pyrolysis oil to hydrocarbon liquid fuels, Chemosphere, 93 (2013) 652-660.

[40] E. Laurent, B. Delmon, Study of the hydrodeoxygenation of carbonyl, car□ylic and guaiacyl groups over sulfided CoMo/γ-Al2O3 and NiMo/γ-Al2O3 catalyst: II. Influence of water, ammonia and hydrogen sulfide, Applied Catalysis A: General, 109 (1994) 97-115.

[41] E. Laurent, B. Delmon, Study of the hydrodeoxygenation of carbonyl, car□ylic and guaiacyl groups over sulfided CoMo/γ-Al2O3 and NiMo/γ-Al2O3 catalysts: I. Catalytic reaction schemes, Applied Catalysis A: General, 109 (1994) 77-96.

[42] R. Maggi, B. Delmon, A review of catalytic hydrotreating processes for the upgrading of liquids produced by flash pyrolysis, in: B.D. G.F. Froment, P. Grange (Eds.) Studies in Surface Science and Catalysis, Elsevier, 1997, pp. 99-113.

[43] J.B.s. Bredenberg, M. Huuska, P. Toropainen, Hydrogenolysis of differently substituted methoxyphenols, Journal of Catalysis, 120 (1989) 401-408.

[44] P. Grange, E. Laurent, R. Maggi, A. Centeno, B. Delmon, Hydrotreatment of pyrolysis oils from biomass: reactivity of the various categories of oxygenated compounds and preliminary techno-economical study, Catalysis Today, 29 (1996) 297-301.

[45] A.V. Bridgwater, Review of fast pyrolysis of biomass and product upgrading, Biomass and Bioenergy, 38 (2012) 68-94.

[46] V.N. Bui, D. Laurenti, P. Afanasiev, C. Geantet, Hydrodeoxygenation of guaiacol with CoMo catalysts. Part I: Promoting effect of cobalt on HDO selectivity and activity, Applied Catalysis B: Environmental, 101 (2011) 239-245.

[47] V.N. Bui, D. Laurenti, P. Delichère, C. Geantet, Hydrodeoxygenation of guaiacol: Part II: Support effect for CoMoS catalysts on HDO activity and selectivity, Applied Catalysis B: Environmental, 101 (2011) 246-255.

[48] T.V. Choudhary, C.B. Phillips, Renewable fuels via catalytic hydrodeoxygenation, Applied Catalysis A: General, 397 (2011) 1-12.

[49] D.C. Elliott, D. Beckman, A.V. Bridgwater, J.P. Diebold, S.B. Gevert, Y. Solantausta, Developments in direct thermochemical liquefaction of biomass: 1983-1990, Energy & Fuels, 5 (1991) 399-410.

[50] K. Kwon, H. Mayfield, T. Marolla, B. Nichols, M. Mashburn, Renewable Energy, 36 (2011) 907.

[51] J. Wildschut, F.H. Mahfud, R.H. Venderbosch, H.J. Heeres, Hydrotreatment of Fast Pyrolysis Oil Using Heterogeneous Noble-Metal Catalysts, Industrial & Engineering Chemistry Research, 48 (2009) 10324-10334.

[52] S. Cheng, L. Wei, X. Zhao, J. Julson, Application, Deactivation, and Regeneration of Heterogeneous Catalysts in Bio-Oil Upgrading, Catalysts, 6 (2016) 195.

[53] K. Routray, K.J. Barnett, G.W. Huber, Hydrodeoxygenation of Pyrolysis Oils, Energy Technology, 5 (2017) 80-93.

[54] F. de Miguel Mercader, M.J. Groeneveld, S.R.A. Kersten, N.W.J. Way, C.J. Schaverien, J.A. Hogendoorn, Appl. Catal., B, 96 (2010) 57.

[55] A.V. Bridgwater, S. Czernik, J. Piskorz, in: A.V. Bridgwater (Ed.) Fast pyrolysis of biomass: A handbook, Antony Rowe Ltd., Chippenham, UK, 2002, pp. 1-22.

[56] A.L. N. Joshi, Chem. Eng. Science, 74 (2012) 1.

[57] Z. He, X. Wang, Hydrodeoxygenation of model compounds and catalytic systems for pyrolysis bio-oils upgrading, in: Catalysis for Sustainable Energy, 2012, pp. 28.

[58] S. Boonyasuwat, T. Omotoso, D.E. Resasco, S.P. Crossley, Conversion of Guaiacol over Supported Ru Catalysts, Catalysis Letters, 143 (2013) 783-791.

[59] M.V. Bykova, D.Y. Ermakov, S.A. Khromova, A.A. Smirnov, M.Y. Lebedev, V.A. Yakovlev, Stabilized Ni-based catalysts for bio-oil hydrotreatment: Reactivity studies using guaiacol, Catalysis Today, 220–222 (2014) 21-31.

[60] M.-Y. Chen, Y.-B. Huang, H. Pang, X.-X. Liu, Y. Fu, Hydrodeoxygenation of lignin-derived phenols into alkanes over carbon nanotube supported Ru catalysts in biphasic systems, Green Chemistry, (2015).

[61] W. Chen, Z.Y. Luo, C.J. Yu, Y. Yang, G.X. Li, J.X. Zhang, Catalytic conversion of guaiacol in ethanol for bio-oil upgrading to stable oxygenated organics, Fuel Processing Technology, 126 (2014) 420-428.

[62] B. Güvenatam, O. Kurşun, E.H.J. Heeres, E.A. Pidko, E.J.M. Hensen, Hydrodeoxygenation of mono- and dimeric lignin model compounds on noble metal catalysts, Catalysis Today, 233 (2014) 83-91.

[63] Y.-K. Hong, D.-W. Lee, H.-J. Eom, K.-Y. Lee, The catalytic activity of Pd/WOx/γ-Al2O3 for hydrodeoxygenation of guaiacol, Applied Catalysis B: Environmental, 150–151 (2014) 438-445.

[64] E. Laurent, B. Delmon, Study of the hydrodeoxygenation of carbonyl, carboxylic acid and guaiacyl groups over sulfided CoMo/gamma-Al_2O_3 and NiMo/gamma-Al_2O_3 catalyst. 2. Influence of water, amonia and hydrogen sulfide. , Applied Catalysis a-General, 109 (1994) 97-115.

[65] K. Leiva, C. Sepúlveda, R. García, J.L.G. Fierro, G. Aguila, P. Baeza, M. Villarroel, N. Escalona, Effect of P content in the conversion of guaiacol over Mo/γ-Al2O3 catalysts, Applied Catalysis A: General, 467 (2013) 568-574.

[66] J.-S. Moon, E.-G. Kim, Y.-K. Lee, Active sites of Ni2P/SiO2 catalyst for hydrodeoxygenation of guaiacol: A joint XAFS and DFT study, Journal of Catalysis, 311 (2014) 144-152.

[67] T. Nimmanwudipong, R.C. Runnebaum, D.E. Block, B.C. Gates, Catalytic Conversion of Guaiacol Catalyzed by Platinum Supported on Alumina: Reaction Network Including Hydrodeoxygenation Reactions, Energy & Fuels, 25 (2011) 3417-3427.

[68] A.V. Bridgwater, Catalysis in thermal biomass conversion, Applied Catalysis a-General, 116 (1994) 5-47.

[69] J.B. Bredenberg, M. Huuska, P. Toropainen, Hydrogenolysis of differently substituted methoxyphenols, Journal of Catalysis, 120 (1989) 401-408.

[70] C. Sepúlveda, K. Leiva, R. García, L.R. Radovic, I.T. Ghampson, W.J. DeSisto, J.L.G. Fierro, N. Escalona, Hydrodeoxygenation of 2-methoxyphenol over Mo2N catalysts supported on activated carbons, Catalysis Today, 172 (2011) 232-239.

[71] C.R. Lee, J.S. Yoon, Y.-W. Suh, J.-W. Choi, J.-M. Ha, D.J. Suh, Y.-K. Park, Catalytic roles of metals and supports on hydrodeoxygenation of lignin monomer guaiacol, Catalysis Communications, 17 (2012) 54-58.

[72] M.V. Bykova, D.Y. Ermakov, V.V. Kaichev, O.A. Bulavchenko, A.A. Saraev, M.Y. Lebedev, V.A. Yakovlev, Ni-based sol–gel catalysts as promising systems for crude bio-oil upgrading: Guaiacol hydrodeoxygenation study, Applied Catalysis B: Environmental, 113–114 (2012) 296-307.

[73] I.T. Ghampson, C. Sepulveda, R. Garcia, L.R. Radovic, J.L.G. Fierro, W.J. DeSisto, N. Escalona, Hydrodeoxygenation of guaiacol over carbon-supported molybdenum nitride catalysts: Effects of nitriding methods and support properties, Applied Catalysis A: General, 439-440 (2012) 111-124.

[74] P.E. Ruiz, B.G. Frederick, W.J. De Sisto, R.N. Austin, L.R. Radovic, K. Leiva, R. García, N. Escalona, M.C. Wheeler, Guaiacol hydrodeoxygenation on MoS2 catalysts: Influence of activated carbon supports, Catalysis Communications, 27 (2012) 44-48.

[75] P.E. Ruiz, K. Leiva, R. Garcia, P. Reyes, J.L.G. Fierro, N. Escalona, Relevance of sulfiding pretreatment on the performance of Re/ZrO2 and Re/ZrO2-sulfated catalysts for the hydrodeoxygenation of guayacol, Applied Catalysis A: General, 384 (2010) 78-83.

[76] C. Sepúlveda, N. Escalona, R. García, D. Laurenti, M. Vrinat, Hydrodeoxygenation and hydrodesulfurization co-processing over ReS2 supported catalysts, Catalysis Today, 195 (2012) 101-105.

[77] P.M. Mortensen, J.D. Grunwaldt, P.A. Jensen, K.G. Knudsen, A.D. Jensen, A review of catalytic upgrading of bio-oil to engine fuels, Applied Catalysis A: General, 407 (2011) 1-19.

[78] H. Topsoe, B.S. Clausen, F.E. Massoth, Hydrotreating Catalysis. Science and Technology, 1996.

[79] E. Furimsky, F.E. Massoth, Deactivation of hydroprocessing catalysts, Catalysis Today, 52 (1999) 381-495.

[80] C. Sepulveda, R. Garcia, N. Escalona, D. Laurenti, L. Massin, M. Vrinat, Unexpected Support Effect in Hydrotreating: Evidence of a Metallic Character for ReS<sub>2</sub>/Al<sub>2</sub>O<sub>3</sub> and ReS<sub>2</sub>/SiO<sub>2</sub> Catalysts, Catalysis Letters, 141 (2011) 987-995.

[81] M. Ferrari, R. Maggi, B. Delmon, P. Grange, Influences of the Hydrogen Sulfide Partial Pressure and of a Nitrogen Compound on the Hydrodeoxygenation Activity of a CoMo/Carbon Catalyst, Journal of Catalysis, 198 (2001) 47-55.

[82] A. Centeno, E. Laurent, B. Delmon, Influence of the Support of CoMo Sulfide Catalysts and of the Addition of Potassium and Platinum on the Catalytic Performances for the Hydrodeoxygenation of Carbonyl, Carboxyl, and Guaiacol-Type Molecules, Journal of Catalysis, 154 (1995) 288-298.

[83] G. de la Puente, A. Gil, J.J. Pis, P. Grange, Effects of Support Surface Chemistry in Hydrodeoxygenation Reactions over CoMo/Activated Carbon Sulfided Catalysts, Langmuir, 15 (1999) 5800-5806.

[84] A. Gutierrez, R.K. Kaila, M.L. Honkela, R. Slioor, A.O.I. Krause, Hydrodeoxygenation of guaiacol on noble metal catalysts, Catalysis Today, 147 (2009) 239-246.

[85] T. Nimmanwudipong, R. Runnebaum, D. Block, B. Gates, Catalytic Reactions of Guaiacol: Reaction Network and Evidence of Oxygen Removal in Reactions with Hydrogen, Catalysis Letters, 141 (2011) 779-783.

[86] R.N. Olcese, M. Bettahar, D. Petitjean, B. Malaman, F. Giovanella, A. Dufour, Gas-phase hydrodeoxygenation of guaiacol over Fe/SiO2 catalyst, Applied Catalysis B: Environmental, 115-116 (2012) 63-73.

[87] Y.-C. Lin, C.-L. Li, H.-P. Wan, H.-T. Lee, C.-F. Liu, Catalytic Hydrodeoxygenation of Guaiacol on Rh-Based and Sulfided CoMo and NiMo Catalysts, Energy & Fuels, 25 (2011) 890-896.

[88] R.C. Runnebaum, T. Nimmanwudipong, D.E. Block, B.C. Gates, Catal. Sci. Technol., 2 (2012) 113.

[89] M.Á. González-Borja, D.E. Resasco, Anisole and Guaiacol Hydrodeoxygenation over Monolithic Pt–Sn Catalysts, Energy & Fuels, 25 (2011) 4155-4162.

[90] H.Y. Zhao, D. Li, P. Bui, S.T. Oyama, Hydrodeoxygenation of guaiacol as model compound for pyrolysis oil on transition metal phosphide hydroprocessing catalysts, Applied Catalysis A: General, 391 (2011) 305-310.

[91] H. Wang, J. Male, Y. Wang, Recent Advances in Hydrotreating of Pyrolysis Bio-Oil and Its Oxygen-Containing Model Compounds, ACS Catalysis, 3 (2013) 1047-1070.

[92] I.T. Ghampson, C. Sepúlveda, R. Garcia, B.G. Frederick, M.C. Wheeler, N. Escalona, W.J. DeSisto, Guaiacol transformation over unsupported molybdenum-based nitride catalysts, Applied Catalysis A: General, 413–414 (2012) 78-84.

[93] A.L. Jongerius, R.W. Gosselink, J. Dijkstra, J.H. Bitter, P.C.A. Bruijnincx, B.M. Weckhuysen, Carbon Nanofiber Supported Transition-Metal Carbide Catalysts for the Hydrodeoxygenation of Guaiacol, ChemCatChem, 5 (2013) 2964-2972.

[94] T. Mochizuki, S.-Y. Chen, M. Toba, Y. Yoshimura, Deoxygenation of guaiacol and woody tar over reduced catalysts, Applied Catalysis B: Environmental, 146 (2014) 237-243.

[95] P.M. Mortensen, J.-D. Grunwaldt, P.A. Jensen, A.D. Jensen, Screening of Catalysts for Hydrodeoxygenation of Phenol as a Model Compound for Bio-oil, ACS Catalysis, 3 (2013) 1774-1785.

[96] V.A. Yakovlev, S.A. Khromova, O.V. Sherstyuk, V.O. Dundich, D.Y. Ermakov, V.M. Novopashina, M.Y. Lebedev, O. Bulavchenko, V.N. Parmon, Development of new catalytic systems for upgraded bio-fuels production from bio-crude-oil and biodiesel, Catalysis Today, 144 (2009) 362-366.

[97] S. Echeandia, P.L. Arias, V.L. Barrio, B. Pawelec, J.L.G. Fierro, Synergy effect in the HDO of phenol over Ni–W catalysts supported on active carbon: Effect of tungsten precursors, Applied Catalysis B: Environmental, 101 (2010) 1-12.

[98] S. Jin, Z. Xiao, C. Li, X. Chen, L. Wang, J. Xing, W. Li, C. Liang, Catalytic hydrodeoxygenation of anisole as lignin model compound over supported nickel catalysts, Catalysis Today, 234 (2014) 125-132.

[99] C. Perego, S. Amarilli, A. Carati, C. Flego, G. Pazzuconi, C. Rizzo, G. Bellussi, Mesoporous silica-aluminas as catalysts for the alkylation of aromatic hydrocarbons with olefins, Microporous and Mesoporous Materials, 27 (1999) 345-354.

[100] T. Itoh, T. Uchida, I. Matsubara, N. Izu, W. Shin, H. Miyazaki, H. Tanjo, K. Kanda, Preparation of γ-alumina large grain particles with large specific surface area via polyol synthesis, Ceramics International, 41 (2015) 3631-3638.

[101] C. Morterra, G. Magnacca, A case study: surface chemistry and surface structure of catalytic aluminas, as studied by vibrational spectroscopy of adsorbed species, Catalysis Today, 27 (1996) 497-532.

[102] M. Trueba, S.P. Trasatti, γ-Alumina as a Support for Catalysts: A Review of Fundamental Aspects, European Journal of Inorganic Chemistry, 2005 (2005) 3393-3403.

[103] S.-D. Mo, Y.-N. Xu, W.-Y. Ching, Electronic and Structural Properties of Bulk γ-Al2O3, Journal of the American Ceramic Society, 80 (1997) 1193-1197.

[104] J.W. Ward, Hydrocracking processes and catalysts, Fuel Processing Technology, 35 (1993) 55-85.

[105] J. Scherzer, A.J. Gruia, Hydrocracking science and technology, CRC Press, 1996.

[106] S. Peratello, M. Molinari, G. Bellussi, C. Perego, Olefins oligomerization: thermodynamics and kinetics over a mesoporous silica–alumina, Catalysis Today, 52 (1999) 271-277.

[107] Y. Ohtsuka, T. Arai, S. Takasaki, N. Tsubouchi, Fischer-Tropsch synthesis with cobalt catalysts supported on mesoporous silica for efficient production of diesel fuel fraction, Energy & Fuels, 17 (2003) 804-809.

[108] S.J. Gregg, K.S.W. Sing, Adsorption, Surface Area and Porosity, Academic Press, London, 1982.

[109] K.S.W. Sing, D.H. Everett, R.A.W. Haul, L. Moscou, R.A. Pierotti, J. Rouquerol, T. Siemieniewska, Reporting physisorption data for gas solid systems with special reference to the determination of surface-area and porosity (recommendations 1984), Pure and Applied Chemistry, 57 (1985) 603-619.

[110] S. Lowell, J.E. Shields, M.A. Thomas, M. Thommes, Characterization of porous solids and powders: surface area, pore size and density, Kluwer Academic Publishers, Boston, 2004.

[111] S. Brunauer, P.H. Emmett, E. Teller, Adsorption of gases in multimolecular layers, Journal of the American Chemical Society, 60 (1938) 309-319.

[112] C. Hammond, The Basics of Crystallography and Diffraction, Oxford University Press, Oxford, 1997.

[113] R. Richards, Surface and Nanomolecular Catalysis, in: Characterization of Heterogeneous Catalysis, Taylor & Francis Group, New York, 2006.

[114] B. Fultz, J.M. Howe, Transmission Electron Microscopy and Diffractometry of Materials, 2nd ed., Springer-Verlag, Berlin **2002**.

[115] D4824-03: Standard test method for determination of catalyst acidity by ammonia chemisorption, in, ASTM International, Pennsylvania, US, **(2008)**.

[116] H.A. Benesi, Acidity of Catalyst Surfaces. I. Acid Strength from Colors of Adsorbed Indicators, Journal of the American Chemical Society, 78 (1956) 5490-5494.

[117] S.Z. Chen, S.X. Bao, Determination of total acidity of solid catalyst by pyridine-thermobalance method, Fenxi Shiyanshi, 15 (1996) 87-90.

[118] R. Cid, G. Pecchi, Potentiometric Method for Determining the Number and Relative Strength of Acid Sites in Colored Catalysts, Applied Catalysis, 14 (1985) 15-21.

[119] A.M. Venezia, X-ray photoelectron spectroscopy (XPS) for catalysts characterization, Catalysis Today, 77 (2003) 359-370.

[120] C.D. Wagner, L.E. Davis, M.V. Zeller, J.A. Taylor, R.H. Raymond, L.H. Gale, Empirical atomic sensitivity factors for quantitative analysis by electron spectroscopy for chemical analysis, Surface and Interface Analysis, 3 (1981) 211-225.

[121] B. Pawelec, R. Mariscal, J. Fierro, A. Greenwood, P. Vasudevan, Carbon-supported tungsten and nickel catalysts for hydrodesulfurization and hydrogenation reactions, Applied Catalysis A: General, 206 (2001) 295-307.

[122] J. Cruz, M. Avalos-Borja, R. López Cordero, M.A. Bañares, J.L.G. Fierro, J.M. Palacios, A. López Agudo, Influence of pH of the impregnation solution on the phosphorus promotion in W/Al2O3 hydrotreating catalysts, Applied Catalysis A: General, 224 (2002) 97-110.

[123] C. Hoang-Van, O. Zegaoui, Studies of high surface area Pt/MoO3 and Pt/WO3 catalysts for selective hydrogenation reactions. II. Reactions of acrolein and allyl alcohol, Applied Catalysis A: General, 164 (1997) 91-103.

[124] T.J. Thibodeau, A.S. Canney, W.J. DeSisto, M.C. Wheeler, F.G. Amar, B.G. Frederick, Composition of tungsten oxide bronzes active for hydrodeoxygenation, Applied Catalysis A: General, 388 (2010) 86-95.

[125] T.J. Thibodeau, A.S. Canney, W.J. DeSisto, M.C. Wheeler, F.G. Amar, B.G. Frederick, Composition of Tungsten Oxide Bronzes Active for Hydrodeoxygenation, Applied Catalysis A: General, 388 (2010) 86-95.

[126] Y.Q. Yang, C.T. Tye, K.J. Smith, Influence of MoS2 catalyst morphology on the hydrodeoxygenation of phenols, Catalysis Communications, 9 (2008) 1364-1368.

[127] O.İ. Şenol, E.M. Ryymin, T.R. Viljava, A.O.I. Krause, Effect of hydrogen sulphide on the hydrodeoxygenation of aromatic and aliphatic oxygenates on sulphided catalysts, Journal of Molecular Catalysis A: Chemical, 277 (2007) 107-112.

[128] C. Newman, X. Zhou, B. Goundie, I.T. Ghampson, R.A. Pollock, Z. Ross, M.C. Wheeler, R.W. Meulenberg, R.N. Austin, B.G. Frederick, Effects of support identity and metal dispersion in supported ruthenium hydrodeoxygenation catalysts, Applied Catalysis A: General, 477 (2014) 64-74.

[129] R.C. Nelson, B. Baek, P. Ruiz, B. Goundie, A. Brooks, M.C. Wheeler, B.G. Frederick, L.C. Grabow, R.N. Austin, Experimental and Theoretical Insights into the Hydrogen-Efficient Direct Hydrodeoxygenation Mechanism of Phenol over Ru/TiO_2, ACS Catal., 5 (2015) 6509-6523.

[130] T. Nimmanwudipong, R.C. Runnebaum, D.E. Block, B.C. Gates, Energy Fuels, 25 (2011) 3417.

[131] M. Ferrari, S. Bosmans, R. Maggi, B. Delmon, P. Grange, CoMo/carbon hydrodeoxygenation catalysts: influence of the hydrogen sulfide partial pressure and of the sulfidation temperature, Catalysis Today, 65 (2001) 257-264.

[132] T. Nimmanwudipong, R. Runnebaum, D. Block, B. Gates, Catal. Lett., 141 (2011) 779.

[133] S.P. Zhang, Y.J. Yan, J.W. Ren, T.C. Li, Study of hydrodeoxygenation of bio-oil from the fast pyrolysis of biomass, Energy Sources, 25 (2003) 57-65.

[134] S. Sitthisa, T. Sooknoi, Y. Ma, P.B. Balbuena, D.E. Resasco, Kinetics and mechanism of hydrogenation of furfural on Cu/SiO2 catalysts, Journal of Catalysis, 277 (2011) 1-13.

[135] K. Leiva, N. Martinez, C. Sepulveda, R. García, C.A. Jiménez, D. Laurenti, M. Vrinat, C. Geantet, J.L.G. Fierro, I.T. Ghampson, N. Escalona, Hydrodeoxygenation of 2-

methoxyphenol over different Re active phases supported on SiO2 catalysts, Applied Catalysis A: General, 490 (2015) 71-79.

[136] D.R. Moberg, T.J. Thibodeau, F.G. Amar, B.G. Frederick, Mechanism of Hydrodeoxygenation of Acrolein on a Cluster Model of MoO_3, The Journal of Physical Chemistry C, 114 (2010) 13782-13795.

[137] T.J. Thibodeau, Development and mechanisms of hydrodeoxygenation catalysts for upgrading pyrolysis oil, in: Chemistry, University of Maine, 2012.

[138] P. Kletting, G. Glatting, Model selection for time-activity curves: The corrected Akaike information criterion and the F-test, Zeitschrift für Medizinische Physik, 19 (2009) 200-206.

[139] H. Akaike, A new look at the statistical model identification, IEEE Transactions on Automatic Control, 19 (1974) 716-723.

[140] N. Rai, S. Caratzoulas, D.G. Vlachos, Role of Silanol Group in Sn-Beta Zeolite for Glucose Isomerization and Epimerization Reactions, ACS Catalysis, 3 (2013) 2294-2298.

[141] M.A. Vannice, Kinetics of Catalytic Reactions, Springer, New York, 2005.

[142] J.L. Ewbank, L. Kovarik, F.Z. Diallo, C. Sievers, Effect of metal–support interactions in Ni/Al2O3 catalysts with low metal loading for methane dry reforming, Applied Catalysis A: General, 494 (2015) 57-67.

[143] F. Rahbar Shamskar, M. Rezaei, F. Meshkani, The influence of Ni loading on the activity and coke formation of ultrasound-assisted co-precipitated Ni–Al2O3 nanocatalyst in dry reforming of methane, International Journal of Hydrogen Energy, 42 (2017) 4155-4164.

[144] S.G. Choi, S.-J. Wang, H.-H. Park, J.-N. Jang, M. Hong, K.-H. Kwon, H.-H. Park, Properties of amorphous silicon thin films synthesized by reactive particle beam assisted chemical vapor deposition, Thin Solid Films, 518 (2010) 7372-7376.

[145] D. Li, W.Y. Teoh, C. Selomulya, R.C. Woodward, R. Amal, B. Rosche, Flame-Sprayed Superparamagnetic Bare and Silica-Coated Maghemite Nanoparticles: Synthesis, Characterization, and Protein Adsorption−Desorption, Chemistry of Materials, 18 (2006) 6403-6413.

[146] W.K. Jozwiak, E. Szubiakiewicz, J. Góralski, A. Klonkowski, T. Paryjczak, Physico-Chemical and Catalytic Study of the Co/SiO2 Catalysts, Kinetics and Catalysis, 45 (2004) 247-255.

[147] V.V. Thyssen, T.A. Maia, E.M. Assaf, Cu and Ni Catalysts Supported on ^{3}-Al2O3 and SiO2 Assessed in Glycerol Steam Reforming Reaction, Journal of the Brazilian Chemical Society, 26 (2015) 22-31.

[148] J. Zieliński, Morphology of nickel/alumina catalysts, Journal of Catalysis, 76 (1982) 157-163.

[149] C. Guimon, A. Auroux, E. Romero, A. Monzon, Acetylene hydrogenation over Ni–Si–Al mixed oxides prepared by sol–gel technique, Applied Catalysis A: General, 251 (2003) 199-214.

[150] W. Cai, L. Ye, L. Zhang, Y. Ren, B. Yue, X. Chen, H. He, Highly Dispersed Nickel-Containing Mesoporous Silica with Superior Stability in Carbon Dioxide Reforming of Methane: The Effect of Anchoring, Materials, 7 (2014) 2340.

[151] R. Nava, J. Morales, G. Alonso, C. Ornelas, B. Pawelec, J.L.G. Fierro, Influence of the preparation method on the activity of phosphate-containing CoMo/HMS catalysts in deep hydrodesulphurization, Applied Catalysis A: General, 321 (2007) 58-70.

[152] S. Jin, Z. Xiao, C. Li, X. Chen, L. Wang, J. Xing, W. Li, C. Liang, Catalytic hydrodeoxygenation of anisole as lignin model compound over supported nickel catalysts, Catalysis Today, 234 (2014) 125-132.

[153] X. Zhu, L.L. Lobban, R.G. Mallinson, D.E. Resasco, Bifunctional transalkylation and hydrodeoxygenation of anisole over a Pt/HBeta catalyst, Journal of Catalysis, 281 (2011) 21-29.

[154] K. Shih, J.O. Leckie, Nickel aluminate spinel formation during sintering of simulated Ni-laden sludge and kaolinite, Journal of the European Ceramic Society, 27 (2007) 91-99.

Appendix A

Hydrodeoxygenation of Guaiacol Calculations

Calculations done for chapter 3-4 are illustrated in this section. They include calculations for conversion, reaction rates. The catalyst sample used for these illustrations is Ni(8)/Al_2O_3.

A.1. Calculation of Conversion of Guaiacol and Yield of Products

The conversion of guaiacol and the yield of products were calculated from changes in the peak areas of guaiacol and products in the GC spectrum using hexadecane as an internal standard. Table A.1 shows integrated areas of the reactants and products after 90 min of reaction.

Table A.1 Concentration of guaiacol

Mass of catalyst:	0.05	g
Guaiacol Conc in Feed:	0.23	Mol/L
	28.80	g/L

Table A.2 Calculated areas from GC spectrum

MW	**84.16**	**92.14**	**226.44**	**124.14**	**94.11**
Effective C#	**5.52**	**5.98**	**16**	**5.82**	**4.10**
		HDO			
	cyclohexane	**toluene**	**hexadecane**	**guaiacol**	**phenol**
Rxn time/min	**area**				
Before Rx			8373143.00	19646416.00	
90	4868263.00	113174.00	9599964.00	7313405.00	572017.00

Based on the integrated peak areas, the molecular weight of each reactant and product and the Effective carbon number for the FID. We calculated the concentration of phenol and cyclohexane as examples in g/L at time, 90min, was calculated as follows:

$$Phenol\ \left(\frac{g}{L}\right) = \frac{MW_{Phen}}{MW_{Guaiacol}} \times \frac{Eff_{carbon\ Gua}}{Eff_{carbon\ Phe}} \times \frac{Area\ Phenol_{time\ t}}{Area\ Gua_{before\ rx}} \times C_{gua\ (\frac{g}{L})}$$

$$Phenol\ \left(\frac{g}{L}\right) = \frac{94.11}{124.14} \times \frac{5.82}{4.1} \times \frac{572017}{19646416} \times 28.8\left(\frac{g}{L}\right) = 0.90g/L$$

$$Cyclohexane\ \left(\frac{g}{L}\right) = \frac{MW_{cyclohex}}{MW_{Guaiacol}} \times \frac{Eff_{carbon\ Gua}}{Eff_{carbon\ cyclohex}} \times \frac{Area\ Cyclohex_{90}}{Area\ Gua_{before\ rx}} \times C_{gua\ (\frac{g}{L})}$$

$$Cyclohexane\ \left(\frac{g}{L}\right) = \frac{84.16}{124.14} \times \frac{5.82}{5.52} \times \frac{4868263}{19446416} \times 28.8\left(\frac{g}{L}\right) = 5.10g/L$$

Once we calculated the all concentration for reactant and products formed the overall sum gives the total mass in g/L. the conversion of guaiacol was calculated as:

$$X(\%) = \frac{C_{guaiacol\_bef\ rx} - C_{guaiacol\_time\ t}}{C_{guaiacol\_bef\ rx}} \times 100\%$$

the product yield was calculated as:

$$Yield\ Phenol(\%) = \frac{Phenol(\frac{g}{L})}{Total\ mass(\frac{g}{L})} \times 100\%$$

A.2. Calculation of Reaction Rates

The reaction rate was calculated as:

$$Reaction\ Rates\left({}^{mol}/{}_{g_{catalyst}}\cdot s\right)=\frac{Initial\ Slope\cdot moles_{Guaiacol}}{M}$$

where $moles_{Guaiacol}$ is the moles of guaiacol in the reactant mixture, *M* is the mass of the catalyst and *Initial slope* is the slope from the conversion vs. reaction time plot (shown in Fig. A.2):

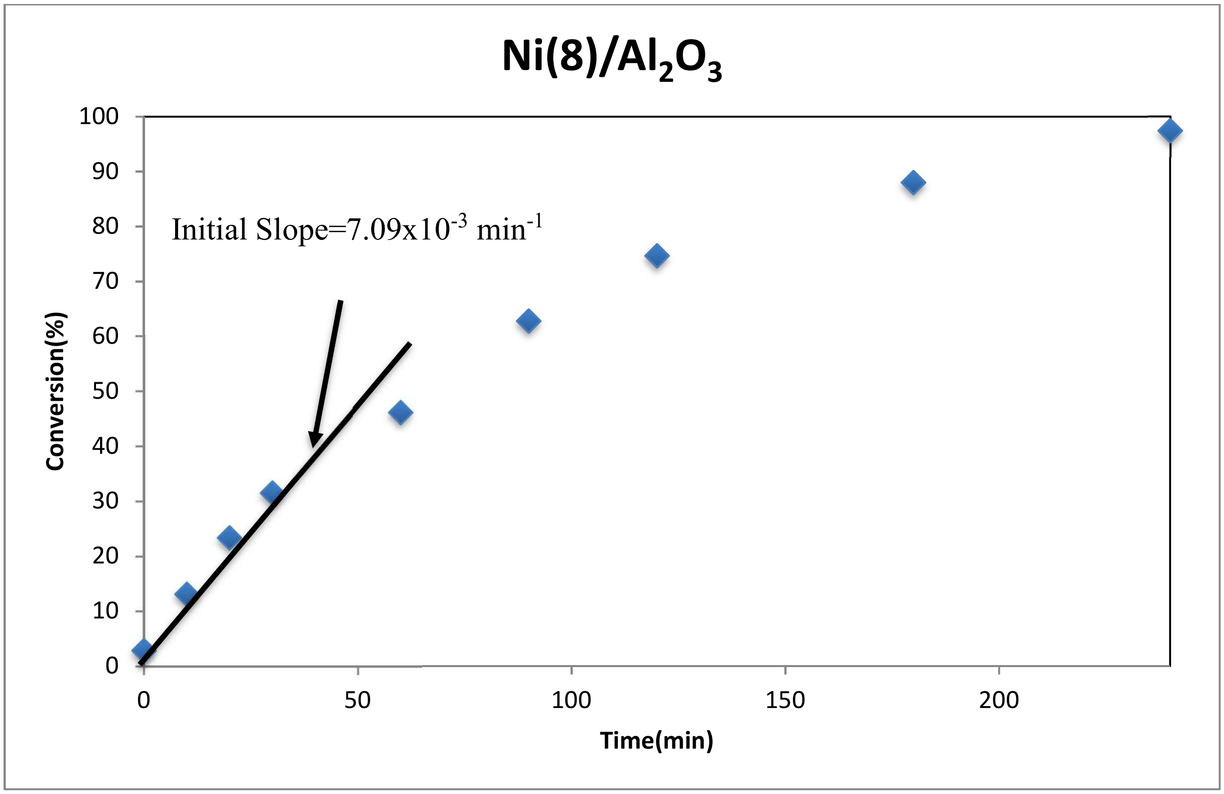

Figure A.2 Conversion of guaiacol and the formation of products versus time for Ni(8)/Al2O3 catalyst.

$$moles_{Guaiacol} = Conc_{Guaiacol} \cdot Vol_{Solvent}$$

$$moles = \left(0.232\, {}^{mol}/_{L}\right) \cdot (0.08L) = 0.0185m$$

$$Reaction\ Rates\left({}^{mol}/_{g_{catalyst}} \cdot s\right) = \frac{(7.09 \times 10^{-3} min^{-1}) \cdot (0.0185mol)}{0.05g}$$

Appendix B

Langmuir Hinshelwood Hougen Watson Models

LHHW Model 2

Rate limiting step addition of first H

$H_2 + \ \ 2* \overset{K_{H_2}}{\Longleftrightarrow} 2H*$ Equilibrium $[H*] = K_{H_2}{}^{1/2} P_{H_2}{}^{1/2}[*]$ (9)

$GUA + * \overset{K_{GUA}}{\Longleftrightarrow} GUA*$ Equilibrium $[GUA*] = K_{GUA}[GUA][*]$ (10)

$GUA* + H* \overset{k_3}{\rightarrow} GUAH*$ Rate Limiting Step (11)

Site Balance: same as Eq (4)

$$C_T = [*]\left\{1 + K_{GUA}[GUA] + \sqrt{K_{H_2}P_{H_2}}\right\} \qquad (6)$$

From reaction (11):

$$r_3 = k_3 K_{GUA}[GUA*][*] \qquad (12)$$

Substituting equation 6 and 10 in 12:

$$r_3 = k_3 K_{GUA}[GUA][*]\sqrt{K_{H_2}P_{H_2}}[*] \qquad (13)$$

$$r_3 = \frac{k_3 K_{GUA} C_T^2 [GUA]\sqrt{K_{H_2}P_{H_2}}}{\left\{1 + \ K_{GUA}[GUA] + \sqrt{K_{H_2}P_{H_2}}\ \right\}^2} \qquad (14)$$

LHHW Model 3

Rate limiting step addition of second Hydrogen

$H_2 + \ 2* \overset{K_{H_2}}{\Longleftrightarrow} 2H*$ Equilibrium $[H*] = K_{H_2}{}^{1/2} P_{H_2}{}^{1/2} [*]$ (15)

$GUA + * \overset{K_{GUA}}{\Longleftrightarrow} GUA*$ Equilibrium $[GUA*] = K_{GUA}[GUA][*]$ (16)

$GUA* + H* \overset{K_3}{\Longleftrightarrow} GUAH* + *$

$$[GUAH*] = \frac{K_3[GUAH*][H*]}{[*]} \qquad (17)$$

$GUAH* + H* \xrightarrow{k_4} PHE + MeOH + 3*$ (18) Rate Limiting Step

Site Balance

$$C_T = [H*] + [GUA*] + [GUAH*] + [*] \qquad (19)$$

Substituting equations 15, 16 and 17 in 19 gives:

$$C_T = [*] + K_{H_2}{}^{1/2} P_{H_2}{}^{1/2}[*] + K_{GUA}[GUA][*] + \frac{K_3[GUA*][H*]}{[*]}$$

$$C_T = [*] + K_{H_2}{}^{1/2} P_{H_2}{}^{1/2}[*] + K_{GUA}[GUA][*] + \frac{K_3 K_{GUA}[GUA][*] K_{H_2}{}^{1/2} P_{H_2}{}^{1/2}[*]}{[*]}$$

$$C_T = [*]\left\{1 + K_{H_2}{}^{1/2} P_{H_2}{}^{1/2} + K_{GUA}[GUA] + K_3 K_{GUA}[GUA] K_{H_2}{}^{1/2} P_{H_2}{}^{1/2}\right\} \text{(20)}$$

From equation (18):

$$r_4 = k_4[GUAH*][H*] \qquad (21)$$

$$r_4 = \frac{k_4 K_3 [GUA*][H*][H*]}{[*]}$$

$$r_4 = \frac{k_4 K_3 K_{GUA}[GUA][*]\{K_{H_2}{}^{1/2} P_{H_2}{}^{1/2}[*]\}^2}{[*]}$$

$$r_4 = k_4 K_3 K_{GUA}[GUA]\{K_{H_2}{}^{1/2} P_{H_2}{}^{1/2}[*]\}^2$$

$$r_4 = k_4 K_3 K_{GUA}[GUA] K_{H_2} P_{H_2}[*]^2$$

$$r_4 = \frac{k_4 K_3 K_{GUA}[GUA] K_{H_2} P_{H_2}[C_T]^2}{\left\{1 + K_{H_2}{}^{1/2} P_{H_2}{}^{1/2} + K_{GUA}[GUA] + K_3 K_{GUA}[GUA] K_{H_2}{}^{1/2} P_{H_2}{}^{1/2}\right\}^2}$$

BIOGRAPHY OF THE AUTHOR

Pamela Elena Ruiz Martinez was born in Penco, Chile on October 19, 1983. She was raised in Penco, Chile and graduated from Lucila Godoy Alcayaga High School in 2001. She attended the University of Concepcion, Chile and graduated in 2009 with a Bachelor's degree in Chemistry. She is a candidate for the Doctor of Philosophy degree in Chemistry from the University of Maine in August 2018.